ALMA MATER STUDIORUM
UNIVERSITÀ DI BOLOGNA

DOTTORATO DI RICERCA IN

BIOLOGIA CELLULARE E MOLECOLARE

Ciclo 38

Settore Concorsuale: 05/E2 - BIOLOGIA MOLECOLARE

Settore Scientifico Disciplinare: BIO/11 - BIOLOGIA MOLECOLARE

NEUROPHAGE: ORTHOGONAL MOLECULAR ENGINEERING OF THE M13 PHAGE FOR TARGETED DELIVERY TO THE CENTRAL NERVOUS SYSTEM

Presentata da: Lucia Pappagallo

Coordinatore Dottorato

Anna Maria Porcelli

Supervisore

Alberto Danielli

Co-supervisore

Valentina Castagnola

Esame finale anno 2026

Contents

Abstract ___ ***3***

1. Introduction ___ ***5***

1.1 Challenges in overcoming biological barriers ___ 5

1.2 State of the art in Blood Brain Barrier crossing ___ 7

1.3 M13 bacteriophage as a nanocarrier for CNS drug delivery: structure, biology and human body interactions ___ 10

1.4 Phage display: principles, methodology, and applications ___ 14

2. Aim of the thesis ___ ***17***

3. Results and Discussion ___ ***20***

3.1 Mechanistic study of wild-type M13 phage crossing the BBB in *in vitro* models ___ 20

3.2 Phage display of BBB-interacting peptides for enhanced BBB crossing: molecular engineering and *in vitro* 2D model crossing validation ___ 28

3.3 Nanobody-ALFA phage engineering as proof of concept for a specific neuronal targeting platform ___ 33

3.4 Orthogonal engineering of the M13 phage platform for the dual display of BBB-crossing and targeting moieties ___ 37

3.5 Application cases: Parkinson's disease and Glioblastoma ___ 45

4. Conclusions ___ ***56***

5. Material and Methods ___ ***58***

5.1 Cell cultures ___ 58

5.2 Molecular cloning ___ 60

5.3 Phage production ___ 65

5.4 Immunoblotting ___ 67

5.5 Differential ethidium bromide staining ___ 68

5.6 Phage conjugation ___ 69

5.7 BBB crossing essay ___ 70

5.8 3D assembloid penetration ___ 71

5.9 2D Targeting assessment ___ 72

5.10 GL261 hEGFR-vIII^{+} cell line generation ___ 73

5.11 Photodynamic Therapy (PDT) ___ 76

References ___ ***78***

Abstract

The blood-brain barrier (BBB) poses a formidable obstacle to central nervous system (CNS) drug delivery, restricting the passage of over 98% of potential neurotherapeutics. This thesis details the design, engineering, and validation of a versatile nanoplatform based on the M13 bacteriophage, developed to address this challenge and enable cell-specific targeted CNS delivery.

Initially, the wild-type (WT) M13 phage was shown to possess an intrinsic capacity to cross *in vitro* 2D and 3D BBB models via a non-disruptive transcytosis mechanism, achieving successful BBB translocation while maintaining full structural and functional integrity. To enhance this natural ability, phage display was employed to engineer M13 platform variants presenting BBB-interacting peptides on the major coat protein (pVIII), which resulted in significantly increased translocation efficiency compared to the WT virion.

To further validate the platform's potential, an orthogonally engineered phage vector was produced, allowing simultaneous display of a barrier-crossing moiety on pVIII and a specific targeting moiety, an anti-ALFA Tag nanobody, on the minor coat protein pIII. This dual-function orthogonal nanovector demonstrated efficient passage across a 2D BBB model and, critically, retained its specific post-translocation targeting of primary neurons transfected with an ALFA-tag presenting CD4 fusion, thereby validating the platform's ability to overcome sequential biological barriers.

This work highlights how the platform represents a highly promising tool to address one of the major challenges in modern medicine: the efficient delivery of therapeutic and diagnostic molecules into the CNS. Its versatility opens the way to multiple applications, ranging from complex and still poorly understood neurodegenerative disorders, such as Parkinson’s and Alzheimer’s diseases, to highly aggressive CNS malignancies like glioblastoma, where innovative and targeted treatment strategies are urgently needed.

Thus, the therapeutic potential of this technology was explored in a model of glioblastoma. An M13 phage targeting the EGFR-vIII oncomarker and functionalized with the photosensitizer Rose Bengal (RB) was applied for Photodynamic Therapy (PDT). Upon light irradiation, this

system induced potent (~80%) and specific killing of target cancer cells via an apoptotic pathway, highlighting its potential to induce an immunogenic response.

Collectively, these findings establish the M13 bacteriophage as a highly modular, effective, and rationally designable scaffold for developing next-generation, non-invasive, and targeted therapies for diseases of the central nervous system.

1. Introduction

1.1 Challenges in overcoming biological barriers

Biological barriers, whether physical, like skin, or functional, like the blood-brain barrier (BBB), pose significant obstacles to effective drug delivery because they selectively impede the exchange of molecules, complicating the delivery of drugs to specific sites (Cader & Neuhaus, 2022; Mahringer et al., 2021). Successful drug delivery hinges on understanding the barrier's nature (Yang et al., 2017), the drug's properties, such as size, charge, lipophilicity (Correia et al., 2022), and factors such as vascularization and efflux systems (Blanco et al., 2015; Yang et al., 2017). Overcoming these barriers is crucial for effective drug delivery, influencing pharmacokinetics without altering the drug's pharmacodynamic profile (Cuggino et al., 2019). Accordingly, the design of drug delivery systems must account for these impediments, enabling drugs to cross barriers they could not otherwise overcome at safe and effective doses (X. Li et al., 2021; Sweeney et al., 2019). Tailored strategies are needed for each tissue or organ system and, despite advancements, predicting successful outcomes remains difficult due to variations in studied drugs, animal models, and success metrics, highlighting the need for continued research and innovation in drug delivery technologies (Blanco et al., 2015; Helms et al., 2016).

Among biological barriers, the BBB sets itself apart as the most challenging hurdle for drug delivery in the human body, constituting a formidable obstacle to the delivery of therapeutics targeting the central nervous system (CNS) (X. Li et al., 2021; Sweeney et al., 2019). From an anatomical and functional perspective, the BBB is composed of endothelial cells lining the brain capillaries, which are tightly interconnected by specialized structures known as tight junctions (TJs) formed by claudins, occludins, and junctional adhesion molecules (Fig. 1A) (Castagnola et al., 2023; D. Wu et al., 2023). TJs confer high trans-endothelial electrical resistance (TEER) and effectively prevent paracellular passage of hydrophilic solutes and high-molecular-weight compounds (Cader & Neuhaus, 2022). Furthermore, these endothelial cells are characterized by an extremely low rate of pinocytosis and the absence of fenestrations, further reducing nonspecific transcellular permeability (Mahringer et al., 2021). The BBB is not merely a passive physical barrier, it is an integral component of the neurovascular unit (Correia et al., 2022), a complex structure composed of endothelial cells, pericytes, astrocytes,

neurons, and the extracellular matrix (Fig. 1B) (Saint-Pol et al., 2020; Sun et al., 2025). Passage across the BBB is strictly regulated also by active transcellular mechanisms, including carrier-mediated and receptor-mediated transport, adsorptive-mediated transcytosis, and ion channels (Sweeney et al., 2019; Teixeira et al., 2023).

These elements play a pivotal role in regulating barrier permeability and maintaining BBB integrity (Saint-Pol et al., 2020). From a pharmacological point of view, these combined features allow only small, neutral, and lipophilic molecules with a molecular weight below 400-500 Da to cross the barrier by passive diffusion (Sweeney et al., 2019; Yang et al., 2017). Most drugs are therefore prevented from accessing the CNS, except where they can harness specific endogenous transport systems or employ sophisticated, targeted delivery strategies (Cader & Neuhaus, 2022; Mahringer et al., 2021). Even among small molecules, approximately 98% of chemotherapeutic agents fail to reach therapeutic concentrations within the brain parenchyma or infiltrative tumor margins, for example posing a major limitation to the effective treatment of glioblastoma (GB), the most common and aggressive type of primary malignant brain tumor in adults (Sun et al., 2025). Moreover, the integrity and function of the BBB are compromised with aging and in neurodegenerative diseases such as Parkinson's disease (PD), Alzheimer's disease (AD), and amyotrophic lateral sclerosis (ALS). These alterations further exacerbate challenges in brain targeting and therapeutic efficacy (Cader & Neuhaus, 2022).

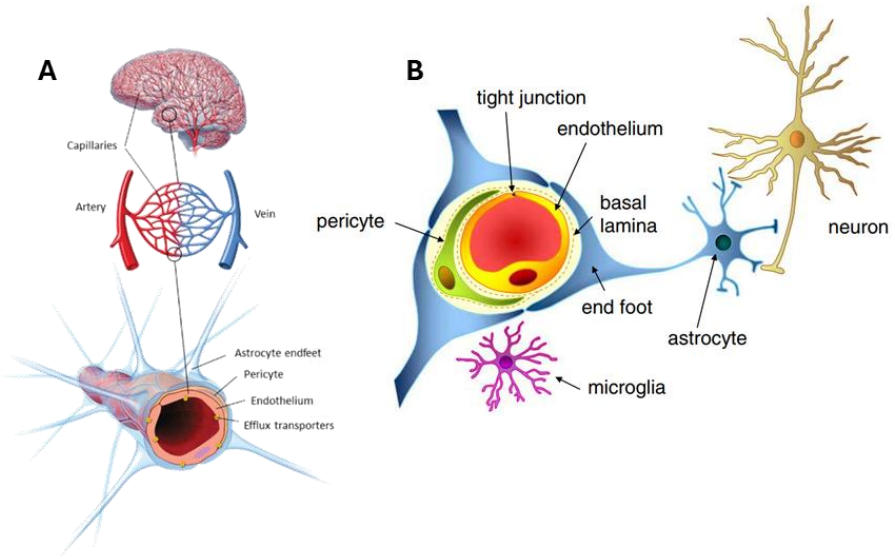

Figure 1: ***(A)*** *Schematic overview of the neurovascular unit at the capillary level: endothelial cells are covered with pericytes, and both cell types are surrounded by astrocytes' endfeet (Helms et al., 2016).* ***(B)*** *Close up of cell types involved in the structure of the neurovascular unit (Abbott, 2013).*

1.2 State of the art in Blood Brain Barrier crossing

The pharmacological bottleneck of CNS drug delivery has become the focus of intense research, especially in the context of unmet clinical needs in treating neurodegenerative disorders, brain tumors, epilepsy, and other CNS pathologies where the BBB further restricts options for effective treatment (Luo et al., 2025; Porro et al., 2025). The earliest strategies to bypass the BBB were fundamentally invasive (Niazi, 2023) including direct intracerebral injections, intrathecal delivery, and more sophisticated methods like convection-enhanced delivery (Cader & Neuhaus, 2022; Correia et al., 2022). While these approaches guarantee effective drug presence in the brain, they are limited by their invasiveness-carrying substantial risks such as infection, neural damage, hemorrhage and have poor distribution profiles, particularly in diffuse or multifocal CNS diseases (Niazi, 2023; Pardridge, 2012).

A more effective and less invasive non-physiologic transient BBB opening may be achieved using osmotic agents, vasoactive drugs, or focused ultrasound, often in combination with microbubbles, facilitating paracellular permeability and temporary access for otherwise excluded drugs (Achar et al., 2021; Qu et al., 2024). However, these methods remain problematic: they are non-selective, can result in unwanted entry of neurotoxic blood components, may damage neural tissue, and suffer from lack of spatial specificity (Correia et al., 2022; D. Wu et al., 2023). Moreover, such disruptions frequently lack the capacity to target only diseased regions, an issue particularly pertinent in heterogeneous conditions like glioblastoma. (Mahringer et al., 2021).

A paradigm shift in recent years has been the development and refinement of colloidal carrier systems, such as lipid and polymeric nanoparticles, dendrimers, and liposomes, for CNS drug delivery (Teixeira et al., 2023). These nanocarriers offer several unique advantages: high loading capacity, surface modifiability, and potential for both passive and active targeting. Surface modification of colloidal carriers has proven particularly significant (Luo et al., 2025; Teixeira et al., 2023). As highlighted by Mahringer et al. (2023), engineering nanoparticles with ligands for receptor-mediated transcytosis (RMT) pathways (e.g., transferrin or insulin receptors), coating with polysorbate 80 or other surfactants, or covalent attachment of peptides and antibodies, can dramatically improve BBB uptake *in vitro* and in animal models. Likewise, strategies exploiting the “Trojan horse” approach (Porro et al., 2025; Yang et al.,

2017), using ligands or antibodies that naturally undergo receptor-mediated endocytosis (RME), show consistent promise in enhancing CNS exposure, even for large or hydrophilic drugs (Mahringer et al., 2021; Teixeira et al., 2023). RMT has emerged as a particularly promising approach (Qiao et al., 2012). It exploits the brain endothelium's natural trafficking systems, whereby therapeutic agents, often linked to ligands such as transferrin, insulin, or low-density lipoprotein analogs, bind to and are internalized by their cognate receptors, actively carrying the therapeutic cargo across the endothelial cells and into the brain parenchyma (Porro et al., 2025; Sweeney et al., 2019). Parallel strategies include transporter-mediated delivery, where modified drugs interact with highly expressed nutrient carriers at the BBB, and adsorptive-mediated transcytosis, which leverages cationic modification of carriers to promote uptake, although with lower specificity (Pardridge, 2012; D. Wu et al., 2023). Despite these advances, translation to the clinic is still incomplete. Many promising colloidal systems remain confined to preclinical development, and those progressing toward clinical application often meet challenges of rapid reticuloendothelial system clearance, immunogenicity, or instability during storage and circulation (Blanco et al., 2015; Luo et al., 2025; Teixeira et al., 2023). Furthermore, the interaction between nanoparticle physicochemical properties and BBB transport remains incompletely understood, with factors such as size, charge, and protein corona formation unpredictably influencing CNS uptake (Blanco et al., 2015; Porro et al., 2025). Building on the principle of endogenous transport, biomimetic nanoparticles, such as those coated with natural membranes (e.g. erythrocyte, leukocyte, or tumor-cell membranes), as well as exosome-based carriers, are increasingly being explored for CNS drug delivery (Achar et al., 2021; Luo et al., 2025). These carriers often display enhanced "stealth" properties and intrinsic CNS activity, but large-scale, reproducible manufacturing and drug loading remain obstacles to widespread use (Correia et al., 2022; Terstappen et al., 2021).

Alternative administration routes can be taken into account (Achar et al., 2021; Cader & Neuhaus, 2022). The intranasal route, which bypasses the BBB via olfactory and trigeminal pathways, has enabled efficient delivery of certain colloidal systems, neuropeptides, and therapeutic proteins to the brain (Gawarkar-Patil et al., 2024; Jiang et al., 2023; Montegiove et al., 2022). However, this strategy is hampered by limited anatomical targeting, mucociliary clearance, and dosing variability (Correia et al., 2022; Koo et al., 2024; Luo et al., 2025). Intra-

arterial and intrathecal infusions represent alternative routes where drugs are delivered directly into the CNS vasculature or cerebrospinal fluid, bypassing the systemic BBB (Niazi, 2023). Intrathecal administration, for example, is widely used for delivering analgesics, antispasmodics, or certain biologics directly to the spinal cord or brain (Sweeney et al., 2019), thereby facilitating high local concentrations and bypassing peripheral metabolism (Madadi & Sohn, 2024).

A further alternative, particularly in neuro-oncology, is offered by implantable devices, wafers, and microchips designed to provide sustained, localized drug release within the brain or tumor resection cavity (Niazi, 2023; D. Wu et al., 2023). The release kinetics and dosing can be fine-tuned, but surgical implantation and potential for local neurotoxicity or infection are significant drawbacks (Sun et al., 2025; Sweeney et al., 2019). Collectively, these alternative routes seek to address the limitations of systemic drug administration for CNS disorders by enhancing brain exposure and minimizing off-target effects (Achar et al., 2021). Each route, however, presents its own technical and clinical obstacles, most notably, invasiveness, lack of precise or region-specific targeting (Sweeney et al., 2019), and challenges regarding chronic administration or patient compliance (Cader & Neuhaus, 2022; D. Wu et al., 2023).

In summary, the state of the art in BBB crossing strategies is defined by innovative advances in nanomedicine (Niazi, 2023; Teixeira et al., 2023) and targeted carrier surface modification (Madadi & Sohn, 2024; Riccardi et al., 2021). Nevertheless, the field continues to confront the limitations of invasiveness, insufficient targeting precision, biological clearance, and uncertain clinical translation (Jiao et al., 2024; Luo et al., 2025; Sun et al., 2025; Teixeira et al., 2023). Addressing these gaps will demand interdisciplinary collaboration, better mechanistic understanding of nanocarrier-BBB interactions, and the implementation of standards for characterization, safety, and efficacy in both preclinical and clinical phases. Only by meeting these challenges can the full therapeutic potential of next-generation CNS drug delivery systems be achieved, enabling precise, effective, and safe transport of therapeutics across the BBB (Senanayake et al., 2025; Sweeney et al., 2019).

1.3 M13 bacteriophage as a nanocarrier for CNS drug delivery: structure, biology and human body interactions

The development of effective strategies for the delivery of therapeutic agents across biological barriers remains a formidable challenge in modern medicine, particularly in the context of CNS disorders (Niazi, 2023). The ever-increasing demand for precise, targeted, and efficient strategies for drug, gene, and imaging agents delivery into the CNS has driven a profound transformation in nanomedicine (Spencer et al., 2020; Sun et al., 2025). Among the most promising biomolecular platforms developed for such purposes, the M13 filamentous bacteriophage has uniquely emerged as a highly versatile nanocarrier due to its structural, genetic, and functional properties, as well as its remarkable capacity for orthogonal bioengineering (Chang et al., 2023; Fadaie et al., 2023; Ulfo, Costantini, et al., 2022; Venkataraman et al., 2025; R. Wang et al., 2023). Recent works have not only unlocked the potential of M13 for cancer theranostics, most notably, for advanced PDT, but have also demonstrated how rational genetic and chemical modifications can expand the boundaries of targeted delivery across intricate biological barriers, including multicellular tumor spheroids (Henry et al., 2015; Turrini et al., 2024; H. Wang et al., 2024; Zadran et al., 2025).

1.3.1 M13 phage biology

Bacteriophages, or phages, are viruses that specifically infect bacteria and are among the most ubiquitous and diverse biological entities on earth, with an estimated 10^{31} particles distributed across all ecosystems (Barr, 2017; Lourenço et al., 2018). Their profound influence on microbial evolution, community dynamics, and even human health has been increasingly recognized in recent decades, not only for their ecological roles but also for their potential applications in biotechnology and medicine (Lourenço et al., 2020). Structurally, phages display remarkable diversity, but many share a common motif: a protein capsid that encloses their genetic material (either DNA or RNA), often equipped with specialized structures for host recognition and infection (Barr, 2017; Lourenço et al., 2018).

Among these, the filamentous M13 bacteriophage, part of the *Inoviridae* family, has become a cornerstone of nanobiotechnology thanks to its distinctive molecular architecture and precise biology (Mai-Prochnow et al., 2015; Sattar et al., 2015; Strathdee et al., 2023). The M13 virion is a long, thin filament, about 6-8 nm in diameter and 900-1000 nm in length,

composed of a circular single-stranded DNA (ssDNA) genome encased in a cylindrical protein shell (G. J. Barbas, 2001). Notably, M13's natural hosts are *E. coli* strains carrying the F-plasmid, with infection initiated by the phage's engagement with the F-pilus: this pilus retracts and facilitates the viral genome's entry into the host cell, illustrating the sharp specificity of phage-host interactions (Fadaie et al., 2023; Lourenço et al., 2018). The M13 genome, relatively compact at 6.5 kilobases, encodes only eleven proteins (Mai-Prochnow et al., 2015). These genes are functionally classified according to their roles in capsid protein synthesis, genome replication, and coordination of phage assembly at the bacterial membrane (Fig. 2A) (G. J. Barbas, 2001; Rakonjac et al., 2024). An especially interesting aspect is the intergenic region, devoid of coding sequences but containing key replication origins, as well as a specialized "packaging signal" critical for initiating phage assembly (Rakonjac & Model, 1998). Upon entry into the bacterial cytoplasm, the phage's (+) strand is replicated using the host's machinery, while the complementary (−) strand predominantly serves as a transcription template for phage proteins (Fadaie et al., 2023; G.P. Smith, V. Petrenko, 1997). Genes II, V, and X encode cytoplasmic proteins that are pivotal to DNA replication, and after infection, the viral ssDNA is first converted into a double-stranded replicative form (RF-DNA) before the assembly of new ssDNA genomes (Mai-Prochnow et al., 2015). Structural proteins, encoded by genes III, VI, VII, VIII, and IX, are synthesized and trafficked to the bacterial inner membrane, where new phage particles are assembled (Fig. 2B) (Sioud, 2019).

The major coat protein, pVIII, is present in roughly 2700 copies per filament and forms the principal scaffold for both virion stability and nanotechnological modification. This abundance makes pVIII an ideal substrate for dense chemical conjugation with drugs, imaging agents, or photosensitizers (Bortot et al., 2022; Hess et al., 2012; Ulfo, Cantelli, et al., 2022).

Minor coat proteins (pIII, pVI, pVII, and pIX), found in five copies at each end of the filament, cap the viral particle and play essential roles in infection and assembly (Rakonjac & Model, 1998). Of particular note, pIII is widely exploited in phage display technologies due to its exceptional tolerance for genetic fusion with diverse peptides and protein domains (Henry et al., 2015; Petrosino et al., 2023; Sioud, 2019, 2019; Strathdee et al., 2023; Turrini et al., 2024). This modular configuration, abundant, modifiable pVIII subunits along the capsid and functionalizable pIII at the end, enables "orthogonal engineering," allowing for independent,

programmable control over both targeting and cargo loading functionalities (Hess et al., 2012; K. H. Lee et al., 2013; Ulfo, Costantini, et al., 2022; H. Wang et al., 2024).

Genes I, IV, and XI are also central: although not capsid constituents, they code for proteins that orchestrate the assembly and extrusion of new phage particles. The pI protein is thought to associate with the inner membrane and potentially forms channels for genome export. Its companion, pXI, shares homology with pI's C-terminal and assists in assembly, while pIV integrates into the outer membrane, likely facilitating the exit of mature virions from the bacterial host (G. J. Barbas, 2001; Loh et al., 2021; Rakonjac et al., 2024).

In summary, the elegance of M13's molecular organization, small genome, modular coat, and specialist infection machinery, not only underscored its ecological success but also paved the way for its adoption as a biological nanomaterial (Chang et al., 2023; Mai-Prochnow et al., 2015; Petrosino et al., 2023; Sattar et al., 2015). Its physical structure and genetic simplicity permit deep genetic and chemical manipulation, creating the foundation for wide-ranging applications in drug delivery, targeted imaging, diagnostics, and bio-nanotechnology (Barr, 2017; Bichet, Chin, et al., 2021; Bichet, Patwa, et al., 2021; K. H. Lee et al., 2013; Rakonjac et al., 2024; Strathdee et al., 2023; Turrini et al., 2024; Ulfo, Costantini, et al., 2022)

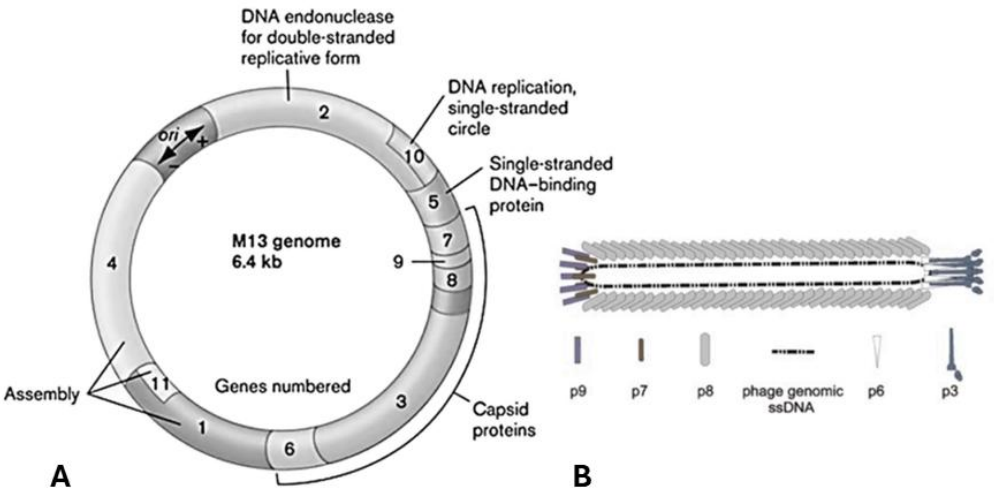

Figure 2: ***(A)*** *M13 phage genome: genes can be classified based on their function. Genes I, V and X are involved in replication; genes I, IV, and XI encode for assembly protein; genes III, VI, VII, VIII, and IX are coding sequences of capsid proteins.* ***(B)*** *M13 coat proteins. The pIII is expressed in five copies on the tip of the phage, while the pVIII covers the whole length of the phage with its 2700 copies (Chaitanya, 2019).*

1.3.2 M13 interaction with human body

The intricate relationship between bacteriophages and biological barriers within the human body is reshaping our understanding of phage biology and their biomedical promise (Barr, 2017; Bichet, Chin, et al., 2021; Nguyen et al., 2017). The concept of phage adherence to mucus highlights how weak interactions between capsid-displayed domains and mucosal glycans facilitate the enrichment and persistence of phages within mucus layers, where they can provide a non-host-derived layer of immunity and limit pathogenic bacterial colonization (Bichet, Chin, et al., 2021; De Sordi et al., 2019a; Kan & Barr, 2023; Lourenço et al., 2020). These mucus-adherent phages show subdiffusive movement, increasing encounters with bacterial hosts and reinforcing protective mucosal immunity, a process supported by experimental data and now leveraged for phage therapy and microbiome modulation (Barr, 2017; Lourenço et al., 2020; Nguyen et al., 2017). Extending beyond mucosal barriers, the idea of an "intra-body phageome" has emerged to describe the population of phages found in sterile regions such as blood, organs, lymph, and the CNS. This phenomenon is attributed to the ability of phages to traverse cellular barriers by mechanisms such as transcytosis, receptor-mediated transport, or passage through compromised epithelia, which may contribute to systemic immune protection, tolerance, and dynamic microbiota-host interplay (Barr, 2017; Bichet, Chin, et al., 2021; Nguyen et al., 2017). Research has established that phages can actively cross polarized epithelial and endothelial layers in several organs, including the gut, lung, liver, kidney, and brain, via apical-to-basolateral trafficking that involves the Golgi apparatus, occurring at physiologically substantial rates (Bichet, Chin, et al., 2021; Kan & Barr, 2023; Nguyen et al., 2017). Notably, studies dating back to the 1940s demonstrated that phages administered systemically can be recovered from brain tissue, providing early evidence of phage transit across the BBB (Bichet, Chin, et al., 2021; Nguyen et al., 2017).

Beyond transcytosis, phage interactions with mammalian cells involve adhesion, internalization, and trafficking that are influenced by cell type, phage morphology, and environmental context, with implications for pharmacokinetics and therapeutic design (Kan & Barr, 2023; Nguyen et al., 2017). Importantly, the defensive and immunomodulatory effects of phages, both at mucosal surfaces and systemically, underscore their role in shaping host microbiomes, balancing bacterial populations, and supporting innate and adaptive immunity (Barr, 2017; Bichet, Chin, et al., 2021; De Sordi et al., 2019a, 2019b). The development and

dissemination of experimental protocols and quantitative imaging tools has further advanced the study of phage-eukaryote interactions, suggesting a profound biomedical potential for engineered phage vectors in drug delivery, neuroimaging, immune modulation, and the treatment of diseases affecting previously inaccessible compartments (Bichet, Patwa, et al., 2021; Kan & Barr, 2023; Nguyen et al., 2017; Strathdee et al., 2023).

1.4 Phage display: principles, methodology, and applications

M13's biotechnological potential is exemplified by the phage display technique, first described by George Smith and Valery Petrenko in 1985 (G.P. Smith, V. Petrenko, 1997). Phage display is an ingenious technique that takes advantage of the biology of bacteriophages to create a direct physical link between a displayed protein or peptide and its encoding DNA (Bratkovič, 2010; Henry et al., 2015; Sioud, 2019). Since its development, phage display has revolutionized both basic research and applied biotechnology, offering a powerful way to select molecules with specific functions or binding properties from vast combinatorial libraries (Harada, 2018; H. Wang et al., 2024).

At the heart of phage display lies the process of genetic fusion. Here, a DNA sequence encoding a peptide or protein fragment is inserted into the gene for a phage coat protein, such as pIII or pVIII in filamentous phages like M13 (G.P. Smith, V. Petrenko, 1997; Sattar et al., 2015). When these recombinant phage infect bacterial cells, they produce new viral particles that feature the foreign peptide fused to one of their surface proteins (Bratkovič, 2010). What makes this method truly powerful is that each individual phage displays a unique peptide on its surface, while carrying within it the gene that encodes that same sequence (Rakonjac et al., 2024). Phage display is versatile not only in what can be displayed but also in how it is displayed (G. J. Barbas, 2001). For instance, pIII, a minor coat protein present in five copies per phage, is particularly well-suited for the display of large peptides or protein fragments such as single chain antibodies or nanobodies because it tolerates larger genetic fusions (Turrini et al., 2024; Venkataraman et al., 2025). By contrast, pVIII is present in thousands of copies per phage and is typically used for presenting small peptides densely across the phage surface (Hess et al., 2012). Building on this foundation, modern phage display strategies employ vectors and display modes tailored to the properties and function of the peptide or protein of interest (Bratkovič, 2010; Rakonjac et al., 2024). If the polypeptide's coding sequence is directly fused

in-frame within the phage genome, the method is called “type 3” (pIII) or “type 8” (pVIII) display, resulting in fully recombinant virions. Fusions of large polypeptides can impede pVIII’s structural function, but pIII remains robust even with sizable inserts (G. J. Barbas, 2001). In alternative, widely used hybrid methods involve the presence of both wild-type and recombinant copies of the display protein, either together on the genome (type 88/33) or distributed between genome and external vector (type 8+8/3+3), allowing control of display density and polypeptide size limits (G.P. Smith, V. Petrenko, 1997; Henry et al., 2015). This modularity allows precise and versatile engineering of the phage surface, enabling the development of multifunctional particles that can act simultaneously as targeted drug carriers, imaging agents, and biosensors (Bortot et al., 2022; Henry et al., 2015; K. H. Lee et al., 2013; Rakonjac et al., 2024; Ulfo, Cantelli, et al., 2022). By independently tuning the displayed targeting moieties and functional payloads, phage display platforms like M13 can be adapted to a wide range of biomedical and materials science applications (Bortot et al., 2022; Ghosh, Kohli, et al., 2012; Hess et al., 2012; Loh et al., 2021; Petrosino et al., 2023; Sattar et al., 2015; Turrini et al., 2024; Zadran et al., 2025).

Over recent decades, these innovations have dramatically expanded M13’s impact in nanotechnology, particularly within biomedicine and material science (Bratkovič, 2010; Henry et al., 2015; Rakonjac et al., 2024). Genetic engineering permits the targeted display of a vast array of peptides, antibodies, or small molecule ligands, and orthogonal chemical modifications allow the dense loading of drugs, imaging agents, or photosensitizers, sometimes hundreds per phage particle (Ghosh, Kohli, et al., 2012; Rakonjac & Model, 1998; Sattar et al., 2015; Ulfo, Cantelli, et al., 2022). This orthogonal approach, by which the targeting moiety and cargo loading are independently tuned, equips M13 nanobioparticles to selectively target and deliver therapeutics deep within solid tumors, penetrate complex tissue architectures, or access anatomical compartments that are otherwise difficult to reach (Fadaie et al., 2023; Ghosh, Kohli, et al., 2012, 2012; Sioud, 2019; H. Wang et al., 2024). Beyond biological interfaces, the versatility of phage display has enabled M13 to function as a “biological building block” for inorganic nanomaterials and hybrid bio-inorganic devices. The Belcher group and collaborators have shown that M13 can direct the mineralization process and assemble nanowires or semiconducting materials with nanometer-scale precision by genetically engineering the phage to display inorganic-binding peptides, leading to the

programmable organization of materials for energy, electronics, or medical applications (Ghosh, Kohli, et al., 2012; Ghosh, Lee, et al., 2012; S.-W. Lee et al., 2002). Meanwhile, researchers such as Rakonjak have pioneered the development of shortened, non-replicative filamentous phage (Ff) nanorods, called Ff-nano, constructed by truncating the native viral particle. These nanorods are particularly well suited for sensitive diagnostics, rapid lateral flow assays, and the fabrication of tissue engineering scaffolds, owing to their stability, non-replicative nature, and amenability to functionalization (Sattar et al., 2015). The modular and flexible engineering that defines phage display means that the same platform can be readily adapted for multiplexed detection of pathogens, controlled spatial delivery of therapeutic agents, or the assembly of novel smart materials for custom applications (Harada, 2018; Henry et al., 2015). Collectively, these advancements emphasize how the M13 bacteriophage, empowered by phage display and orthogonal chemical modification, serves as a rationally designed nanoplatform, by positioning not only as a foundational technology for molecular discovery, but as a cornerstone for the design of the next generation of nanoscale therapeutics, diagnostics, and synthetic materials (Fadaie et al., 2023; Ghosh, Kohli, et al., 2012; Loh et al., 2021; Sioud, 2019; Ulfo, Cantelli, et al., 2022; H. Wang et al., 2024).

2. Aim of the thesis

Delivering therapeutic agents to the central nervous system (CNS) is extremely challenging because of the blood-brain barrier (BBB), a highly selective and protective interface that strongly restricts the access of both small and large molecules to brain tissue. This barrier creates major hurdles for treating neurological disorders and CNS tumors, such as Parkinson's disease (PD) and glioblastoma (GB). Traditional invasive and systemic delivery techniques are often limited by low efficiency and significant side effects, highlighting the urgent need for more targeted, effective, and less invasive strategies. In this context, recent advances in nanotechnology and biomimetic carriers, including viral nanoparticles, are showing great promise for overcoming these biological barriers and enabling more precise delivery of drugs to the brain. Among the most promising approaches stand out phage-based nanovectors, which combine remarkable versatility and targeting potential with a large cargo capacity. Their molecular structure allows for precise genetic engineering towards specific targets, and they can be further orthogonally functionalized through selective chemical conjugation. This unique set of features makes them particularly suitable for addressing the complex challenges of CNS drug delivery, offering an advanced and customizable platform for transporting therapeutic molecules across the BBB .

The aim of this thesis is to generate and validate an M13 bacteriophage-based nanoplatform designed for the targeted delivery of molecules of therapeutic interest into the CNS. Building on insights from advanced nanotechnology and molecular engineering, this work focuses on addressing the challenge of crossing the BBB while achieving specific neuronal targeting.

Initially, the wild-type (WT) M13 phage was evaluated for its ability to translocate across *in vitro* BBB models of increasing complexity, specifically employing both 2D endothelial monolayer and 3D complex assembloid models. The quantitative assessment of phage translocation provided a baseline for further engineering efforts.

The WT phage was, then, further modified on the pVIII major coat protein to express peptides, such as transferrin-mimic (Tfm), GYR and C7-BBB peptides, known from literature to facilitate BBB penetration, interacting with key endothelial transport receptors, thus improving transcytosis and transmigration efficiency.

To proof targeting specificity, the WT M13 phage was genetically engineered to display, on the pIII minor coat protein, an anti-Alfa Tag nanobody, directed against a synthetic mOrange-hCD4-AlfaTag membrane protein expressed on the surface of target neuronal populations. This modification aimed to proof the selective delivery of cargos to defined neuron types.

A key innovation of this work is the assembly of an orthogonally engineered M13 phage platform, integrating both targeting and BBB-crossing functional modules within a single scaffold. The orthogonally-modified phage was tested for its ability to efficiently cross the 2D BBB model, target neurons of interest, and, crucially, retain its targeting phenotype following BBB crossing. This represents a significant advancement, as it enables molecular cargoes to reach and act upon specific neuronal populations only after overcoming the barrier that protects the brain.

In line with translational goals, the thesis further explores the potential application of this nanoplatform in models of Parkinson's disease (PD) and glioblastoma (GB). For the PD, the purpose of the platform was the transport of photovoltaic nanoparticles across the BBB to the CNS, with the intent of restoring neuronal electrical activity. In the context of GB, the goal of the platform is to facilitate the delivery of photosensitizer molecules deep within tumor tissues, enabling their eradication through photodynamic therapy. These case studies underscore the versatility and therapeutic potential of the M13 nanoplatform for both neurodegenerative and anti-cancer applications.

Overall, this research paves the way for the development of advanced, minimally invasive, and cell-specific delivery technologies for CNS diseases, laying the groundwork for novel treatment modalities that could overcome the limitations of current strategies.

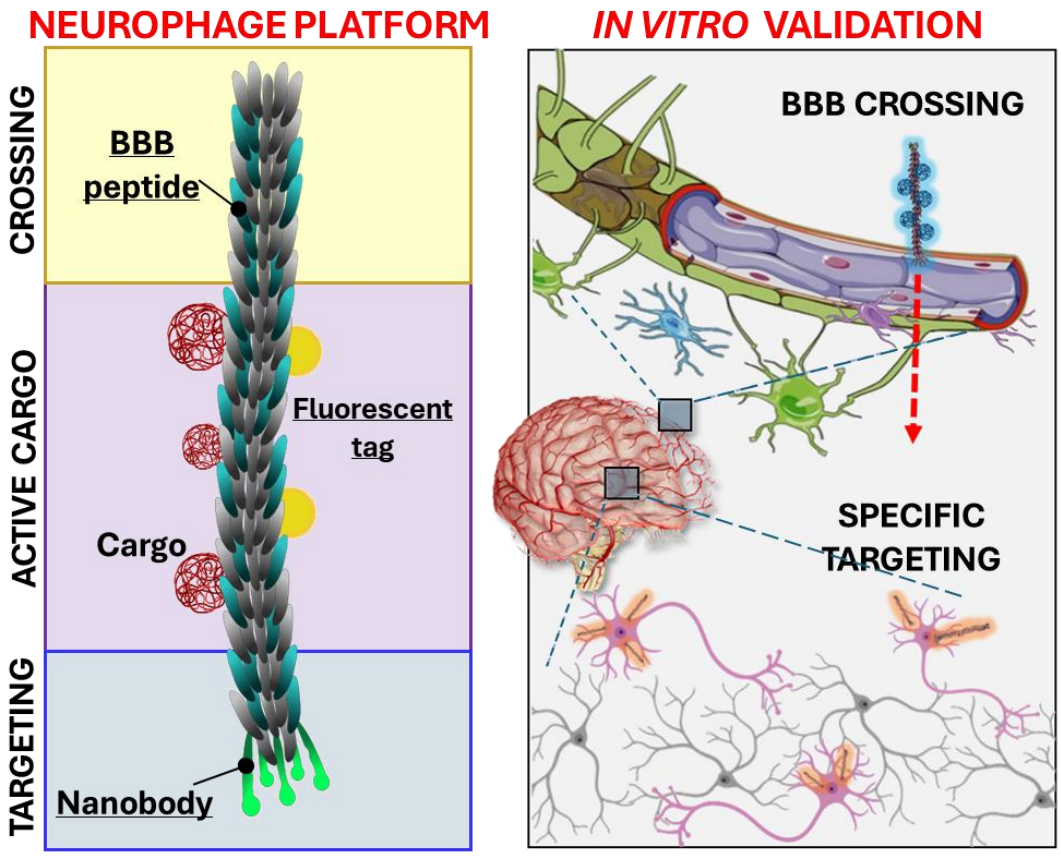

Figure 3: ***Graphical Abstract of the Neurophage platform****. It is an orthogonal, genetically engineered M13 phage-based nanoplatform designed to enter the CNS and enable targeted delivery of molecules of interest to specific cell populations. In this study, the platform displays a BBB-interacting peptide that enhances BBB translocation on the pVIII major capsid protein, that would allow non-invasive CNS access following systemic administration. As a proof of concept, the Neurophage platform was evaluated for its ability to cross in vitro 2D and 3D BBB models and to deliver a fluorescent payload to a specific population of transfected primary mouse cortical neurons.*

3. Results and Discussion

3.1 Mechanistic study of wild-type M13 phage crossing the BBB in *in vitro* models

The M13 phage exhibits a natural propensity to penetrate the BBB, a property first reported in 1943, when phages were isolated from murine brain following systemic administration (Dubos et al., 1943). Later studies demonstrated brain entry after intranasal delivery in mice, a capability attributed to its filamentous morphology and unique surface chemistry (Huh et al., 2019). *In vitro* studies though, lack of a mechanistic evidence on how the M13 phage crosses the BBB. In this study we demonstrated that M13 phages exploit receptor-mediated transcytosis to cross the endothelial barrier without disrupting tight junction, both in 2D endothelial monolayer models and 3D multicellular BBB assembloids.

We started by producing the M13 phage following the protocol outlined in the "material and methods" section optimized by our laboratory to ensure high yield and reproducibility. The quality and consistency of the produced phages were rigorously assessed using multiple analytical approaches. Absorbance spectra were employed to estimate virion concentration and purity, while Transmission Electron Microscopy (TEM) confirmed the characteristic filamentous morphology of the particles (data not shown). In addition, Western Blot (WB) analyses verified the presence of major coat proteins, such as pVIII and pIII, and excluded potential contaminants (Fig. 4 A - B).

For downstream applications, the phages were chemically conjugated with Alexa Fluor 488 or 594 fluorophores via an N-hydroxysuccinimide (NHS)-ester reaction, a well-established method for labelling proteins. Zeba desalting columns were used to remove unreacted fluorophores and to facilitate purification under compatible buffer conditions. The integrity and purity of the labelled virions were then evaluated by agarose gel electrophoresis and UV spectroscopy, confirming the absence of free dye and detecting stable, intact virions (Fig. 4 C-D). Through systematic optimization of both production and conjugation steps, we achieved high inter-batch reproducibility and consistent experimental outcomes across independent preparations. This robust phage production and labelling pipeline was a fundamental prerequisite for evaluating the intrinsic BBB penetrating capacity of M13 phages, ensuring that

observed differences in translocation efficiency reflected biological properties rather than technical variability.

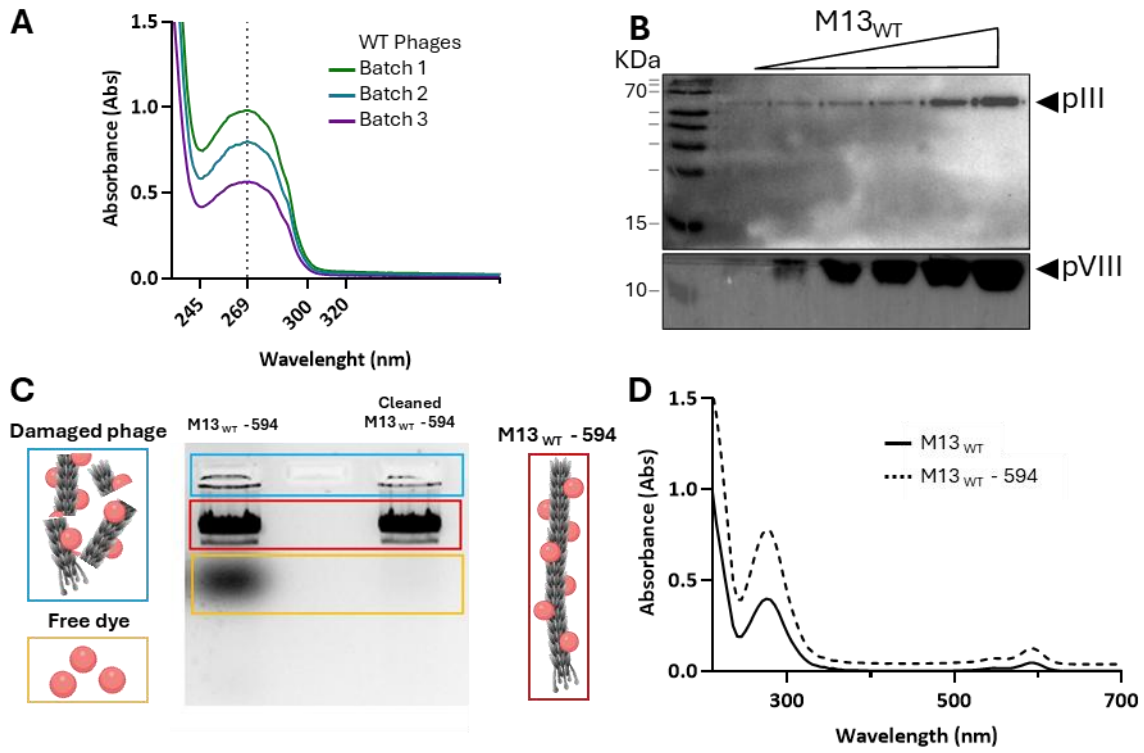

Figure 4: **(A)** UV-VIS spectra of three $M13_{WT}$ batches. **(B)** WB analysis of different $M13_{WT}$ dilutions, showing the presence of the pIII and pVIII coat proteins. **(C)** Assessment of $M13_{WT}$ purity and integrity by agarose electrophoresis showed three populations: aggregated phages trapped in the well (blue), intact fluorescently labelled phages (red), and free dye (yellow). **(D)** UV spectra of $M13_{WT}$ before and after conjugation with CF594.

Once the phage production pipeline was validated, we proceeded to the establishment and characterization of the 2D *in vitro* BBB model, a well-established platform for investigating molecular translocation across the endothelial barrier (Badawi et al., 2024; Helms et al., 2016). The BBB constitutes the principal and highly selective interface between the CNS and the systemic circulation, where brain microvascular endothelial cells, supported by astrocytes, pericytes, and the basement membrane, regulate vascular permeability and restrict paracellular flux through complex networks of TJs composed of claudins, occludins, and zonula occludens proteins (Fig. 5 A). In this 2D model, bEnd.3 cells are cultured on collagen-coated polyethylene terephthalate (PET) semipermeable transwell membranes. This setup yields a polarized confluent monolayer separating the apical chamber (“blood-side”) from the basolateral chamber (“brain-side”), thereby recapitulating essential aspects of microvascular organization in vivo (Fig. 5 B). This simple yet robust model offers direct quantification of

translocated particles while preserving barrier properties relevant to CNS entry studies. Tight junctions formed between adjacent cells restrict the paracellular flow of ions, thereby increasing the electrical resistance, which can be modeled by an equivalent circuit, omitting the contribution of the membrane resistance. The barrier integrity was quantitatively assessed via TEER measurements using a CellZscope system and TEER values > 10 Ω×cm² were taken as indicative of functionally tight monolayers, with our cultures typically ranging from 15–20 Ω×cm². Importantly, TEER was monitored both prior to and throughout M13 phage exposure, remaining consistently above threshold values, thus confirming endothelial viability and absence of phage-induced barrier disruption (Fig. 5 C – D). Furthermore, two control conditions ensured accurate normalization of crossing data (Fig. 5 E):

(i) Untreated transwells (UT) with fully formed tight junctions, representing the baseline for intact barrier function.

(ii) Low-density (LD) cultures, in which insufficient cell confluence precluded tight junction formation, allowing unrestricted paracellular diffusion.

Comparison with LD controls enabled estimation of the proportion of phage particles interacting with or retained by the monolayer, thereby yielding a normalized BBB translocation percentage that corrects for experimental and structural limitations of the *in vitro* model.

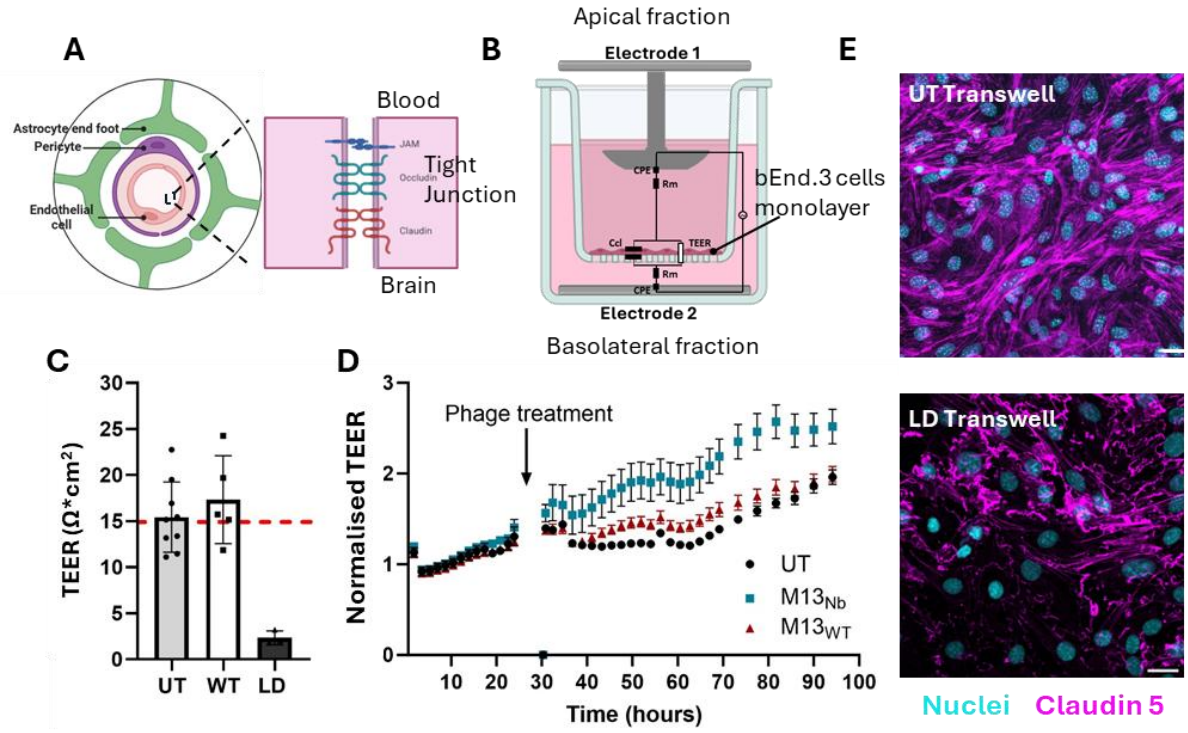

Figure 5: ***(A)*** *Schematic representation of the neurovascular unit and the tight junctions sealing the space between adjacent endothelial cells.* ***(B)*** *An equivalent electrical circuit models endothelial cell monolayers, where AC voltage applied across electrodes measures resistance reflecting the parallel paracellular pathways.* ***(C)*** *Average TEER values reached before the phage treatment in BBB crossing experiments.* ***(D)*** *Representative overtime TEER values (normalized over the value at T=0) monitored throughout the BBB crossing experiment show that the barrier was stable and was not altered after phage treatment, confirming the M13 biocompatibility.* ***(E)*** *bEnd.3 cells seeded onto transwell inserts at high (UT) and low (LD) density for 72 hours show a different tight junction spatial organisation, visualised through immunostaining with anti-claudin5 antibody (magenta). LD transwells do not possess a formed barrier (cyan: nuclei; scale bar: 20 µm).*

Following validation of the model, we investigated the translocation dynamics of the $M13_{WT}$ phages across the endothelial barrier. Phage suspensions (5×10^{11} virions/mL in complete DMEM) were applied to the apical compartment of confluent, TEER-validated transwells. Fluorescently labelled phages, prepared as described above, enabled precise quantification of crossing events via fluorescence measurements of the basolateral compartment at defined time points through flow cytometry as described in 5.7 section (Fig. 6 A). To addresses the possible influence of the specific fluorophore on the phage biological interactions, two different fluorophores were conjugated to the phage (Alexa Fluor 488 or 594). Given that the measured crossing ability does not significantly diverge when different fluorophores are used (Fig. 6 B). Considering that the covalently bound fluorophore units are in the range of 84-154 over about 2700 pVIII proteins of the main coat (therefore 5%), the differences (e.g., changes to the phage surface charge) contributed to our systems appear to be marginal. To delineate

the transcellular component from passive leakage, results were normalized to LD controls lacking tight junctions, which represent 100% paracellular passage.

The $M13_{WT}$ phage exhibited robust BBB penetration, which reached around 40% crossing after 72 h of phage exposure, consistent with receptor-mediated uptake mechanisms. Barrier function remained uncompromised throughout the assays, as evidenced by stable TEER values above 10 Ω×cm² during and after phage exposure, further corroborated by immunofluorescence imaging, which revealed intact distribution of TJ proteins such as claudin-5 (Fig. 6 C).

TEM analysis of basolateral fractions confirmed that translocated phages retained structural integrity (data not shown), highlighting the suitability of M13-based vectors for CNS-targeted delivery *in vitro*. In addition, WB analysis allowed us to verify the presence and structural integrity of the major coat protein pVIII in the basolateral fractions, further confirming that the intact phage, rather than free fluorophore, successfully crossed the barrier (Fig. 6 D).

Furthermore, to assess the full biological functionality of the translocated virions, a soft agar plaque assay was conducted on *E. coli* TG1 host cells. Serial dilutions of the basolateral phage solutions were plated, and the appearance of discrete lysis plaques confirmed the infective capability of the recovered phages, thereby validating that $M13_{WT}$ particles were functionally intact after crossing the *in vitro* BBB model (Fig. 6 E)

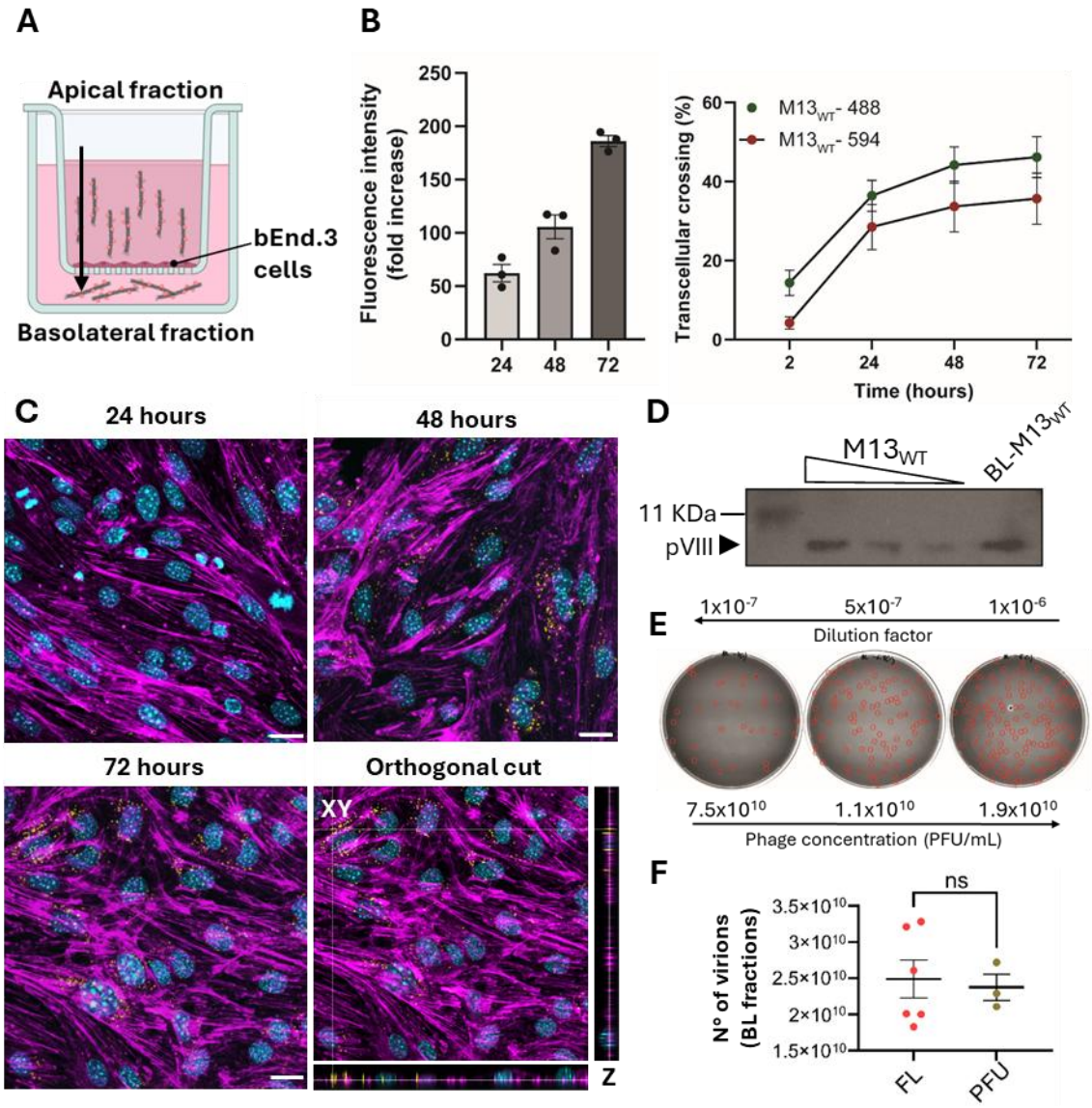

Figure 6: ***(A)*** *Schematic representation of the 2D BBB crossing experiment: bEnd.3 cells seeded on a transwell membrane were incubated with a phage solution in the apical compartment, and at 2, 24, 48, and 72 hours, aliquots were taken from the basolateral compartment to quantify the phages that had crossed the model by measuring their fluorescence.* ***(B)*** *Kinetics of internalisation of M13WT-594 in bEnd.3 cells (n=3, mean ± SEM).* ***(C)*** *Representative confocal images showing M13WT-594 internalization in bEnd.3 cells at the different time points; Orthogonal section (z = 22) of the three fluorescence channels acquired at 72 h, highlighting phage internalization within the cells. (cyan: nucleus; magenta: claudin; yellow: M13WT-594; scale bar: 20 µm).* ***(D)*** *Structural integrity verification of phages into BL fractions: Western Blot analysis of the phage-containing BL compartment compared to different dilutions of the M13WT stock, showing bands related to the major pVIII coat protein (about 8 KDa).* ***(E)*** *Functional integrity assessment of phages recovered from BL compartment: representative plaque assay dishes showing three serial dilutions of M13WT collected in the BL compartment after 72 hours of incubation.* ***(F)*** *Comparison of phage quantification in BL fractions by fluorometric analysis and plaque assay (PFU).*

Beyond 2D endothelial monolayers, M13 phages have also shown a remarkable propensity to traverse complex multicellular barriers in other contexts. For instance, in our previous work (Turrini et al., 2024), we reported that genetically modified phages directed toward colon cancer cells penetrated deeply into densely packed colorectal cancer spheroids. We also

demonstrated that GD2-targeted modified phage vectors selectively infiltrating GD2-positive neuroblastoma spheroids (Zadran et al., 2025), corroborating the inherent capability of M13 to penetrate and traverse compact, high-resistance cellular architectures while preserving functional cargo delivery.

To evaluate whether this behaviour extends to more complex BBB models, we employed a 3D multicellular assembloid system fully described and validated from the literature (Bergmann et al., 2018; Castagnola et al., 2023). This model incorporates human brain microvascular endothelial cells forming a tight ZO-a-positive peripheral layer around a core of pre-labelled human astrocytes and pericytes, recapitulating the supracellular physiological architecture of the BBB (Fig. 7 A).

In this experiment, assembloids were incubated with $M13_{WT}$-CF594 phages for 72 h, cryosectioned, and imaged via confocal microscopy. In this configuration, the labelled phage needs to be internalised by the peripheral endothelial layer, given that the paracellular space is sealed by tight junctions and then pass between the different cell cytotypes by transcytosis and intercellular exchange, to reach the assembloid core. Astrocytes and pericytes have been preventively stained to distinguish the assembloid core from the brain endothelial layer and quantify the localisation of $M13_{WT}$-594.

Experimental data in Figure 7 B show that phages actually translocated inside the core, indicating an excellent propensity of penetration and intercellular exchange of material. Indeed, quantitative analysis performed by our collaborators at IIT revealed an even distribution of phages between the endothelial external monolayer (~51%) and astrocyte/pericyte core (~49%), confirming efficient penetration past the endothelial layer into deeper parenchymal-mimicking regions.

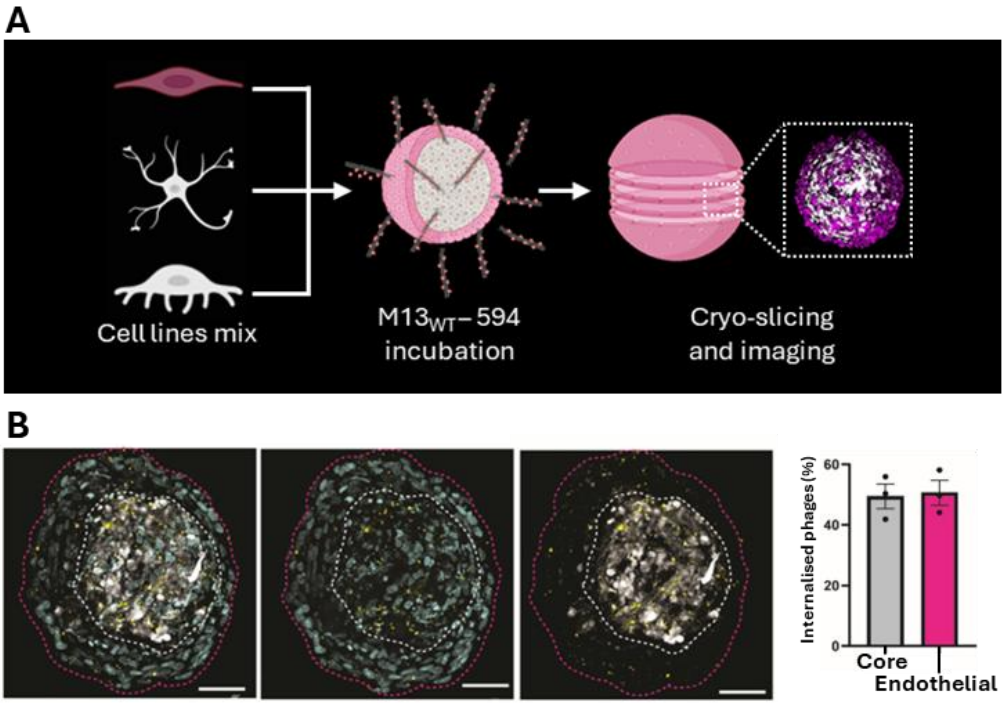

Figure 7: $M13_{WT}$ interactions with a 3D BBB multicellular model. ***(A)*** *Schematics illustrating the experimental approach: 3D multicellular assembloids were prepared by employing pre-labeled human astrocytes and human pericytes together with non-labeled human brain endothelial cells. Assembloids were treated with $M13_{WT}$-594 for 72 hours, fixed, cryo-sliced and observed under a confocal microscope.* ***(B)*** *Representative confocal images of assembloid slices and related quantification of $M13_{WT}$-594 (indicated in yellow) distribution in the endothelial layer or in the astrocytes/pericytes core; nuclei are in cyan, pre-labelled (cell tracker) astrocytes and pericytes are in white; scale bar: 50 µm.*

Together, the results obtained from both the 2D and 3D BBB models provide compelling and complementary evidence that $M13_{WT}$ phages are capable of crossing the BBB model through an active, non-disruptive transcytosis mechanism, while fully preserving their structural integrity and biological functionality. This cross-model consistency, where a phenomenon first quantified in a minimalistic barrier recurs robustly in a complex, physiologically relevant environment, strongly suggest that the M13 phage can be tweaked into a highly adaptable and reliable nanovector for CNS-targeted delivery. Such versatility offers significant translational potential for shuttling therapeutic or diagnostic molecules across the BBB into the CNS. While these evidences represent only a starting point, they highlight the potential of phage-based nanocarriers to access the CNS. Thanks to the ease of applying the phage display technique to the M13 scaffold, these nanocarriers can be further enhanced, making them even more promising for overcoming current technological limitations in the treatment of CNS disorders."

3.2 Phage display of BBB-interacting peptides for enhanced BBB crossing: molecular engineering and *in vitro* 2D model crossing validation

Despite the excellent ability of $M13_{WT}$ to penetrate the BBB *in vitro*, it is necessary to further enhance its tropism towards the CNS to achieve greater therapeutic potential. To accomplish this, we designed a strategy to exploit known BBB-interacting peptides for the display on the phage capsid. Many displays strategies exist but we focused on the 8+8 phage display system. It is a hybrid approach in which recombinant and WT copies of the pVIII major coat protein are co-expressed, enabling a variable number of copies of a selected peptide to be displayed along the filamentous virion of the M13 phage. It preserves the proper capsid assembly and integrity and amplifies ligand-receptor interactions through multivalency.

In the context of BBB interaction and crossing, several peptides, such as transferrin-mimic (Tfm), GYR, and C7, have been identified in literature via *in vivo* phage display biopanning. They show to interact specifically with endothelial receptors, promoting RMT and efficient BBB penetration *in vitro* and *in vivo* (J. Li et al., 2012; L.-P. Wu et al., 2019; Xie et al., 2019). By integrating the nanofiber-like morphology, biocompatibility, and genetic tunability of M13 with multivalent display of BBB peptides, this approach is intended to maximize endothelial engagement, facilitate transcytotic uptake, and improve phage-mediated delivery of molecular payloads into the CNS.

To generate M13 phages displaying BBB-interacting peptides, we started from the molecular cloning using a custom phagemid vector (pK8001), which encompassess unique restriction sites for cloning. Synthetic oligonucleotides encoding the Tfm, GYR, and C7 peptides were annealed and ligated into the digested pK8001 backbone to create the final pK8001_BBB-interacting peptide phagemids (Fig. 8 A). Following sequence validation, we compared two methods for phage production: superinfection (SI) and co-transformation (CoT Fig. 8 B). The superinfection protocol involved transforming *E. coli* TG1 cells with the phagemid and subsequently infecting them with a WT M13K07 helper phage. This approach produces a mixed population of long (~1 µm) and short (~500 nm) phages, depending on whether the WT genome or the phagemid is packaged inside the capsid, but both types phenotypically express a mix of WT pVIII and peptide displaying-pVIII.

Alternatively, the co-transformation method involved simultaneously transforming *E. coli* DH5α cells with the pK8001 phagemid and the M13ΔOri Hyperphagemid that provides all the phage proteins but cannot be packaged into the newly formed virions. This strategy produces a homogeneous population of short phages (~500 nm) that genetically encapsulate only the pK8001 phagemid while maintaining the mixed pVIII phenotype. As shown in Figure 8 C, structural characterization via western blot revealed that the co-transformation method was completely ineffective for GYR and C7, whereas for Tfm phage the production of pIII and pVIII did occur, although at very low levels. This finding is rooted in the complex and stoichiometrically sensitive nature of M13 phage assembly, in fact M13 assembly is a highly regulated process, not a simple aggregation of proteins. It occurs at the bacterial membrane, where a dedicated machinery encoded by genes I, IV, and XI forms a channel to orchestrate the extrusion of new phage particles. The phage genome is coated with pVIII as it passes through this channel (Rakonjac & Model, 1998). This complex interplay requires the correct relative concentrations and functional integrity of all components to succeed. The success of the 8+8 hybrid display system relies on incorporating both WT and recombinant coat proteins (G.P. Smith, V. Petrenko, 1997). This is especially crucial for pVIII, which forms the main structural protein of the virion with approximately 2700 copies. Fusing peptides, particularly those larger than 8-10 amino acids, to pVIII compromises its structural function and can prevent phage assembly (Hess et al., 2012). In this frame, the supply of a WT pVIII is essential since it acts as a structural scaffold, allowing the less-stable modified pVIII molecules to be incorporated into the capsid without causing the entire assembly to fail.

In co-transformation, the simultaneous expression of modified and WT pVIII proteins can easily lead to a stoichiometric imbalance. An overabundance of structurally modified pVIII can interfere with the assembly machinery, leading to improperly formed or non-viable phage particles. In contrast, the superinfection method provides a more temporally regulated sequence: the host cell is first established with the phagemid before being infected by the helper phage, which supplies the WT coat proteins. This staggered timing may create a more favourable balance of functional and modified components, promoting efficient assembly, explaining our experimental findings.

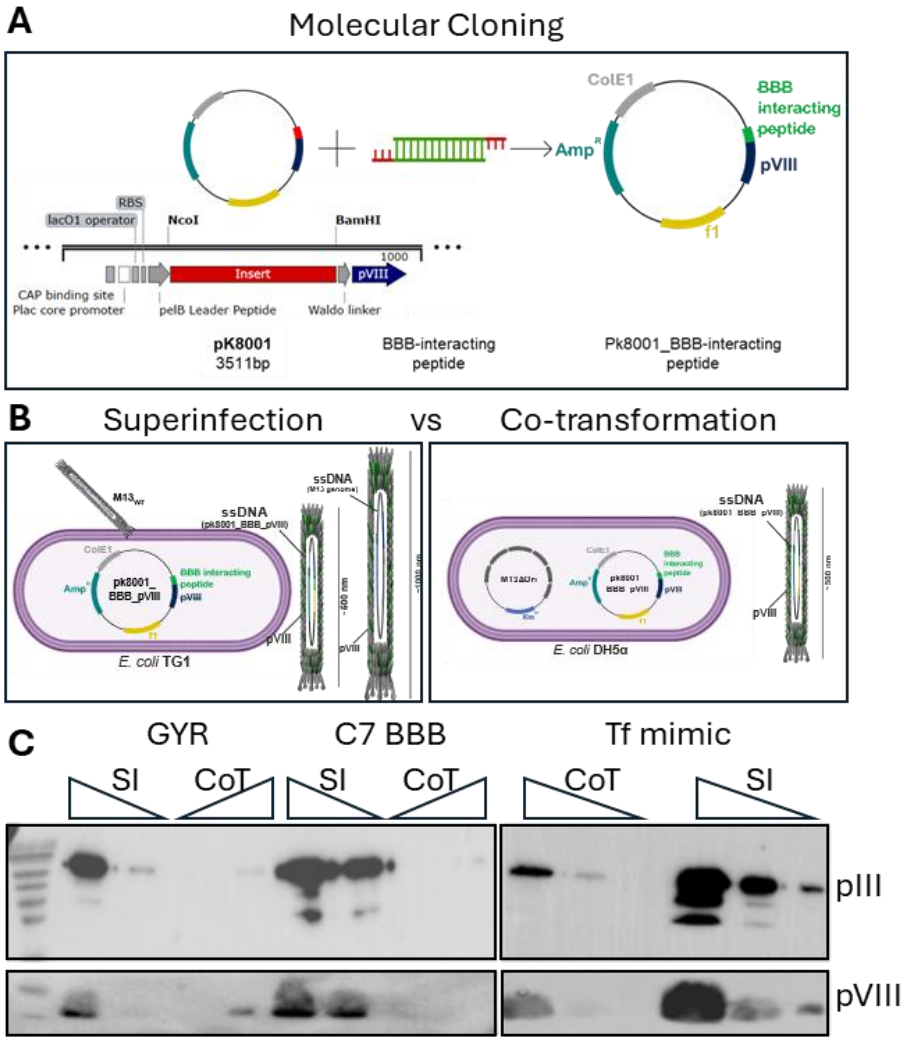

Figure 8: ***(A)*** *Schematic representation of the molecular cloning workflow used to generate BBB-interacting phages. Oligonucleotides encoding the BBB-interacting peptide were annealed and cloned into the pk8001 phagemid in frame with the pVIII phage protein.* ***(B)*** *Schematic of the two production methods for BBB-interacting phages. Left: Superinfection, in which TG1 E. coli cells were transformed with the pk8001_BBB interacting peptides phagemid and subsequently infected with the wild-type helper phage. Right: Co-transformation, in which DH5α E. coli cells were simultaneously transformed with the the pk8001_BBB interacting peptides phagemid and the M13K07Δori helper phagemid.* ***(C)*** *Western Blot analysis of BBB-interacting phages produced by superinfection (SI) or co-transformation (CoT). GYR and C7 phages showed detectable pIII and pVIII expression only with SI, whereas Tfm phages produced very low levels of pIII and pVIII also under CoT conditions.*

After observing the inefficient production of BBB-interacting phages via the co-transformation method, we proceeded to assess the quality and stability of phages produced using the superinfection method. To evaluate their structural integrity over time, we utilised differential ethidium bromide staining, a technique designed to verify that the phage's DNA genome is correctly encapsulated and protected within its protein capsid (Fig. 9 A).

The procedure involves comparing two samples of the same phage preparation on an agarose gel: one is loaded as it is, while a control sample is heat-denatured by boiling. This treatment

disrupts the capsid's protein structure, causing it to release its DNA. Following electrophoresis and initial staining with ethidium bromide, the results distinguish between the two states. The band for the intact phages appears dim or invisible because the encapsulated DNA is shielded from the dye. Conversely, the denatured sample, containing exposed DNA, binds the ethidium bromide, producing a bright band. Following the first staining, the entire gel is treated with an alkaline solution, such as NaOH, which chemically denatures the remaining intact virions and releases their genomic content. After re-staining, the band corresponding to the initially intact phage sample also becomes bright. This method was subsequently used to compare the stability of the virions immediately after production (Day 0) with their state 15 days later, to confirm their structural integrity over time. As shown in Figure 9 A, all three BBB-interacting phages were confirmed to be intact at day 0. Crucially, at day 15, the continued presence of a very faint band prior to alkaline treatment confirmed their sustained stability. This outcome confirmed that the phages were structurally stable and had been properly assembled, validating the use of a single batch for multiple experimental replicates without concerns about degradation.

Consequently, the three modified phages were sent to our collaborators at IIT to be subjected to a 2D BBB crossing experiment. Following the established protocol, an endothelial cell monolayer was grown on a transwell insert to form a tight barrier. The phage solution was then added to the apical compartment, and at different time points, aliquots from the BL fractions were collected to quantify the number of translocated virions via fluorescence exploiting their conjugation with a fluorophore (Fig. 9B). The quantity of translocated phages is reported both as the absolute virion number in BL and as a percentage of the total phages initially added (Fig. 9B). The results clearly demonstrate that the $M13_{BBB\text{-}interacting}$ phages cross the in vitro model significantly more efficiently than the $M13_{WT}$ phage. Notably, their translocation percentage at 72 hours was comparable to that of the WT phage crossing a low-density, non-confluent barrier, confirming their enhanced crossing capability.

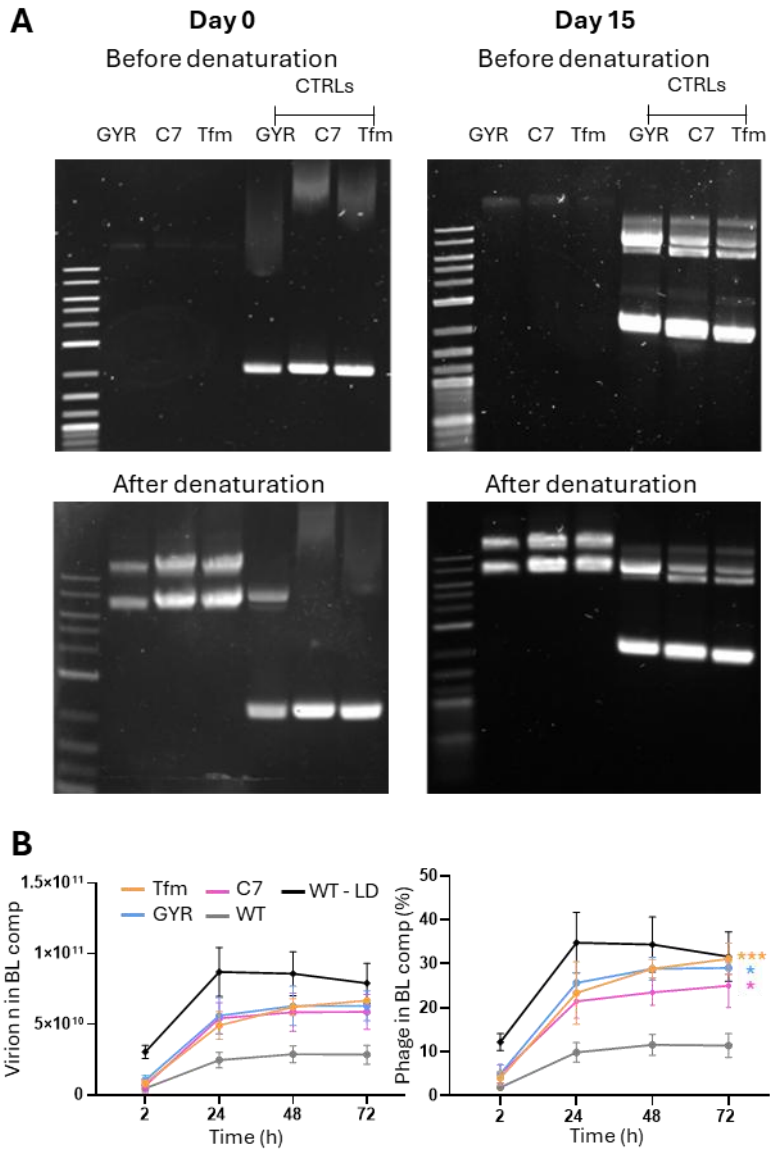

Figure 9: ***(A)*** *Agarose gel electrophoresis of the differential ethidium bromide staining assay. At day 0 and day 15, prior to chemical denaturation, only faint bands were detected for the three phage samples (GYR, C7, Tfm), whereas strong bands were observed for the denatured controls. Following chemical denaturation, strong bands also appeared for all samples, confirming the presence of DNA encapsulated within intact capsids in the initial gels.* ***(B)*** *Quantification of phage translocation across the BBB in the 2D crossing assay, expressed as the total number of virions detected in the BL compartment and as the percentage of translocated phages relative to the initial apical inoculum. All three BBB-interacting phages crossed the BBB significantly more efficiently than WT, with values at 72 h approaching those of WT phages in low-density Transwell conditions (dataset collected at IIT).*

Overall, considering the WB data confirming successful production and assembly, the structural stability over time verified by the differential ethidium bromide assay, and, most importantly, the highly enhanced ability to cross the 2D BBB *in vitro* model, the Transferrin mimic (Tfm) phage emerged as the best candidate.

These results, while preliminary, are highly promising and pave the way towards developing an effective phage-based nanoplatform capable of entering the CNS in a non-invasive and efficient manner. Of course, the platform has broad range of optimisation, and further experiments are necessary to improve its BBB-crossing ability. Potential improvements could include enhancing the number of displayed peptides. Crucially, its ability to cross more complex 3D *in vitro* and in *vivo* BBB models must also be assessed to fully validate its potential.

3.3 Nanobody-ALFA phage engineering as proof of concept for a specific neuronal targeting platform

By leveraging phage display technology, M13 coat proteins can be modified to present targeting ligands such as peptides, nanobodies, or single-chain antibodies on the virion surface. Previous studies have demonstrated that engineered M13 phages displaying a modified pIII fusion protein can effectively and specifically target desired cell populations, from cancer cells to bacteria (Bortot et al., 2022; Ghosh, Lee, et al., 2012; Hess et al., 2012; Turrini et al., 2024). This capability makes them ideal candidates for delivering therapeutic payloads while minimising off-target effects in hard-to-reach districts of the human body.

To investigate whether a modified M13 phage retains its targeting capacity after crossing our BBB *in vitro* model, we developed a synthetic targeting platform. This system comprises an engineered phage targeting the ALFA tag by means of a specific Nanobody (Götzke et al., 2019), aka $M13_{Nb\alpha}$, and a corresponding synthetic target, the ALFA_hCD4_mOrange construct allowing extracellular display of the ALFA tag upon transfection.

To generate the retargeted phage $M13_{Nb\alpha}$, the M13 phage genome was engineered to display five copies of an anti-ALFA Tag nanobody on its pIII minor coat protein. We employed a robust type 3 phage display strategy based on the pComb3XSS phagemid (Addgene plasmid #63890) in which we cloned the coding sequence for the anti-ALFA nanobody in-frame with the C-terminal domain of the pIII protein. For virion production, the co-transformation method represented in Fig. 10 A was utilized. *E. coli* DH5α cells were simultaneously transformed with the engineered pComb3XSS_Nb-ALFA phagemid and the Hyperphagemid M13K07Δp3Δori. This helper is critical as it provides all the necessary proteins for phage assembly but lacks a functional pIII gene. This design ensures that the pIII protein is exclusively supplied by the phagemid, resulting in a homogenous population of phage particles where all five copies of

pIII are fused to the anti-ALFA nanobody. Consequently, this system achieves a pentavalent display, which can significantly enhance target binding avidity. Following production and purification, the quality and integrity of the resulting $M13_{Nb\alpha}$ phage were rigorously assessed as previously described (Fig 10 B-C).

UV-Vis spectroscopy confirmed a high-yield production and sample purity after the conjugation with CF488, while TEM imaging performed by our IIT collaborators verified that the engineered virions maintained the correct filamentous morphology. Finally, to confirm the successful incorporation of the fusion protein, purified phages were analyzed by Western blotting. Probing with an anti-pIII monoclonal antibody revealed a distinct band at approximately 40 kDa, which corresponds to the expected molecular weight of the pIII-nanobody fusion protein, thus validating its correct expression and assembly into the phage capsid.

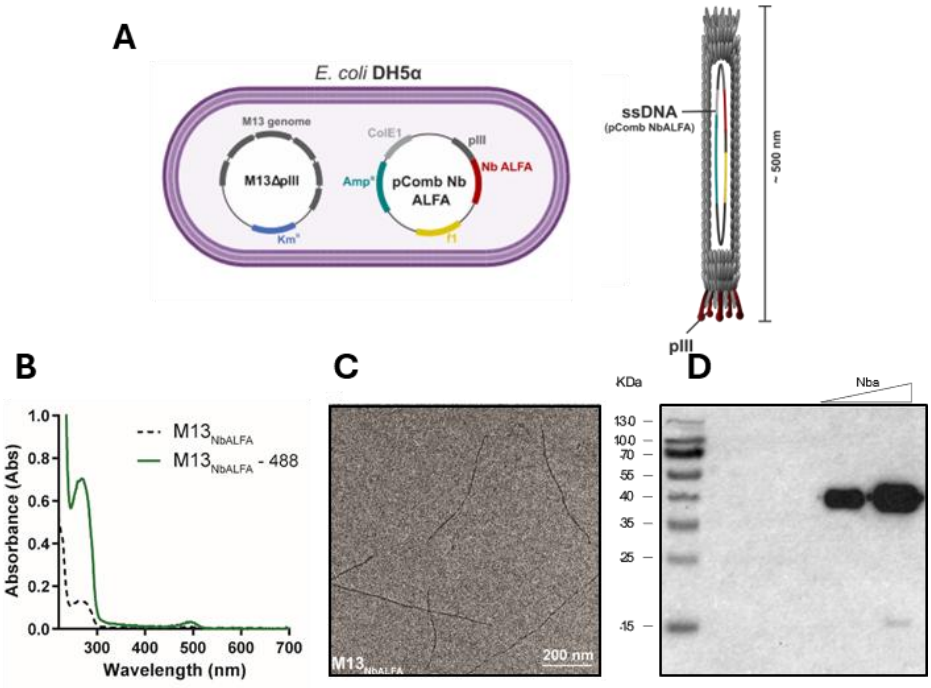

Figure 10: ***(A)*** *M13NbALFA was obtained through the co-transformation method, using a phagemid encoding for an anti-ALFA-Tag nanobody on the pIII protein and the helper phage vector HyperΔori in E. Coli DH5α cells.* ***(B)*** *Absorption spectrum of M13NbALFA before (dotted line) and after conjugation with CF488 (full green line).* ***(C)*** *Representative TEM micrographs, with high magnification insets, illustrating the structure of M13Nbα (data acquired at IIT).* ***(D)*** *Immunoblot analysis of phage pIII coat protein M13NbALFA, confirming that the pIII protein in M13NbALFA was successfully engineered.*

After the successful production and validation of the engineered Nbα phage, the next step was to generate a synthetic target to validate its binding specificity in a cellular context. This was achieved through the molecular cloning of the ALFATag_hCD4_mOrange construct, using the

human CD4 receptor as a transmembrane scaffold (Fig. 11 A). Fused in-frame to its intracellular domain is the mOrange fluorophore, which serves as a reliable reporter to visually confirm successful expression of transformed cells. Crucially, the short ALFA-Tag peptide was cloned in frame within the extracellular domain, presenting a specific epitope recognised by $M13_{Nb\alpha}$. This construct was then used to transfect primary mouse cortical neurons at DIV 7 using Lipofectamine 2000 as transfection agent. This reagent was chosen for its relatively low transfection efficiency in primary neurons, resulting in a sparse population of transfected cells among a majority of non-transfected ones. This experimental design is ideal for assessing targeting specificity, as it allows for the clear visualisation of any potential off-target binding to neighbouring negative cells. To perform the targeting experiment, the purified Nbα phage was fluorescently labelled with a CF488 dye. The transfected neuronal culture was then incubated with the labeled $M13_{Nb\alpha}$ - 488 phage solution for one hour.

The results were subsequently analysed using confocal microscopy (Fig 11 B). As hypothesised, a strong co-localisation was observed between the mOrange signal (magenta) of the ALFA-hCD4-mOrange protein and the fluorescent signal of the $M13_{Nb\alpha}$ phage (yellow). This binding was highly specific, occurring exclusively on the cell membranes of the few transfected neurons. Importantly, no phage signal was detected on the surrounding non-transfected neurons, confirming the high-specific targeting of the Nbα phage to its designated ALFA-Tag epitope. This experiment successfully validated the functionality of our synthetic targeting platform, setting the stage to test whether this specificity is retained after crossing the BBB.

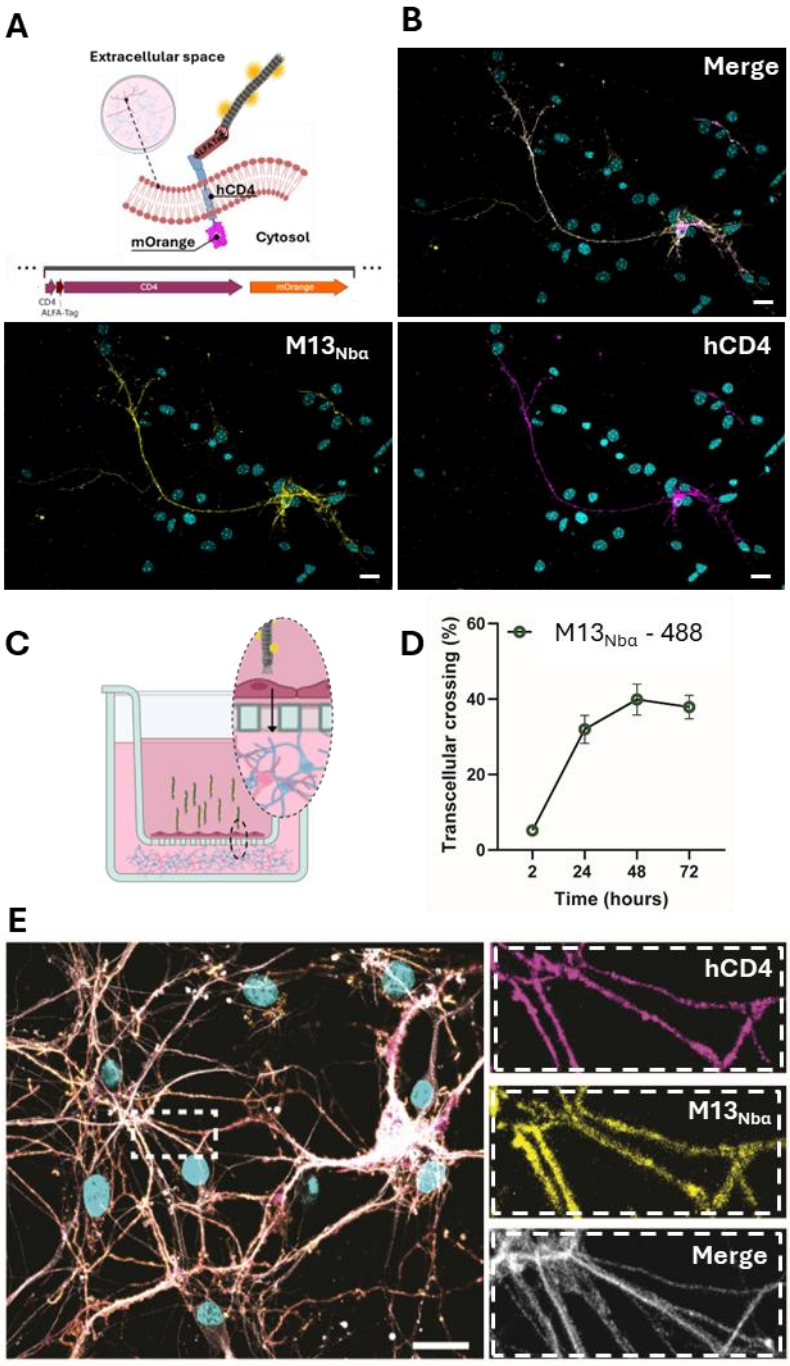

Figure 11: $M13_{Nb\alpha}$ targeting efficacy in murine primary neuronal cultures. ***(A)*** *Schematics of the model used to assess the $M13_{Nb\alpha}$ efficiency in neuronal targeting: primary neurons are transfected to transiently express human CD4 transmembrane protein carrying a intracellular fluorescent reporter (m-Orange) and an extracellular ALFA-Tag. After exposure to $M13_{Nb\alpha}$-488, efficient targeting is reflected by the co-localization between the m-Orange reporter (neurons) and the 488 label (phage).* ***(B)*** *Representative confocal image of primary cortical neurons expressing the ALFATag_hCD4_mOrange (magenta) after one-hour exposure to the $M13_{Nb\alpha}$-488 (yellow), showing a complete overlap of the two signals. No phage signal is visible in non-transfected neurons (cyan: nuclei, white:merge, scale bar: 20 µm).* ***(C)*** *Schematic of the "cross-ting" experimental setup: bEnd.3 cells form a 2D barrier on the transwell membrane, and primary neurons are placed in the basolateral compartment. $M13_{Nb\alpha}$-488 is added to the apical compartment, and the neurons are analyzed 72 hours later using a confocal microscope.* ***(D)*** *Quantification of $M13_{Nb\alpha}$ crossing by fluorescence in the crossting experimental setup, expressed as percentage of the total phage quantity in the apical compartment (5×10^{11} in 800 µL).* ***(E)*** *Representative confocal images showing an unaltered targeting efficiency of the $M13_{Nb\alpha}$-488 after crossing of the 2D BBB layer (magenta: CD4-AlfaTag, yellow: M13, grey: tubulin-ß3, cyan: nuclei, scale bar: 20 µm); courtesy of Silvia Vercellino – IIT.*

To this end, we designed a "cross-ting" (crossing + targeting) experiment using the *in vitro* 2D model of the BBB (Fig. 11 C). The experimental setup, consisting of a transwell system, was the same as the BBB crossing experiment extensively explained in section 3.1. Briefly, a confluent monolayer of murine brain endothelial cells was cultured on the porous membrane of the insert, forming a tight barrier that separates the apical and lower basolateral compartments. In the basolateral compartment, we cultured the primary cortical neurons previously transfected with the ALFATag_hCD4_mOrange construct as set for the targeting experiment. The fluorescently labeled $M13_{Nb\alpha}$-488 phage was then introduced into the apical compartment. This configuration ensured that the phage had no direct access to its neuronal targets and was first required to actively translocate across the endothelial cell layer. This setup tests two key properties simultaneously: the retargeted phage's ability to penetrate the BBB model and its capacity to remain structurally and functionally intact throughout the process. After 72 hours of incubation, the neuronal culture was analysed by confocal microscopy.

The $M13_{Nb\alpha}$ -488 phage resulted to successfully cross the endothelial layer (Fig. 11 D) and bound with high fidelity to its target neurons in the basolateral compartment (Fig. 11 E). We observed a clear and specific co-localisation of the phage's fluorescent signal with the mOrange reporter on the transfected neurons. Once again, no binding was detected on neighbouring non-transfected cells, underscoring the remarkable specificity of the system.

This outcome is highly significant, as it confirms that the engineered Nbα phage not only possesses an intrinsic ability to cross the BBB, comparable to its wild-type counterpart, but critically, it retains its full targeting specificity after translocation. This validation of dual functionality, barrier penetration followed by precise cellular targeting, represents an important step, confirming the potential of the M13 phage platform as a robust and viable nanovector for targeted delivery to the CNS.

3.4 Orthogonal engineering of the M13 phage platform for the dual display of BBB-crossing and targeting moieties

The previously discussed results on M13 phage-based platforms, designed either for enhanced BBB translocation or for specific cell targeting, underscore their considerable potential in nanomedicine. These findings emphasize the versatility of filamentous phages as modular scaffolds that can be engineered with tailored ligands to overcome key barriers in drug

delivery. A particularly promising direction is represented by the development of a phage-based orthogonal systems in which a single platform combines BBB interacting peptides that facilitate efficient, non-invasive CNS entry, with cell targeting moieties ensuring precise recognition of pathological cells, addressing multiple biological obstacles simultaneously. This capability is especially relevant for conditions affecting hard-to-reach body compartments, such as neurodegenerative diseases in the brain, or for tumours within complex microenvironments, reducing off-target toxicity and mitigating the collateral damage often caused by conventional treatments.

To generate our orthogonal phage platform, we started from the molecular cloning of the targeting moiety and the BBB-interacting peptide into the phagemid vectors for phage display. As previously discussed, the Type 3 display system was retained for the targeting moiety; the Nbα was cloned in-frame with the C-terminal portion of the pIII protein within a validated phagemid, a method well-suited for displaying larger protein fragments.

For the display of the BBB-interacting peptide on the pVIII major coat protein, however, several distinct strategies were explored, each leveraging different display modalities (Fig. 12 A). The display of the Tfm peptide, one of the BBB interacting peptides previously discussed, on the major coat protein pVIII of filamentous phages offers a spectrum of valency options. The most deisderable of these is the Type 8 display system. In this configuration, the coding sequence of the Tf mimic peptide is cloned directly in-frame with the sequence of gene VIII within the M13K07 Δori ΔpIII hyperphagemid. This method would ensure that every copy of the pVIII protein is constitutively expressed as a Tfm-pVIII fusion (Henry et al., 2015). It eventually results in a fully recombinant virion with a high display valency of up to 2700 peptides. However, this high-density arrangement is only tolerated for very short peptides, as larger inserts disrupt the proper assembly and viability of the virion.

To overcome this constraint, the Type 88 display system was leveraged (G.P. Smith, V. Petrenko, 1997). In this configuration, the Tf mimic peptide was cloned in-frame with an additional copy of the pVIII coding sequence within the M13K07 Δori ΔpIII hyperphagemid. The resulting Tfm-pVIII fusion protein is constitutively expressed under the regulation of the M13K07 promoter, but it is not the only pVIII copy present, as the genome now carries both the WT and the engineered gene VIII. This produces a hybrid virion where the abundant WT pVIII proteins

provide structural integrity, allowing for the successful display of multiple copies of the Tfm peptide without compromising the virion's stability.

An even more versatile approach is the Type 8+8 phagemid system. As already discussed before, here the recombinant fusion protein is encoded on the pComb_Nbα phagemid, while an additional WT pVIII is supplied by the M13K07 Δori ΔpIII hyperphagemid, offering easier genetic manipulation and greater stability. The resulting virions are also mosaic, but the display level is typically lower and more controlled, making it an ideal choice for displaying complex proteins without compromising phage assembly. For this approach, we explored three distinct configurations, using inducible promoters to control the expression of the fusion proteins better.

The first option was a polycistronic coding sequence where both fusion proteins, Nbα-pIII and Tfm-pVIII, were expressed under the control of a single inducible Lac promoter (pLac). In this case, expression is controlled by the addition of isopropyl-β-D-1-thiogalactopyranoside (IPTG) to the culture medium, a widely used and validated approach in molecular biology.

The second and third approaches, however, involved cloning the fusion proteins into two separate cistrons, each regulated by a different inducible promoter. The first of these constructs, pComb_LNbα_RTfm, places the Nbα-pIII cistron under the control of the pLac promoter, while the expression of the Tfm-pVIII cistron is controlled by the rhamnose-inducible promoter (pRham). This promoter, which is less strong than pLac, is activated by the introduction of rhamnose into the culture medium.

The final approach, pComb_RNbα_LTfm, was designed considering the different promoter strengths, swapping the two promoters. In this arrangement, the stronger Lac promoter controls the expression of the Tfm-pVIII fusion protein, allowing for greater expression efficiency of a protein that already imposes a significant metabolic load on the bacterium. The expression of the Nbα-pIII fusion protein, present in only five copies, is controlled by the weaker pRham promoter and is, therefore, induced by the addition of rhamnose. This overall separation of genetic elements offers easier manipulation and greater stability, with the resulting virions being mosaic, making it an ideal choice for displaying complex proteins without compromising phage assembly.

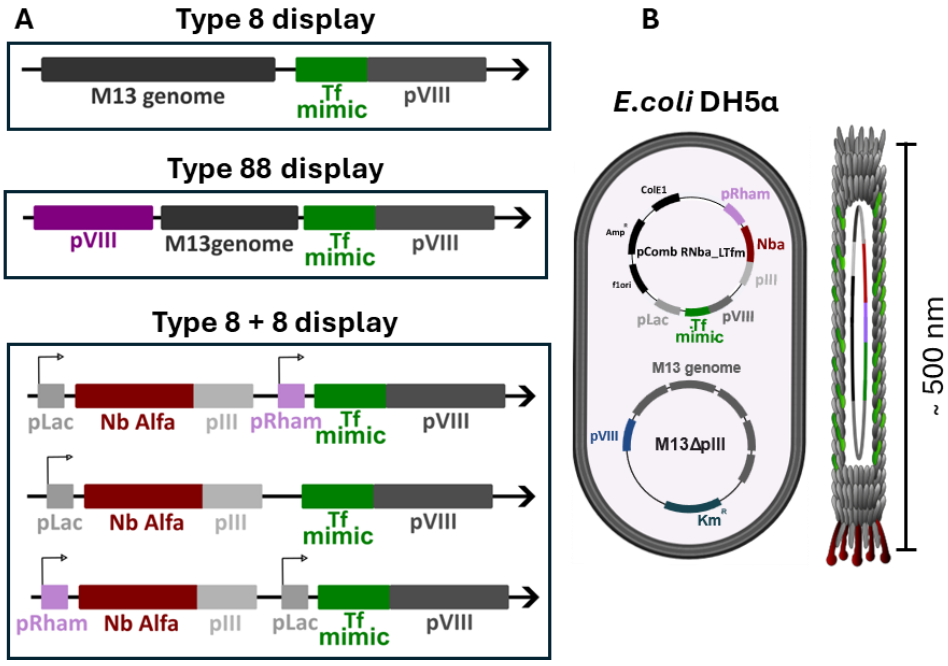

Figure 12: ***(A)*** *Schematic of DNA constructs for three types of pVIII display. In type 8 and 88, the peptide coding sequence is directly cloned into the M13K07 genome, giving higher display yield but reduced virion stability and no regulation. In type 8+8, the peptide sequence is inserted into a phagemid under an inducible promoter (different in each variant), resulting in lower yield but inducible and finely controllable display.* ***(B)*** *Cartoon representation of the phage production method. The genetically modified phagemid and the hyperphagemid are co-transformed into E. coli DH5α, producing orthogonally modified functional M13 virions.*

Our initial experimental strategy focused on three of these systems: the high-density Type 8 display and the two monocistronic Type 8+8 configurations. Following successful cloning and verification of all constructs via Sanger sequencing, we employed several techniques to validate phage production and compare their quality. The first critical quality control step was UV-Vis spectroscopy. A properly assembled M13 phage shows a characteristic spectrum with a distinct absorbance peak at a wavelength λ= 269 nm, which is a signature of the combined absorbance from the ssDNA genome and the aromatic amino acids within the coat proteins. As observed in Figure 13 A, the the orthogonal RNbα_LTfm phage (in blue) produced a spectrum that closely matches the WT control, displaying the clean, sharp peak at 269 nm indicative of a homogenous population of well-formed virions. In stark contrast, both the Hyper_Tfm phage (Type 8 display) and the LNbα_RTfm phage (Type 8+8 display) lacked a defined peak, instead showing a broad absorbance plateau between 220 and 300 nm before gradually decreasing. This result was consistent with the known low efficiency of the Type 8 display system.

The Dot Blot analysis in Figure 13 B confirmed this failure at the protein level. For the Hyper_Tfm orthogonal phage, the expression of the Nba-pIII fusion protein was correctly regulated: it was successfully produced following induction with IPTG but was absent otherwise, as its coding sequence is under the control of the inducible Lac promoter. In stark contrast, this lack of pVIII expression was independent of IPTG, which is logical since its gene is not controlled by an inducible promoter, confirming a fundamental weakness in its production in this configuration.

Having excluded the Hyper_Tfm phage due to its production inefficiency, we focused on the validation and optimisation of the Type 8+8 display. In the two systems analysed, both fusion proteins are provided by a phagemid and are controlled by two different inducible promoters: pLac, the IPTG-induced lac operon promoter, and pRham, induced by rhamnose. These operons differ significantly in strength; pLac is known for driving high levels of protein production when induced, whereas pRham is a weaker promoter used for finer expression control, yielding lower protein levels. As shown in the dot blot in Figure 13 C, when pVIII expression is under the control of the Lac operon, its production is far more efficient, resulting in a higher quantity of protein.

Following this analysis and considering the spectral data (Fig. 13 A), we decided to proceed with the further optimisation of the RNbα_LTfm phage, in which the Nba-pIII protein is controlled by pRham, while the Tfm-pVIII protein is driven by the stronger pLac promoter. To this end, the induction of Tfm-pVIII expression was considered optimal at 0.4 mM IPTG, while for the Nbα-pIII protein, several rhamnose concentrations were tested to optimise its production. Previously, concentrations of 100 mM and 50 mM had failed to adequately induce protein expression, a deficiency reflected by the absence of a phage pellet after PEG/NaCl precipitation during the purification process. Paradoxically, it is knowns that in *E. coli* higher transcription levels may lead to excessively elevated protein expression, which in turn can impair proper folding (Bhatwa et al., 2021). As a result, the protein may fail to remain monodisperse and instead form aggregates, often accumulating as inclusion bodies that interfere with the correct expression of the target proteins and the proper assembly of recombinant virions. Subsequently, two new concentrations were tested: 10 and 5 mM. In this case, as is evident from Figure 13 D, protein induction under both conditions was effective for the assembly of functional virions. Indeed, the UV spectra of the 10 mM rhamnose and 5 mM

rhamnose orthogonal phages do not differ significantly from each other or from the standard WT phage spectrum.

Therefore, the optimal induction conditions for the production of the RNbα_LTfm orthogonal phage, from now on Orthogonal – 5/10 mM, are 0.4 mM IPTG for the Tfm-pVIII cistron under the control of the Lac promoter, and 5–10 mM rhamnose for the Nba-pIII cistron under the control of rhamnose promoter.

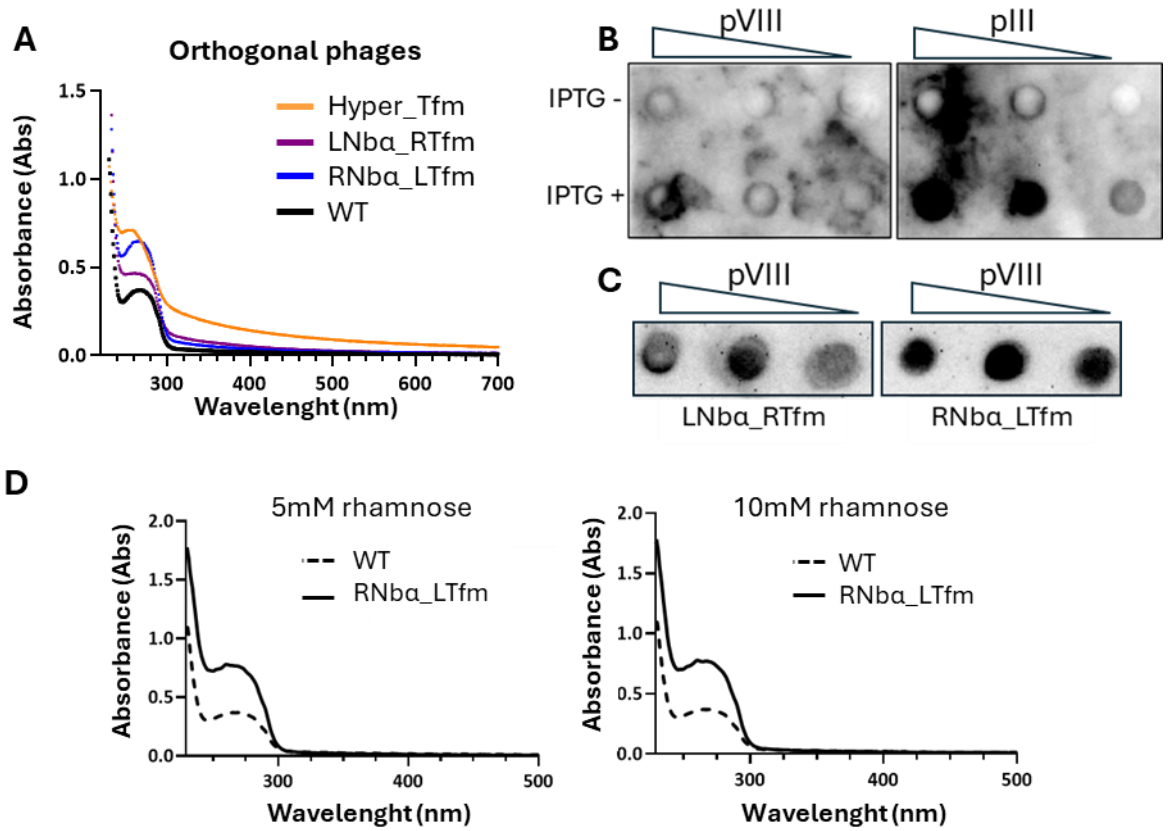

Figure 13: Orthogonal phages charachterisation: ***(A)*** *UV spectra of M13 phages. Black: WT phage; colored lines: orthogonal phages, reflecting different generation efficiencies.* ***(B)*** *Dot blot analysis of the Hyper_Tfm phage. On the left, detection of the pVIII protein; on the right, detection of the pIII protein with and without IPTG induction. While pIII expression is clearly regulated by IPTG, pVIII should be present under both conditions but is absent, highlighting the low efficiency of this strategy.* ***(C)*** *Dot blot analysis of pVIII expression. On the left, the LNba_Rtfm construct; on the right, the RNba_LTfm construct. The results confirm RNba_LTfm as the most efficient system.* ***(D)*** *UV-Vis spectra of RNba_LTfm phages induced with 5 mM and 10 mM rhamnose. Both spectra closely resemble WT.*

Following the successful characterisation and production optimisation of the orthogonal HR and LR phages, both were tested by our IIT collaborators for their ability to cross the BBB and target the ALFA tag on transfected neurons. The “cross-ting” system, previously described in section 3.3, was employed to compare the behaviour of the orthogonal phages with the WT phage across the 2D BBB system and on transfected primary mouse cortical neurons. Figure

14 A shows a representative graph of the TEER values measured before, during, and after the experiment to ensure the viability of the bEnd.3 cells and thus the integrity of the BBB. As is visible, the TEER values remained above 10 $\Omega \cdot cm^2$ for the entire duration, confirming once again that the phages are harmless to endothelial cells. As in previous experiments, a solution of $5x10^{11}$ phages/mL was incubated in the apical compartment of the system, where the bEnd.3 cells are cultured to form the barrier. At time points of 2, 24, 48, and 72 hours, the translocation of phage into the basolateral compartment was quantified, taking advantage of the CF488 fluorophore previously conjugated to the phage capsid.

As shown in Figure 14 B, this quantification is expressed both as a fold-increase over the autofluorescence of the untreated sample and as a percentage of the total phage added to the apical compartment ($5x10^{11}$ in 800 µL). In both metrics, the passage of the orthogonal phages was significantly greater than that of the WT phage at all time points, with the orthogonal-5 mM rhamnose phage proving slightly more effective than its 10 mM counterpart. Meanwhile, the primary neurons transfected with the target construct were cultured in the basolateral compartment. One hour after the addition of the phage, the neurons were visualised using confocal microscopy to assess the colocalisation of the target with the orthogonal phage. As seen in the images (Fig. 14 C), both the orthogonal-5mM (left) and -10 mM (right) phages were able to target the transfected neurons after crossing the 2D BBB model.

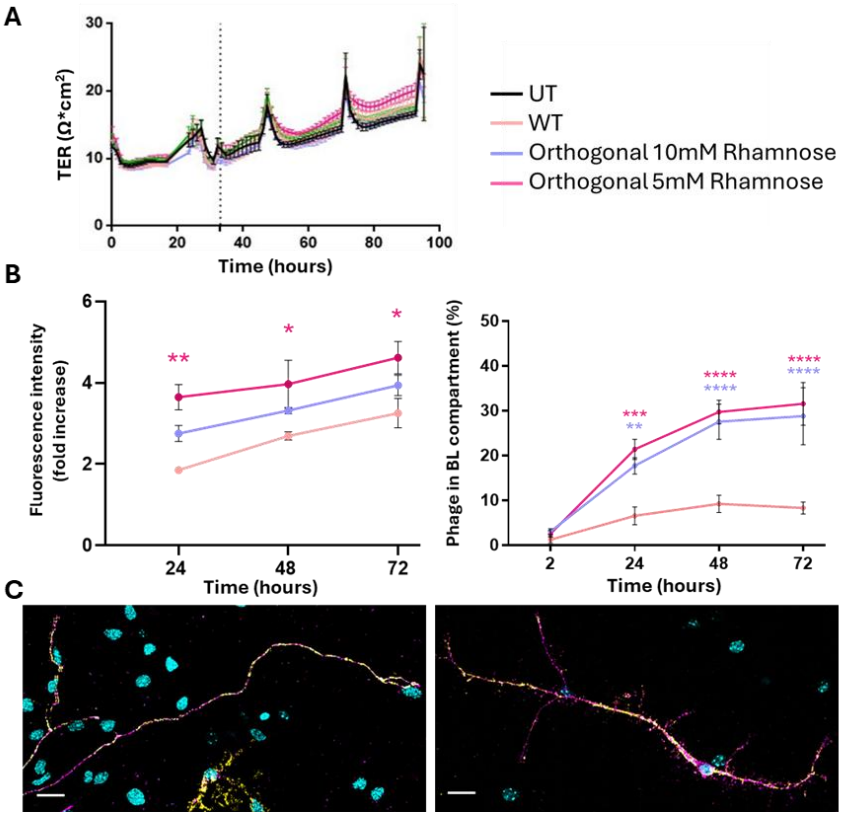

Figure 14: "Cross-ting" experiment with orthogonal phages performed by IIT collaborators: ***(A)*** *Representative TEER values from one replicate of the crossing experiment, measured before, during, and after the assay, consistently remaining above 10 Ω·cm². (B) Quantification of phages in the basolateral compartment (N=5), expressed both as fold increase in fluorescence relative to the untreated control and as a percentage of the total phages present in the apical compartment. The pink line represents the WT phage, while the blue and magenta lines correspond to the orthogonal HR and LR phages, respectively. (C) Targeting of transfected primary mouse cortical neurons by orthogonal phages after crossing the 2D BBB model. Orthogonal LR phages are shown on the right, Orthogonal HR phages on the left. Cyan: nuclei; magenta: mOrange; yellow: orthogonal phage. Scale bar: 20 µm.*

These certainly still preliminary but promising experimental results allowed us to conclude that is possible to orthogonally engineer an M13 phage to display two different functional proteins of interest on its capsid in a relatively simple and cost-effective manner. In this platform, a targeting moiety and a barrier-crossing moiety were successfully integrated, creating a nanovector with dual functionality.

The engineered orthogonal phages demonstrated a significantly greater ability to cross an *in vitro* 2D blood-brain barrier model compared to the WT phage, without compromising barrier integrity. Critically, after translocation, the phages retained their capacity to specifically target the intended neuronal cells. This confirms once again the platform's potential for addressing the pressing challenge of specific, non-invasive delivery of therapeutic molecules to regions like the CNS, which remain difficult to access with current technologies.

3.5 Application cases: Parkinson’s disease and Glioblastoma

The Neurophage project was originally conceived with an ambitious goal: to generate a minimally invasive, cell-specific therapy for Parkinson's Disease. The therapeutic strategy aimed to counteract the progressive degeneration of the nigrostriatal dopaminergic pathway, whose disruption leads to the inactivation of D1-dopaminoceptive neurons in the brain’s “direct pathway” and results in severe motor impairments (Luo et al., 2025). The core of this proposed treatment was a novel hybrid bio-nano construct, combining two key elements:

- the engineered M13 bacteriophage serves as a nanocarrier, designed to cross the BBB and deliver its payload specifically to D1 neurons.
- photovoltaic polymer nanoparticles (NPs) conjugated to the phage.

These NPs, made from materials like PCPDTBT, are engineered to absorb external energy from highly penetrant near-infrared (NIR) light or ultrasound (Maya-Vetencourt et al., 2020). When stimulated non-invasively through the skull, the NPs convert this energy into a signal that directly excites the targeted neurons. This innovative approach aims to remotely reactivate the direct pathway to rescue motor function. By achieving targeted neural modulation without surgery or genetic modification, the Neurophage platform was designed to outperform highly invasive treatments like Deep Brain Stimulation and optogenetics (Luo et al., 2025; Niazi, 2023).

However, the transition from concept to practical implementation was impeded by significant technical hurdles. While initial challenges involved the structural complexity of conjugating nanoparticles to the phage's filamentous morphology, a more fundamental obstacle emerged with the targeting strategy itself. The project's success was critically dependent on achieving high-specificity binding to the D1 dopamine receptor. This was critically hampered by the lack of known antibodies or nanobody sequences that recognise the receptor's extracellular loop, compromising the cell-specific delivery essential for an effective therapy.

Despite this decisive setback, it was clear that the platform’s core strengths should not be abandoned. The engineered phage's demonstrated potential to efficiently target cells of interest and cross the BBB remained a powerful and valuable asset for treating other central nervous system diseases where delivery is the primary therapeutic obstacle. Consequently,

the project was strategically pivoted away from neurostimulation to confront one of the most significant challenges in modern oncology: glioblastoma (GB).

Glioblastoma is the most common and most aggressive primary malignant tumour of the central nervous system in adults, accounting for about 15% of all brain tumours. Its annual incidence is approximately 3 cases per 100000 persons, and the prognosis is dismal: despite maximal surgical resection, radiation, and chemotherapy, the median survival time remains 12–15 months from diagnosis, with a 5-year survival rate below 5% (Alessandrini et al., 2019; Pagani et al., 2025). GB is characterised by rapid cellular proliferation, diffuse infiltration into surrounding brain tissue, marked heterogeneity at the molecular, cellular, and spatial levels, and a strong propensity for recurrence even after aggressive therapy (Appolloni et al., 2021). This is largely due to the BBB, which severely restricts the systemic delivery of nearly all therapeutic agents to the tumour site. To address this, our strategy aimed to leverage the synergy between the localised precision of phage-mediated photodynamic therapy (PDT) and the systemic power of Immunogenic Cell Death (ICD) (Bortot et al., 2022; Turrini et al., 2024; Ulfo, Cantelli, et al., 2022; Zadran et al., 2025). PDT utilises light-activated photosensitizers to generate cytotoxic Reactive Oxygen Species (ROS) within the tumour, inducing a regulated form of cell death that releases immunostimulatory Damage-Associated Molecular Patterns (DAMPs) (Catanzaro et al., 2022; Krysko et al., 2012; Turubanova et al., 2019). This process effectively transforms the tumour into an in situ vaccine, capable of priming a specific and long lasting adaptive immune response against malignant cells (Kepp et al., 2014). The M13 phage platform, with its proven BBB-crossing capability, is an ideal nanovector to execute this advanced therapeutic strategy.

The overarching goal we aim to achieve is to fuse the advanced capabilities of this M13 phage-based photo-oncolytic platform, its precision targeting, deep tissue penetration, and its demonstrated potential to reverse therapeutic resistance, with the phage-based platform ability to access the brain. By delivering a high payload of photosensitizers directly to GB cells and initiating a potent, localised ICD, this approach aims to not only ablate the primary tumour but also to generate a robust, systemic anti-glioma immunity, offering a transformative therapeutic strategy for this severe disease.

Our recent work on neuroblastoma (Zadran et al., 2025) provides a powerful proof-of-concept for the precision and efficacy of such phage-based photo-oncolytic systems, by eingineering

the M13 phage to display an anti-GD2 antibody fragment, and achieving highly selective targeting and killing of GD2-positive tumour cells upon light irradiation. This nanovector demonstrated deep penetration into 3D tumour spheroids and efficacy in *in vivo* models. Those principles are directly translatable to glioblastoma by exploiting the modularity of the M13 platform, which allows for the straightforward substitution of the targeting moiety to engage prevalent GB oncomarkers, like the Epidermal Growth Factor Receptor Variant III (EGFR-vIII). It is a gain-of-function splice-variant of the EGFR receptor expressed almost exclusively in cancer cells. Because of its constitutive activation EGFR-vIII drives cancer growth without needing a ligand, conferring a significant growth advantage to the tumour. This aggressive oncogene is overexpressed in approximately 33.33% of GB cases and is associated with significantly shorter survival in patients (Yuan et al., 2025).

To adapt this therapeutic strategy to glioblastoma, we have employed M13^{7D12}-RB platform, a M13 phage-based platform that has been extensively characterised in our research group but is not yet published. The system's specificity is achieved by genetically modifying the phage to display the 7D12 nanobody on its tip, in fusion with the pIII protein. This modification endows the phage with a strong affinity for both human EGFR (hEGFR) and hEGFR-vIII receptors, as oncotargets.

For its therapeutic action, the phage is chemically rigged through the bioconjugation of the photosensitiser Rose Bengal (RB) to its pVIII major coat protein, effectively loading the nanovector with a high therapeutic payload of light-triggerable sensitizers. The resulting construct, M13$_{7D12}$ - RB, functions as a highly targeted agent for PDT. It fundamentally relies on three components: a photosensitizer, molecular oxygen, and light (Rodrigues et al., 2022; Turubanova et al., 2019). Upon light absorption, the photosensitizer is excited to its triplet state, transferring energy to molecular oxygen. This process primarily generates the highly reactive singlet oxygen through the Type II photochemical reaction, although Type I reactions can also occur, producing radical species like the superoxide radical (Dos Santos et al., 2019). These cytotoxic ROS rapidly react with and damage macromolecules, leading to lipid peroxidation and protein and DNA oxidation (Chio & Tuveson, 2017), resulting in cell death.

The core therapeutic strategy involves the selective delivery of RB to hEGFR-vIII-positive cells, followed by localised light irradiation. This external trigger excites the RB molecules, causing them to generate ROS that induces oxidative stress and targeted cell death. This represents a

modular and precisely controllable system where the cytotoxic effect is confined to malignant tissues and activated only when and where desired, minimising collateral damage.

In our work on human cancer cell lines, the platform demonstrated exceptional precision and efficacy; it selectively recognised and bound to EGFR-positive epidermoid carcinoma cells, even within mixed cell populations, while exhibiting no affinity for the EGFR-negative rhabdomyosarcoma cells. Crucially, the nanovector was shown to be safe and inert in the absence of light. Upon laser irradiation, however, it induced potent and highly specific cytotoxicity, eradicating over 80% of the targeted EGFR-positive cells while leaving the negative cells largely unharmed (Costantini et al. in preparation).

Leveraging these promising findings, our core objective was to determine if this potent, phage-mediated photoablation could induce an efficent immunogenic cell death (ICD) *in vivo*. In collaboration with the Cell Death Investigation and Therapy Laboratory of Professor Dmitry Krysko at the University of Ghent, we wanted to ask if this therapeutic action is able to ablate the primary tumour and also to generate a protective, long-term anti-tumour immune response. This would confirm the platform's ability to function as an in situ vaccine, a transformative therapeutic strategy for GB.

To evaluate the *in vivo* ability of the phage platform to induce ICD, the use of murine models is recommended. However, our targeting moiety, the 7D12 nanobody, is specific to human EGFR. Therefore, we first needed to investigate its potential cross-reactivity with murine EGFR (mEGFR). Although hEGFR and mEGFR share 91% overall structural homology, the homology within the extracellular domain, the epitope for the 7D12 nanobody, is lower, at only 88.34% (Figure 15 A). To experimentally assess this cross-reactivity, we incubated our engineered $M13_{7D12}$ phage with both the hEGFR-positive human cell line A431 and the murine glioma cell line GL261. As demonstrated by both immunohistochemistry and flow cytometry assays (Figure 15 B - C), the $M13_{7D12}$ platform exhibited strong binding exclusively to the human A431 cells, with no detectable binding to the murine GL261 cells. This lack of cross-reactivity was anticipated, given the significant divergence in the epitope regions between the human and murine receptors and the characteristic high specificity and avidity of nanobodies for their intended targets (Roovers et al., 2011).

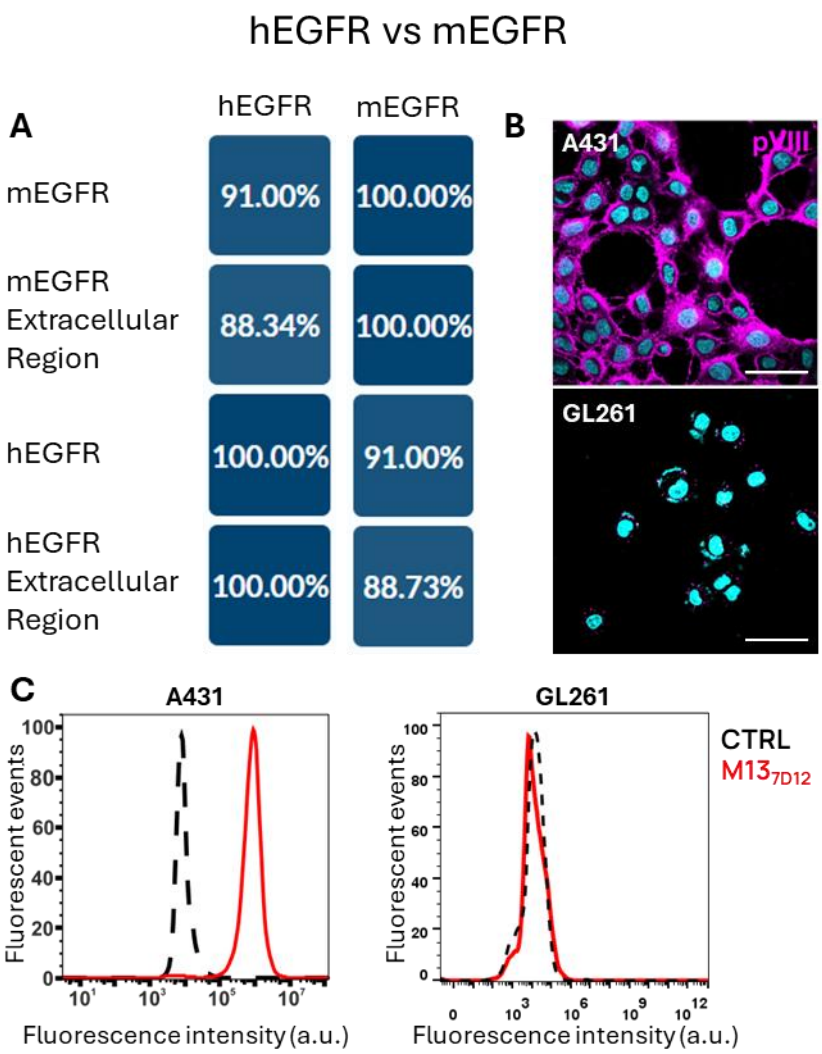

Figure 15: ***(A)*** *Matrix showing the percentage of sequence similarity between the human and mouse EGFR receptors and their extracellular regions (ECR). The full-length receptor sequences share 91% overall similarity, while the ECR alone shows 88.34% similarity.* ***(B)*** *Immunofluorescence assay targeting the pVIII protein on human (A431) and murine (GL261) EGFR⁺ cell lines, both incubated with the M13 7D12 phage platform. Binding was observed only in the human cell line. (Cyan: nuclei; magenta: pVIII. Scale bar: 50 µm).* ***(C)*** *Flow cytometry analysis of M13 7D12 phage binding to human and mouse EGFR receptors, expressed as fluorescence events versus fluorescence intensity.*

To address this lack of cross-reactivity and overcome the absence of a robust targeting mojety (scFv, Nb, *etc*) against mEGFR, we engineered a murine GL261 cell line to stably express the human target, hEGFR-vIII. This was achieved by transfecting the murine cell line with a plasmid encoding the hEGFR-vIII sequence, which also carried a Geneticin resistance cassette for selection. Non-viral transfection reagents, specifically Lipofectamine, and FuGENE® were chosen to avoid the complexities and higher biosafety requirements associated with viral vectors. Following transfection, the cells were subjected to continuous antibiotic selection

pressure with Geneticin to promote the genomic integration of the plasmid and establish a stably expressing cell line.

However, a technical challenge arose from the observation that GL261 cells are not compliant with single-cell cloning, as their viability is compromised at very low densities. The minimum seeding density that supported cell growth was approximately 12 cells per well in a 96-well plate, which precluded the isolation of a clonally derived population. Consequently, this process yielded a heterogeneous population comprising both hEGFR-vIII-positive and hEGFR-vIII-negative cells. Subsequent analysis by flow cytometry and immunohistochemistry confirmed this mixed composition, revealing that approximately 43% of the cell population expressed the target receptor and was specifically bound by the $M13_{7D12}$ platform (Figure 16 A).

The therapeutic efficacy of PDT is defined not only by its capacity to induce cell death, but crucially, by the immunological consequences of the death modality it triggers. A primary determinant of this outcome is the subcellular localisation of the photosensitiser, which is directly governed by the incubation time. This period allows the agent to traffic beyond the plasma membrane to distinct intracellular organelles, thereby pre-selecting the molecular pathways that will be targeted upon photoactivation (Turubanova et al., 2019). Complementing this spatial targeting, the irradiation protocol regulates the kinetics of the phototoxic effect. A moderate light dose facilitates a controlled oxidative stress that can initiate programmed cell death pathways like apoptosis, which are immunogenic. In contrast, an intense, overwhelming dose can lead to rapid membrane collapse and necrosis, a largely non-immunogenic outcome. Therefore, the interplay between incubation time and irradiation dose creates a tuneable system where the site and intensity of damage can be modulated. A thorough understanding of this dynamic is essential for rationally designing PDT protocols aimed not just at tumour ablation, but at the strategic induction of a potent anti-tumour immune response.

Building on these fundamental concepts, we tested the ability of our $M13_{7D12}$-RB platform to kill transfected GL261 cells (hEGFR-vIII +) via a mechanism compatible with ICD induction. We began by incubating the cells for 1 hour with a fixed RB concentration of 1 µM, after which we compared two irradiation times: 1 minute, our standard timing for this platform on human cell lines, and an extended 2-minutes exposure. Untreated non-transfected glioma cells and

transfected cells incubated with naked WT phage were used as controls. As shown in Figure 16 B, the cytotoxic effect, assessed 24 hours post-irradiation, was only marginal following a 2-minutes irradiation and was not significant for the 1-minute exposure. While this limited efficacy could be attributed to several parameters, we hypothesised that it was primarily a consequence of suboptimal PS cellular localisation resulting from the short incubation time. To investigate this, we re-evaluated the killing effect of the $M13_{7D12}$-RB phages by maintaining the 1 µM RB equivalents concentration and 2-minutes irradiation, but now comparing the standard 1-hour incubation with a prolonged 24-hour period. Following a 24-hour recovery from irradiation, cell viability was again quantified using a viability dye and flow cytometry. While this assessment resulted in a cell viability of 56.7% with the 24-hour incubation, the 1-hour incubation surprisingly yielded a more potent effect, reducing viability to 40%, a level of cytotoxicity far greater than observed in the previous experiment (Figure 16 C).

At this point, we hypotesised that the high variability in our data was unlikely to be linked solely to the standard parameters influencing PDT efficacy and ICD induction. We therefore speculated that a significant contributing factor was the non-homogeneous nature of our transfected cell population.

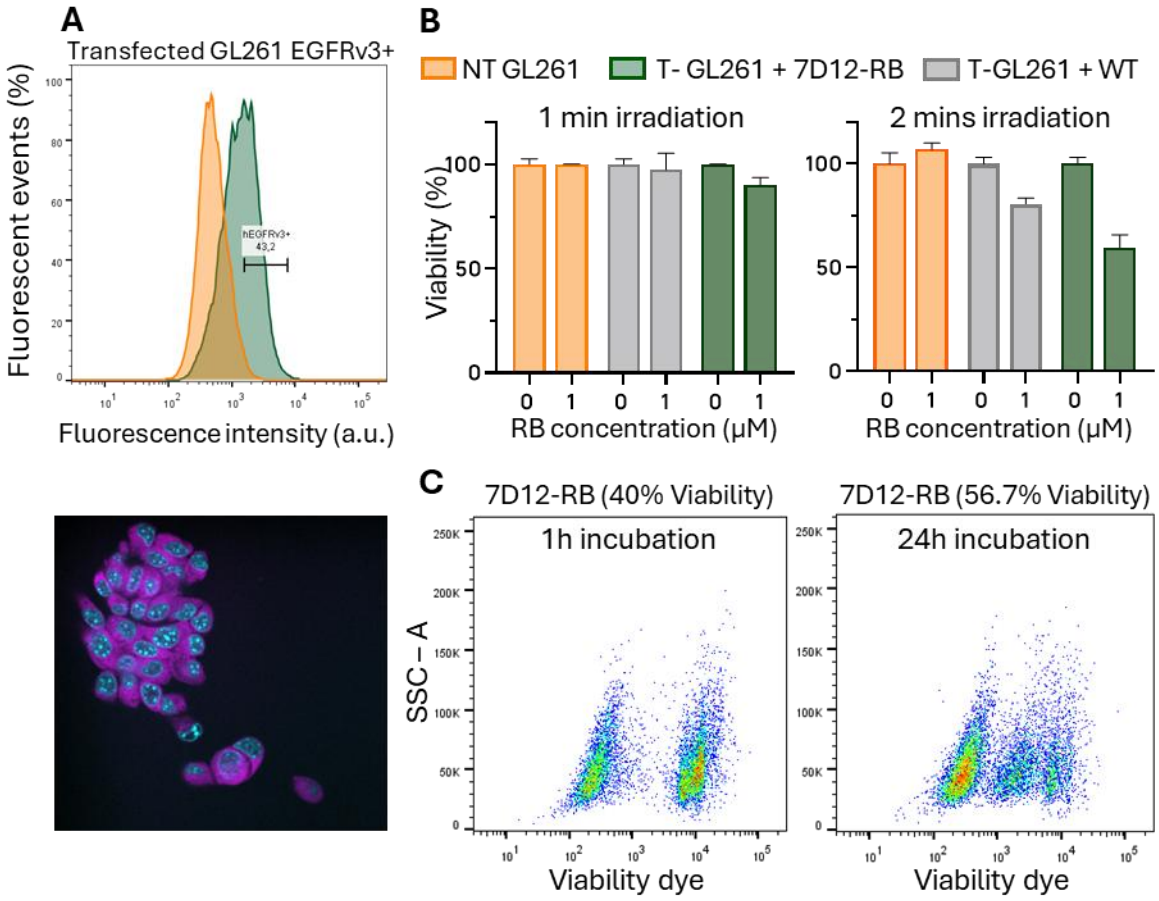

Figure 16: ***(A)*** *Flow cytometry and immunohistochemistry analysis of $M13_{7D12}$ phage binding to murine GL261 glioma cells stably transfected with the human EGFR-vIII receptor. Approximately 43.2% of transfected cells were bound by the platform (green peak) compared to the non-transfected GL261 cells (orange peak).* ***(B)*** *Cell viability assay on murine GL261 cells treated with the $M13_{7D12}$ – RB platform ([RB] = 1 μM) and exposed to different irradiation times (1 min, left; 2 min, right). In both cases, the cell viability after treatment (green) was not significantly different from either the untreated non-transfected control (orange) or the transfected control treated with WT phage (grey).* ***(C)*** *Flow cytometry assay assessing the viability of transfected GL261 cells treated with the M13-7D12–RB platform ([RB] = 1 μM) for 1 h (40% viability) or 24 h (56.7% viability). The viability dye Sytox Blue binds to the DNA of dead cells with disrupted membranes, producing an increased fluorescent signal proportional to the number of dead cells in the sample.*

To overcome this variability, we decided to sort the transfected cells to obtain a population as homogeneous as possible for hEGFR-vIII expression. Following the protocol described in the Materials and Methods section, we sorted the cells, achieving a yield of 10% and obtaining a final batch of 330785 cells. We first confirmed the binding of our platform to this purified population via flow cytometry. As shown in Figure 17 A, this resulted in a distinct peak shift in 85.7% of the cells compared to non-transfected controls treated with the $M13_{7D12}$. After expanding the sorted cells in culture, we repeated the 2D killing experiment. Maintaining the 1 μM RB equivalents concentration, we again tested 1-hour and 24-hour incubation times, combined with either 1 or 2 minutes of irradiation. Upon assessing cell viability after a 24-hour

recovery period, we observed markedly different dynamics. The 2-minute irradiation proved to be a highly aggressive treatment for this homogeneous hEGFR-vIII+ population, inducing 60% cell death after only a 1-hour incubation. The rapid kinetics of this killing suggested a non-controlled, necrotic pathway rather than the desired induction of ICD. Curiously, the 1-minute irradiation induced a slower, more progressive cell death mechanism that is more consistent with a controlled pathway. While slower to initiate, this condition ultimately proved more powerful, achieving 80% killing with a 24-hour incubation (Fig. 17 B). In order to confirm that this slower kinetic was indeed indicative of apoptosis, we proceeded to test for the externalisation of phosphatidylserine using an Annexin V assay.

Phosphatidylserine is a phospholipid that, in healthy cells, is strictly located on the inner leaflet of the plasma membrane, facing the cell's cytoplasm. During the early stages of apoptosis, this membrane asymmetry is lost, and phosphatidylserine is flipped to the outer surface, where it functions as an "eat-me" signal for phagocytes (Efimova et al., 2020; Krysko et al., 2012). Annexin V has a high and specific binding affinity for this exposed phosphatidylserine and, by using Annexin V conjugated to a fluorescent dye, it is possible to sensitively detect and quantify cells undergoing apoptosis via methods like flow cytometry.

We treated our cells with two different concentrations of RB (0.3 and 1 µM) for 1 or 24 h and irradiated them for one minute. After 24 hours recovery, we stained the cells with fluorescently-labelled Annexin V and Sytox Blue as viability dye to assess the cell death modality. Our analysis in Fig. 17 C revealed a progressive, dose-dependent increase in cells that were positive for both Annexin V and the viability dye. Specifically, in sorted GL261-hEGFRvIII^{+} cells treated with the M13$_{7D12}$–RB platform ([RB] = 0.3), incubated for 1 or 24 h and irradiated for 1 min, a double-positive (Annexin V^{+}/Viability Dye^{+}) population of 24.1% was detected with 24 h incubation. At 1 µM RB, this population increased markedly to 64.4%, confirming a dose-dependent enhancement of cell death. This double-positive staining pattern and its kinetics indicate that the cells not only exposed PS on the outer membrane leaflet but also lost plasma membrane integrity, consistent with late apoptotic stages.

While these results are preliminary, they strongly suggest that our treatment triggers a regulated form of cell death. The critical next step is to determine if this process qualifies as ICD. To achieve this, we plan to confirm the release of other key DAMPs, such as HMGB1 and extracellular ATP.

Furthermore, we want to assess our platform's ability to promote dendritic cell maturation in a co-culture system. These experiments will ultimately clarify whether the observed cell death is capable of initiating a productive anti-tumour immune response. This will be achieved by co-culturing the dying EGFRvIII-positive GL261 cells with immature bone marrow-derived dendritic cells (BMDCs). Maturation will then be assessed by using flow cytometry to analyse the expression of key surface markers, such as MHCII, CD80, and CD86. Additionally, the supernatant from the co-culture will be collected and the release of the pro-inflammatory cytokine IL-6 will be measured by ELISA to confirm the successful triggering of an immune-stimulatory response.

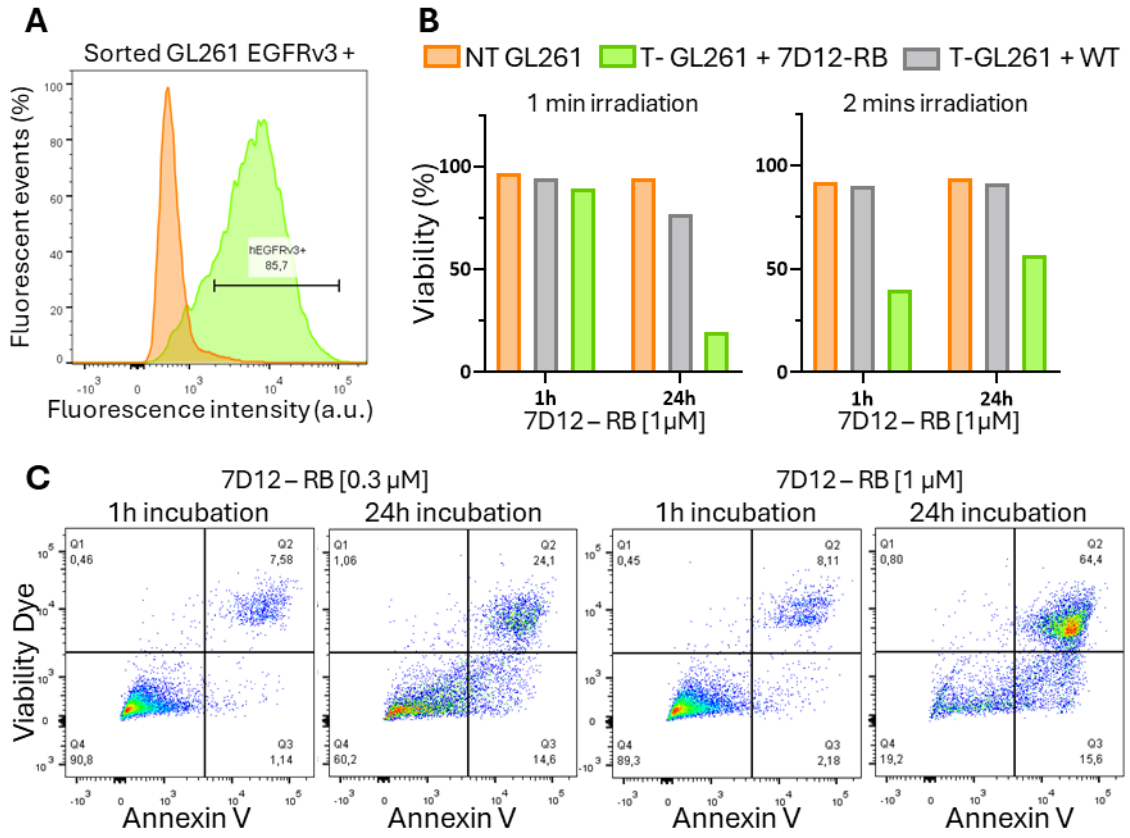

Figure 17: ***(A)*** *Flow cytometry analysis of $M13_{7D12}$ phage binding to murine GL261 glioma cells sorted after stably transfection with the human EGFRvIII receptor. A markedly increased fraction (85.7%) of the sorted, transfected cells was bound by the M13-7D12 platform (green peak) compared with the non-transfected GL261 population (orange peak).* ***(B)*** *Cell viability assay on sorted GL261-hEGFRvIII⁺ cells treated with the $M13_{7D12}$ – RB platform ([RB] = 1 µM), incubated for 1 h or 24 h and irradiated for 1 min (left) or 2 min (right). In both cases, cell viability after treatment (green) was significantly lower than in either the untreated non-transfected control (orange) or the transfected control treated with WT phage (grey). Notably, the dynamics of cell death differed between the two irradiation times: 1 min irradiation induced a slower, more regulated cell death profile, whereas 2 min irradiation caused rapid and potentially unregulated cell death in the homogeneous sorted population.* ***(C)*** *Annexin V assay of sorted GL261-hEGFRvIII⁺ cells treated with the $M13_{7D12}$ – RB platform ([RB] = 0.3 or 1 µM), incubated for 1 h or 24 h and irradiated for 1 min. After 24 h, treatment with 0.3 µM RB yielded a double-positive (Viability Dye⁺/Annexin V⁺) population of 24.1%, while 1 µM RB resulted in a substantially higher double-positive fraction of 64.4%.*

Despite the technical and theoretical challenges encountered in the development and repositioning of this platform, the results obtained are highly encouraging. They open up the possibility of making a tangible contribution to some of the most significant current challenges in nanomedicine and the treatment of CNS diseases. Our ultimate objective is to integrate our targeted PDT platform, $M13_{7D12}$, with the Neurophage platform extensively characterised in this thesis. This strategic fusion aims to create an efficient modular system capable not only of specifically targeting glioblastoma and delivering a high payload of PS to the tumor site, but also of enabling systemic administration, by orthogonally displaying BBB-interacting upon the phage, confering it an enhanced ability to cross the BBB and enter the central nervous system. Such an approach has the potential to significantly improve upon the highly invasive nature of current treatments for CNS pathologies, paving the way for safer and more effective therapies.

4. Conclusions

Effective drug delivery to the central nervous system represents a major and persistent challenge in modern medicine. The primary obstacle is the blood-brain barrier, a highly selective and dynamic interface that stringently regulates the passage of substances from the systemic circulation into the brain. While this barrier is crucial for protecting the delicate neural environment, it also severely impedes the entry of the vast majority of therapeutic agents; it is estimated that the BBB restricts over 98% of potential neurotherapeutics from reaching their targets in effective concentrations. This limitation poses a profound challenge for the treatment of CNS pathologies, rendering conventional systemic therapies largely ineffective for aggressive diseases such as glioblastoma and neurodegenerative disorders like Parkinson's disease.

The aim of this thesis was to engineer a novel nanocarrier capable of overcoming this barrier; to design a platform that could be administered non-invasively, efficiently reach and cross the BBBwithout causing disruption, and deliver its payload to specific cellular targets within the CNS. The M13 bacteriophage was selected as the foundational scaffold for this platform due to its unique structural and genetic properties.

Our investigation began by exploring a fundamental question: could the M13 phage, in its Wild Type form, traverse this barrier? Using BBB *in vitro* models, we observed that the phage could consistently penetrate a 2D endothelial monolayer, a process that did not compromise the barrier's structural integrity, as confirmed by stable trans-endothelial electrical resistance (TEER) values. Phages recovered after transit were found to be both structurally and functionally intact. This inherent, non-disruptive crossing mechanism was further confirmed in a more complex 3D multicellular assembloid model, establishing the M13 phage as a reliable platform for a CNS delivery system.

Building on this finding, we sought to enhance the phage's natural crossing efficiency. By employing phage display technology, we genetically modified the phage's major coat protein pVIII to present peptides known to facilitate BBB transit. The resulting engineered phages demonstrated a significantly improved translocation efficiency compared to the WT, confirming that the platform’s barrier-crossing capability could be rationally and substantially boosted.

A successful nanocarrier must combine CNS access with target specificity. To achieve this, we developed a synthetic targeting system by engineering the phage's minor coat protein pIII to display a nanobody against the ALFA-Tag, a specific molecular marker syntetically expressed on the surface of transfected primary cortical neurons. The engineered phage exhibited exceptional specificity, binding exclusively to ALFA-tagged neurons while showing no off-target interactions.

The culmination of this work was the generation of an orthogonally engineered platform that integrated both functionalities into a single nanovector. This dual-function phage was designed to display the Tfm peptide on its body for enhanced BBB transit and the anti-ALFA nanobody on its tip for a proof-of-concept neuronal targeting. In a combined "cross-ting" experiment, this platform first successfully traversed the 2D BBB model with high efficiency and then, upon reaching the basolateral compartment, retained its full capacity to specifically target the designated neurons. This demonstrated the successful creation of a modular nanoplatform capable of overcoming sequential biological barriers to achieve precise delivery.

The translational potential of this platform was explored in the context of glioblastoma. The system was adapted to deliver a photosensitiser (Rose Bengal) for Photodynamic Therapy, targeting the human EGFR-vIII receptor commonly overexpressed on glioblastoma cells. Initial experiments on engineered murine glioma cells showed that the platform could induce potent, specific, and controlled cell death via apoptosis upon light activation. This apoptotic pathway is consistent with the induction of immunogenic cell death, a process that can stimulate a systemic anti-tumour immune response.

In conclusion, this thesis details the successful design, engineering, and validation of a versatile M13 phage-based nanoplatform. We have demonstrated its capacity for non-disruptive BBB transit, which can be significantly enhanced through genetic modification, and its ability to perform high-specific cell targeting within a neuronal context. The integration of these functions into a single orthogonal system, and its promising application in a preclinical model of glioblastoma, provides a strong foundation for developing a new class of non-invasive, targeted therapies for diseases of the central nervous system.

5. Material and Methods

5.1 Cell cultures

5.1.1 Bacterial strains

Strain	**Description**	**Reference**
DH5α *Escherichia coli*	supE44 ΔlacU169 (ϕ80 lacZΔM15) hsdR17recA1 endA1 gyrA96 thu-1 relA1	(Hanahan, 1983)
TG1 *Escherichia coli*	K-12 ginV44 thi-1 Δ(mcrB-hsdSM)5, (rk mK-) F'[traD36 proAB+ laclq lacZΔM15]	Lucigen

The **DH5α *Escherichia coli*** cells are engineered to easily perform the white/blue screening and maximise the transformation efficiency through various mutations. The supE44 mutation makes this strain able to suppress amber stop codons.

The **TG1 *Escherichia coli*** strain has a high transformation efficiency, and it is ideal for the creation of large peptide libraries or phage display with the superinfection method.

These strains grow in suspension in Luria-Bertani medium (LB) or form colonies on LB-Agar (LBA) plates. The transformed cells were selected using the antibiotics carried by the transforming vectors, such as ampicillin(Amp) and kanamycin (Km), at a final concentration of 100 and 25 µg/mL, respectively.

5.1.2 Primary cells

Cells	**Description**	**Reference**
Primary murine cortical neurons	Primary neurons prepared from wild type C56BL/6 mice	C.C. Little, 1921

Primary cortical neurons were isolated from 18-day-old (E18) embryos of C57BL/6

pregnant mice, in accordance with the European Community Council Directive 2010/63/EU and approved by the Italian Ministry of Health. Pregnant mice were anaesthetised with CO_2 and euthanised via cervical dislocation. Embryos were delivered by caesarean section, decapitated, and their brains extracted into Hank's Balanced Salt Solution (HBSS). Under a stereomicroscope, meninges were carefully removed from the olfactory lobes, and cortices were dissected. Tissue was incubated in 5 mL of trypsin-EDTA at 37 °C for 30 minutes to facilitate dissociation. Following enzymatic digestion, 5 mL of Neurobasal medium supplemented with 2% B27, 1% Penicillin/Streptomycin, 1% GlutaMax, and 5% Fetal Bovine Serum (FBS) was added. The suspension was centrifuged at 1100 rpm for 5 minutes, the supernatant discarded, and the pellet resuspended in 5 mL of supplemented medium. A second centrifugation at 700 rpm for 5 minutes was performed, after which the pellet was resuspended in 10 mL of the same culture medium.

5.1.3 Cell lines

Line	**Description**	**Reference**
bEnd.3	Immortalised mouse brain Endothelial cells	(Montesano et al., 1990)
hCMEC/D3	Human Cortical Microvessels Endothelial Cells /D3	(Weksler et al., 2005)
hBVPs	Human Brain Vascular Pericytes	ScienCell
NHA	Human Astrocytes	Lonza
GL261	Murine glioma cells	(Szatmári et al., 2006)

bEnd.3 immortalised murine brain endothelial cell line was purchased from the American Type Culture Collection (ATCC® RL2299™). These cells were routinely grown in Dulbecco's Modified Eagle Medium (DMEM - Gibco) supplemented with 10% Fetal Bovine Serum (FBS), (100 U/mL-100 µg/L), and 1% Glutamine (200 mM). These cells have a doubling time of 26-30 hours and form a compact monolayer at confluency due to the presence of tight junctions.

hCMEC/D3 Human Cortical Microvessels Endothelial Cells, **hBVPs** Human Brain Vascular Pericytes, and **NHA** Human Astrocytes cell lines were cultured in EGM-2 Endothelial medium bullet kit (Lonza).

GL261 murine glioma cell line was cultured in DMEM and supplemented with 10% FBS, sodium pyruvate (Sigma Aldrich, 100 µM), 1% Penicillin-Streptomycin and 1% Glutamine. All cell lines were cultured in an incubator at 37 °C with 5% CO2 and 90% humidity.

5.2 Molecular cloning

Engineered plasmid	Description	Resistance	Reference
Pk8001	plasmid for phage display on modified gene VIII	Amp	MBT Lab
Pk8001_Tfm	Derivative of Pk8001 with Tfmimic peptide fused to the NTer of the pVIII protein	Amp	this work
Pk8001_GYR	Derivative of Pk8001 with GYR peptide fused to the NTer of the pVIII protein	Amp	this work
Pk8001_C7	Derivative of Pk8001 with C7 peptide fused to the NTer of the pVIII protein	Amp	this work
M13K07 Δori ΔpIII_Tfm	Derivative of M13K07 Hyperphage with Tfmimic peptide fused to the NTer of the pVIII protein	Km	this work
pComb_3XSS	plasmid for phage display on modified gene III	Amp	Addgene
pComb_Nbα	Derivative of pComb3XSS with nanobody anti-ALFA Tag fused to the N-Ter of the pIII protein	Amp	this work
pComb_LNbα_RTfm	Derivative of pComb3XSS with nanobody anti-ALFA Tag fused to the N-Ter of the pIII protein and the Tfm peptide fused to the C-Ter of the pVIII	Amp	this work
pComb_RNbα_LTfm	Derivative of pComb3XSS with nanobody anti-ALFA Tag fused to the N-Ter of the pIII protein and controlled by the Rhamnose promoter; and the Tfm peptide fused to the N-Ter of the pVIII protein and controlled by the Lac promoter	Amp	this work
ALFATag_hCD4_mOrange	Derivative of hCD4_mOrange plasmid with ALFA Tag and mOrange in frame with human CD4 gene	Amp	this work

Oligonucleotide	**Sequence 5’ → 3’**
AD269_Tfmimic_NcoI_fwd	CATGGCCTGCCGCACCATTGGCCCGAGCGTGTGCGGTGGCGGTG
AD270_Tfmimic_BamHI_rev	GATCCACCGCCACCGCACACGCTCGGGCCAATGGTGCGGCAGGC
AD460_GYR_NcoI_ fwd	CATGGCCGGTTATCGTCCGGTTCATAATATTCGTGGTCATTGGGCACCGGGT
AD461_GYR_BamHI_ rev	GATCCACCCGGTGCCCAATGACCACGAATATTATGAACCGGACGATAACCGG
AD462_C7BBB_NcoI_ fwd	CATGGCCTGTACCAGCACCAGCGCACCGTATTGT
AD463_C7BBB_BamHI_ rev	GATCCACAATACGGTGCGCTGGTGCTGGTACAGG
AD338_Nb_ALFA_fwd	GTTTTGAGCTCGAAGTGCAGCTTCAG
AD339_Nb_ALFA_rev	GTTTTACTAGTTGACGACACAGTGACC
AD302_CD4_ALFAtag_fwd	GAGCTCAGAAGAAGACTGACCGAACCCAAAGTGGTGCTGGGCAAAAAAG
AD303_CD4_ALFAtag_rev	CTCTTCGAGACGGCTCCCGCCGCTGGGCTTTCCCTGAGTGGCTG
AD519_Hyper_Tfm_NcoI_fwd	GCCCGAGCGTGTGCGGATCCGCTGAGGGTGACGATCCC
AD520_Hyper_Tfm_BamHI_fwd	CAATGGTGCGGCAGGCCATGGAGCGAAAGACAGCATCGG
AD497_pRham_NotI fwd	TTTTGCGGCCGCCCACAATTCAGCAAATTGTGAAC
AD498_pRham rev	TTTCATATGTAATTTCTCCTCTTTG
AD499_pk8001_Tfm fwd	AAAGAGGAGAAATTACATATGAAATACCTATTG
AD500_pk8001_Tfm_NotI rev	GTTTTGCGGCCGCCAAATAAAACGAAAGGCTCA
AD501_pComb3XSS_mut1 fwd	CGGCGCATACCCGTACGA
AD339_Nbα_rev	GTTTTACTAGTTGACGACACAGTGACC
AD502_pComb_Nbα_mut2_fwd	ATGGGCTCCAAAAAGATTTGG
AD503_pComb_Nbα_mut2 rev	AATTAATTTCTCCTCTTTGAATTCAATTG
AD504_pVIII_XhoI_mut_fwd	AGAGCTGTCTAGGGCGGCGG
AD505_pVIII_XhoI_mut_rev	GAGTCATTAGCTTGCTTTCGAGGTG

5.2.1 Pk8001_Blood Brain Barrier interacting peptides

The **pK8001_Tfm**, **pK8001_GYR**, and **pK8001_C7** phagemids were generated from the custom pK8001 vector (MBT Lab), designed for 8+8 phage display by encoding the N-terminal domain of the M13 pVIII major coat protein. Peptides interacting with BBB were cloned using NcoI and BamHI sites at the C-terminus of pVIII. Each sequence was synthesised as complementary oligonucleotides flanked by these sites (C- and N-term, respectively), phosphorylated with T4 Polynucleotide Kinase (New England Biolabs - NEB), and annealed in EDTA/NaOH. The pK8001 vector was digested with NcoI/BamHI, dephosphorylated (Quick CIP, NEB), and ligated with peptide inserts (1:5 vector:insert) overnight at 16 °C. Constructs were transformed into *E. coli* TG1 and, with the M13K07 Δori ΔpIII hyper plasmid, by heat shock. Transformants were plated on LBA with 2% glucose and 100 µg/mL ampicilli.

Colonies resistant to ampicillin, indicating successful uptake of the phagemid, expressed one of the peptides, Tfm, M1, GYR, or C7, in-frame with the C-terminal domain of the pVIII major coat protein. Cloning success was confirmed via Sanger sequencing (Mix2Seq kit, Eurofins) of the relevant phagemid region.

Only the cloning of Tfm, GYR, and C7BBB peptides was successful, whereas the M1 peptide appeared to be toxic to E. coli and was therefore not produced.

5.2.2 pComb_NanobodyALFA

The pComb_NanobodyALFA (pComb_Nbα) phagemid was produced by amplifying and cloning the coding region for the anti-ALFA tag nanobody from the pET51b(+)_EGFP_Nbα (Addgene plasmid #136626;(Götzke et al., 2019))) into the pComb3XSS_DsbA phagemid, digested with SacI/SpeI restriction enzymes (NEB) and linearised. The resulting plasmid pComb_Nbα was used to transform *E. coli* DH5α cells that were plated on LBA plates supplemented with 2% glucose and 100 µg/mL Amp. Positive clones were verified by Sanger sequencing (Mix2Seq kit, Eurofins).

5.2.3 ALFA_hCD4_mOrange

The molecular cloning of the ALFA-Tag hCD4_mOrange synthetic target was obtained through a mutagenic PCR. hCD4_mOrange (Addgene plasmid # 110192;) was used as template together with phosphorylated primers AD0302 and AD0303 in a PCR reaction using Q5 high

fidelity DNA polymerase (NEB). Amplicons were then ligated and transformed into rubidium chloride competent E. coli DH5α cells and plated on LBA plates supplemented with 2% glucose and 100 µg/mL Amp. Positive clones were verified by Sanger sequencing (Mix2Seq kit, Eurofins).

5.2.4 Orthogonal phages

The **M13K07 Δori ΔpIII_Tfm** orthogonal phage was derived from our previously engineered M13K07 Δori ΔpIII hyper phagemid (Petrosino et al., 2023). In this phagemid, the peptide Tf mimic was genetically fused to the wild-type gene encoding the pVIII major coat protein, allowing each expressed pVIII protein to display the peptide on the phage coat.

The coding sequence of Tf mimic peptide was cloned in frame with the pVIII major coat protein using mutagenic PCR, performed by Q5 high-fidelity DNA polymerase (NEB). Amplification was primed by phosphorylated oligos AD519 and AD520. Transformation and verification of successful cloning were carried out as described in Section 4.2.1.

To generate fully assembled and functional phage particles, *E. coli* DH5α cells were co-transformed with the M13K07 Δori ΔpIII_Tfm phagemid, which encodes all phage proteins except the minor coat protein pIII, and pComb_Nbα phagemid, which provides the pIII protein fused in-frame with an anti-ALFA Tag nanobody (Nbα). As a result, each of the approximately 2700 copies of the pVIII protein distributed along the phage capsid displays the Tfm peptide, while the five pIII proteins located at the tip of the phage display the Nbα.

The **pComb_LNbα_RTfm** and **pComb_RNbα_LTfm** phagemids are both derivatives of the original pComb_Nbα construct. The parental phagemid encodes the Nbα nanobody fused in-frame with the pIII minor coat protein, under the control of the inducible Lac promoter (pLac). Through molecular cloning, our aim was to generate cis-monocistronic phagemids encoding both modified pIII and pVIII proteins, each regulated by a distinct inducible promoter. Specifically, pComb_LNbα_RTfm places pIII-Nbα under the control of pLac and the pVIII-Tfm under the control of the rhamnose-inducible promoter (pRham), while in pComb_RNbα_LTfm, the promoter arrangement is inverted with pIII-Nbα by pRham and pVIII-Tfm regulated by pLac. To generate the pRham_pVIII_Tfm cistron, a double joint PCR protocol (DJ PCR) (Yu et al., 2004) was employed, consisting of three sequential PCR steps. In the first round, the two DNA fragments of interest were independently amplified, with the design of primers allowing for

the incorporation of 25-nucleotides overlapping regions to facilitate later fusion. Specifically, the rhamnose-inducible promoter was amplified from the ppk3015 phagemid (Doulix) using oligos AD497 and AD498. The forward primer introduced a NotI restriction site at the 5' end of the amplicon, while the reverse primer included a 25-nucleotide sequence homologous to the 5' end of the second fragment. At the same time, the pVIII-Tfm coding sequence was amplified from the pk8001 phagemid using oligos AD499 and AD500. The forward primer was designed to include a 25-nucleotide sequence at the 5' end, complementary to the 3' region of the pRham promoter fragment, and via the reverse primer a NotI restriction site was introduced at the 3' end of the amplicon.

The second round of PCR involved the fusion of these two DNA fragments, without further primers. Instead, equimolar amounts of the two previously amplified fragments were combined in a single PCR tube. The overlapping tail sequences allow the fragments to anneal and extend during cycling, resulting in a fused construct.

In the third and final PCR step, the full-length fusion product was amplified using phosphorylated primers AD497 and AD500, and the correct product size was confirmed via agarose gel electrophoresis.

To generate the cis-monocistronic pComb_LNbα_RTfm phagemids, two additional mutations were introduced into the original pComb_Nbα backbone. Specifically, two internal NcoI restriction sites were removed via two independent mutagenic PCRs using oligo pairs AD501 - AD339 and AD502 - AD503, respectively. Both the mutated pComb_Nbα backbone and the fused DJ-PCR product were digested O.N. at 37 °C with NotI, followed by gel extraction purification for the plasmid and PCR cleanup (Macherey-Nagel) for the insert. The plasmid backbone was then dephosphorylated, and the insert and vector were ligated at a 1:5 molar ratio (controllare) at 16 °C O.N. A residual SpeI restriction site was subsequently removed from the pComb_LNbα_RTfm phagemid through another mutagenic PCR using oligos AD504 and AD505. The final construct was verified by Sanger sequencing and transformed into E. coli DH5α cells following the protocol previously described.

The cis-monocistronic phagemid pComb_RNbα_LTfm phagemid was obtained by extracting the NbapIII-pVIIITfm coding sequence from the pComb_LNbα_RTfm construct and ligating it in reverse orientation into the original phagemid backbone. The pComb_RNbα_LTfm

phagemid was digested with EcoRI restriction enzyme which resulted to be a double cutter inside the original phagemid. Specifically, EcoRI cleaves downstream of the pLac promoter and upstream the pRham promoter, generating two fragments of 1505 bp and 4255 bp, respectively. These fragments were purified via gel extraxtion. The shorter insert was phosphorilated at its 5' ends using the T4 Polynucleotide Kinase (T4 PNK - Neb), while the longer fragment was dephosphorylated using calf intestinal alkaline phosphatase (Quick CIP – Neb) to prevent cis-ligation of the vector. The two DNA fragments were then mixed at a 1:5 vestor to insert molar ratio and ligated at 16 °C O.N. The final construct was verified by Sanger sequencing and transformed into E. coli DH5α cells following previously established protocol.

Additionally, to generate functional phage particles, either the pComb_LNbα_RTfm or pComb_RNbα_LTfm construct was co-transformed with the M13K07 Δori ΔpIII helper plasmid into E. coli DH5α cells. This setup enables the expression of all necessary components required for phage assembly, with the pIII-Nbα and pVIII-Tfm fusion proteins each under the control of distinct, inducible promoters.

5.3 Phage production

Phage production was carried out according to the protocols in the "Phage display: a laboratory manual" (G. J. Barbas, 2001) book. Two different production techniques were used: super-infection and co-transformation.

5.3.1 Nanobody ALFA

The Nanobody ALFA (Nbα) phage was produced using the **co-transformation** method. For this protocol, *E. coli* DH5α cells were concurrently transformed with two plasmids: the pComb_Nbα, encoding the pIII_Nbα fusion protein, and the M13K07_Δori hyper phagemid, which supplies all the required phage proteins necessary for the assembly of fully functional phage particles except for the WT pIII. Following transformation, a single positive colony was inoculated into 5 mL of LB medium supplemented with 100 µg/mL Amp and 0.4 mM isopropyl-β-D-1-thiogalactopyranoside (IPTG), to induce the expression of pIII-Nbα gene and grown at 30 °C for 24 hours under shaking conditions.

Following the incubation, phages were purified using a modified version of the protocol described by Passaretti et al. (Passaretti et al., 2020). Briefly, the bacterial culture was

centrifuged at 10000 × g at 4 °C for 20 minutes to pellet the E. coli cells, allowing recovery of phages from the supernatant. To this, (4% w/v) PEG-8000 and (3% w/v) NaCl were added. The mixture was incubated at 37 °C to dissolve the powders, followed by incubation at 4 °C for 1 hour to promote phage precipitation. The solution was then centrifuged again at 10000 × g, 4 °C for 20 minutes, and the resulting phage pellet was resuspended in 1× PBS. To remove residual PEG, an isoelectric point (IP) precipitation was performed: the pH of the suspension was slowly adjusted to pH 4.2, the IP of the M13 phage, by the dropwise addition of 0.5 M HCl, followed by centrifugation at 10000 × g at 4 °C for 30 minutes. The pellet was then resuspended in 1× PBS and further centrifuged at 6000 × g for 10 minutes to remove any remaining bacterial debris. The final phage-containing supernatant was collected, and the concentration of the phages was determined by measuring the absorbance at a wavelength of 269 nm using a UV-Vis spectrophotometer, with a known extinction coefficient of ε = 3.84 µM. After the assessment of the concentration, of 0.1% sodium azide (NaN_3 0.1%) was added as an antibacterial agent and the solution was stored at 4 °C.

5.3.2 BBB-interacting phages

The phages displaying the peptides **Tfm**, **GYR**, and **C7**, hereafter collectively referred to as BBB-interacting phages, were produced using both super-infection and co-transformation methods.

For the **super-infection** protocol, *E. coli* TG1 cells were first transformed with pk8001_BBB-interacting phagemids, which encode the pVIII major coat protein fused to the respective peptide of interest. To provide the remaining phage components, including a wild-type copy of pVIII, the transformed cells were subsequently infected with a wild-type M13K07 helper phage.

A single positive colony was inoculated into 5 mL of LB medium supplemented with 100 µg/mL Amp and 0.4 mM IPTG, to induce the expression of pVIII-BBB interacting peptide gene and grown at 37 °C under shaking conditions until reaching an optical density at 600 nm (OD600) of 0.4. At this point, 8 mL of fresh LB, supplemented with Amp (100 µg/mL) and 2 µL of M13K07 helper phage (1×10^{11} pfu/mL; NEB), was added to allow the infection. After 2 hours at 37 °C under shaking, the culture was scaled up to a total volume of 400 mL, with Amp

(100 µg/mL), Km (25 µg/mL) and 0.4 mM IPTG, and incubated at 30 °C for 24 hours with agitation.

For the **co-transformation** protocol, E. coli DH5α cells were simultaneously transformed the pk8001_BBB-interacting phagemid, encoding the pVIII-peptide fusion protein, and the M13K07 Δori hyper phagemid. Following transformation, a single positive colony was picked and inoculated into 400 mL of LB medium supplemented with 100 µg/mL Amp, 25 µg/mL Km and 0.4 mM IPTG and incubated at 30 °C for 24 hours under shaking conditions.

In both protocols phage purification was performed as described in the 5.3.1 section, including PEG/NaCl precipitation, IP adjustment, and multiple centrifugation steps to ensure removal of residual PEG and bacterial cells.

5.3.3 Orthogonal phages

The **Hyper_Tfm_Nbα** phage was obtained by co-transforming DH5α with M13K07 Δori ΔpIII_Tfm (expressing pVIII fused to the Tfm peptide) and pComb_Nbα (pIII fused to Nbα). This system yields phages displaying ~2700 copies of pVIII-Tfm along the capsid and 5 copies of pIII-Nbα at the tip. Similarly, **pComb_LNbα_RTfm** and **pComb_RNbα_LTfm** phages were generated by co-transforming DH5α cells with M13K07 Δori ΔpIII and the respective constructs. Colonies selected on LBA with Amp, Km, and 2% glucose were inoculated into 400 mL LB with Amp, Km, 4 mM IPTG, and either 5 mM or 10 mM rhamnose to modulate pRham-controlled expression, then cultured for 24 h at 30 °C with shaking. Purification was performed as for the other phages. These constructs incorporate two pVIII variants within the capsid: wild-type pVIII from the backbone and the pVIII-Tfm fusion.

5.4 Immunoblotting

Modified phages were validated and characterised using immunoblotting techniques, including Dot Blot and Western Blot assays.

5.4.1 Dot Blot

To confirm the presence of modified phage proteins, a dot blot assay was conducted. Phage samples were diluted to the desired concentrations, boiled for 10 minutes to denature proteins, and cooled to room temperature. Aliquots were then spotted onto a pre-activated, dried blotting membrane and allowed to pass through by gravity. The membrane was rinsed

with milliQ water, excess liquid removed under vacuum, and subsequently blocked for 45 minutes at room temperature in PBS containing 0.05% Tween-20 and 5% dry milk. Primary incubation was performed for 1 hour at RT using monoclonal anti-pIII (1:5000) or anti-pVIII (1:10000) antibodies (New England Biolabs) prepared in the same blocking solution. After multiple washes with PBS + 0.05% Tween-20, the membrane was incubated for 1 hour at RT with an HRP-conjugated anti-mouse IgG secondary antibody (Jackson Immuno Research; 1:10000). Following final washes, protein bands were visualized using an enhanced chemiluminescence (ECL) solution (Lightwave plus GVS filter technology), and signals were captured with a ChemiDoc™ Imaging System (Bio-Rad).

5.4.2 Western Blot

To verify that the molecular weight of the engineered fusion protein matched the predicted value and differed from the WT counterpart, a western blot assay was performed. Phage-containing solutions were mixed with loading buffer (2.5% β-mercaptoethanol, 1X SDS) and boiled for 10 minutes to denature proteins. Samples were then loaded onto a 15% (w/v) polyacrylamide gel and separated by SDS-PAGE under standard running conditions to achieve optimal resolution. Following electrophoresis, proteins were transferred onto a PVDF membrane (GVS) using a blotting chamber with transfer buffer (0.25X Tris-Glycine, 20% methanol). The membrane was subsequently blocked in PBS containing 0.05% Tween-20 and 5% dry milk for 45 minutes at room temperature before incubation with monoclonal anti-pIII (1:5000) or anti-pVIII (1:10000) antibodies (NEB) prepared in the same blocking solution, for 1 hour at RT. After thorough washes with PBS + 0.05% Tween-20, an HRP-conjugated anti-mouse IgG secondary antibody (Jackson Immuno Research; 1:10000) was applied for 1 hour at RT. Protein detection was achieved via enhanced chemiluminescence (Lightwave plus GVS filter technology), and the signal was recorded using the ChemiDoc™ Imaging System (Bio-Rad).

5.5 Differential ethidium bromide staining

The stability of BBB-interacting phages displaying Tfm, GYR, or C7 peptides was assessed by comparing intact virions with heat-denatured controls. For the experimental samples, phage suspensions were supplemented with SDS-free loading buffer. Control phage solutions, containing the same phage preparations as the test samples, were boiled at 98 °C for 15 min

before the addition of SDS-containing loading buffer. All samples were loaded onto a 0.8% (w/v) agarose gel prepared in 1×TAE buffer and subjected to electrophoresis at 80 V for 50 min. Following electrophoresis, gels were stained with ethidium bromide (EtBr, 1 µg/mL) for 10 min, washed twice with TAE, and imaged with a ChemiDoc imaging system (Bio-Rad). After initial imaging, gels underwent alkaline treatment to induce nucleic acid denaturation. Briefly, gels were washed twice with TAE, immersed in 50 mL of 0.4 M NaOH for 1 h, and then neutralized in 0.45 M HCl (pH 7) for 20 min. Following neutralization, the staining and washing steps were repeated as described above, and gels were reimaged with the ChemiDoc system to assess changes in nucleic acid integrity and migration patterns.

5.6 Phage conjugation

For Phage labelling, the fluorophore carboxylic group was covalently conjugated to the free amine-containing residues on the capsid of M13 via cross-coupling reaction using 1-ethyl-3-(3-dimethylaminopropyl) carbodiimide (EDC)/N-hydroxysuccinimide (NHS), resulting in the formation of amide bonds. First, the phage buffer was exchanged with a Zeba 40000 kDa column to replace PBS with HCO3-/CO32- buffer pH 8. The NHS-dye (10 mM) was then added to the phage suspension in a ratio of 1 µL dye for 200 µL phage (10^{14} virions/mL), and the reaction was carried out for 1 hour at room temperature under shaking. Excess free dye was removed by buffer exchange with two Zeba 40000 kDa columns, and conjugated phages were stored in PBS at 4 °C.

For Rose Bengal (RB) conjugation, performed by the NanoBioInterface lab of professor Matteo Calvaresi, NHS and EDC were added under stirring to a 10 mM RB solution in DMSO, adjusting to final concentrations of 15 mM NHS and 10 mM EDC. The reaction mixture was maintained under constant agitation (700 rpm) at 25 °C and protected from light for 3 hours. Subsequently, 50 µL of the activated RB solution were added dropwise to 1 mL of PBS containing 40 nM phages. The suspension was then incubated O.N. at 25 °C, in the dark, with continuous shaking at 700 rpm. Excess RB and other reaction byproducts were removed by dialysis against 100 mM sodium carbonate buffer (pH 9) using a 14 kDa cut-off regenerated cellulose membrane. A final dialysis step was performed against PBS.

5.7 BBB crossing essay

BBB crossing for transcytosis studies was performed by seeding bEnd.3 cells at a density of 90000 cells/mL onto a pre-coated with rat tail type I collagen solution (5155, Advanced BioMatrix) 12 mm Ø inserts and 3,0 µm pore size polyester membrane transwell (#665630, Greiner Bio-One International); the low-density paracellular transport controls were seeded at 10000 cell/mL. After three days of culture, **Trans Endothelial Electric Resistance (TEER)** measurements were performed using a computer-controlled multiwell device (CellZscope, nanoAnalytics GmbH, Münster, Germany) to monitor and confirm the formation of a tight 2D monolayer. The CellZscope system operates by applying an alternating current (AC) voltage through a pair of voltage-sensing electrodes positioned on either side of the Transwell insert, and by measuring the amplitude-phase response of the resulting current (Srinivasan et al., 2015). Tight junctions formed between adjacent cells restrict the paracellular flow of ions, thereby increasing the electrical resistance, which can be modeled by an equivalent circuit, omitting the contribution of the membrane resistance. TEER values higher than 10 Ω×cm2 (usually between 15 and 20 Ω×cm2 for bEND.3 cells) are indicative of the correct establishment of barrier-forming intercellular junctions, confirming the integrity of the 2D BBB model. When the TEER measurement reached the values range defined before, the transwells were moved to a 12 wells plate and cells were treated by replacing the apical fraction with 0.5 mL 5x1011 v/mL phages suspension in cDMEM. The basolateral fraction (BL) consisted of 1.5 mL of fresh cDMEM, from which 100 µL were withdrawn after 2, 24, 48, 72 hours from the phage treatment. The virions traslocated across the barrier were quantified through fluorescence quantification in a TECAN Spark microplate reader (TECAN, US), by interpolation from a calibration line. The phage virion number translocated across the low-density cell control transwell (without formed barrier) was considered the 100 % passage through the paracellular transport and used to normalize the phage transcellular crossing.

Phage uptake was verified through flow cytometer analysis. bEnd.3 cells were seeded 3 days prior to the experiment in 24-well plates at a cell density of 6×10^4 cells/mL (0.5 mL per well). Once confluent, cells were treated with $5x10^{11}$ v/mL CF594-labelled WT M13 phages for 24, 48 and 72 hours. Cells were then washed, harvested by trypsinisation, suspended in PBS and fixed in 2% paraformaldehyde (PFA). Cells were then run in flow cytometry employing a CytoFLEX S instrument (Beckman) equipped with 4 laser lines. For quantifying the internalisation rate, the

phage fluorescence was detected after excitation with a 561 nm laser through a 610/20 nm band pass filter. Single cells were gated based on physical parameters (FSC/SSC), and the results were expressed as fold increase in fluorescence intensity over the untreated control.

Immunofluorescence and confocal imaging were performed on fixed cells (4% PFA, 15 min). Cells were then permeabilised with 0.1% (v/v) Triton X-100, blocked with 2% (W7v) BSA, and incubated with primary antibodies for 1 hour at RT. The primary antibodies used were: rabbit monoclonal anti-zona occludens (ZO1; 1:200; #61-7300, ThermoFisher Scientific), rabbit polyclonal anti-claudin-5 (CLD5; 1:500; # PA599415, ThermoFisher Scientific), and rabbit monoclonal anti-tubulin β3 (1:500; #T2200, Sigma-Aldrich). After PBS washing, samples were incubated with the appropriate secondary antibody for 1 hour at RT. Cells were then incubated for 5 min with Hoechst (1 µM, #3342, Sigma) and were mounted with Vectashield antifade mounting medium (#H-1000-10, Vector Laboratories) on microscope slides. Image acquisitions were performed using a confocal microscope (Leica SP8 TCS, Leica Microsystems GmbH, Wetzlar, Germany) with a 63X (1.4 NA) oil immersion objective. Confocal images were acquired by using a 1024x1024 scan format at 400 Hz speed.

Phage recovery from basolateral fractions was achieved by concentration of the sample through ultracentrifugation at 100000×g for 3 h and purification via isoelectric precipitation (pH 4.2). Final purification was achieved with a second ultracentrifugation step before TEM grid preparation. For Western blot analysis, phages were precipitated with PEG 8000/NaCl and pelleted by centrifugation at 10000×g for 25 min, at 4 °C. **Western Blot** assay on BL fractions was performed as described in section 5.4.2.

Plaque assay to assess functional integrity of phages in the basolateral fractions was performed on *E. coli* TG01 cells. Cells at mid-log phase (OD_{600} ≈ 0.4) were infected with serially diluted phage suspensions, mixed with pre-warmed soft agar (0.7% w/v LB), and plated on LBA agar. Plates were incubated O.N. at 37 °C, and plaques were subsequently visualised and counted using a gel documentation system.

5.8 3D assembloid penetration

Three cell line BBB assembloids preparation was carried out using human brain vascular pericytes hBVPs (ScienCell), human astrocytes NHA (Lonza) and human endothelial cells hCMEC/D3 in a single well of a 96-well plate. Wells were coated with 1% agarose in PBS to

prevent cell attachment. Then, hBVPs and NHA were pre-labeled with CellTracker Green CMFDA Dye (Invitrogen, #C2925) for 1 h at 37 °C. The two cell lines and the hCMEC/D3 were then washed, collected and counted. Cells were seeded together at a cell density of 1500 cells per well in a 1:1:1 ratio, in 200 µL of the EGM-2 Endothelial medium bullet kit (Lonza), as previously described. Assembloids were incubated at 37 °C, 5% CO2, 95% humidity for 72 h prior to the treatment with 5E11 v/mL $M13_{WT}$ CF594 for 72 h.

For the **cryosectioning**, assembloids were collected in a 1.5 mL tube, washed and fixed in 4% PFA for 30 min at RT, washed and stored in PBS. They were then embedded in O.C.T. compound (Scigen Scientific Inc.) in a 1.5 mL tube and kept on dry ice until completely solidified. Next, the solid O.C.T. that had encapsulated the assembloid pellet on the tip was mounted onto a cryostat sample holder. Assembloids were sliced into 20 µm-thick slices and collected onto PLL/Gelatin-coated microscope glass slides and stored at -20 °C until further processing.

For **immunostaining and imaging** performed on 20 µm-thick assembloid slices, samples were washed 3 times to remove the O.C.T. and then permeabilised and blocked for 1 hour at RT with a 10% (w/v) BSA solution in 0.3% Triton-X100. After 3 washes, samples were incubated with anti ZO1 and anti-pVIII primary antibodies (5 µg/mL, #61-7300, Thermo Fisher Scientific and #61097 Progen respectively) in 2% (w/v) BSA solution in 0.1% Triton-X100 overnight at 4 °C. Secondary antibodies were incubated at RT for 1 hour in 2% (w/v) BSA solution in 0.1% Triton-X100, together with Hoechst. Slices were then imaged with a Leica SP8 confocal microscope equipped with 63x oil immersion objective and images were analysed with Cellprofiler image analysis software.

5.9 2D Targeting assessment

5.9.1 Neuronal targeting

Cortical neurons were obtained from mouse **dissection** (E17, E18) and plated at a density of 40000 cells/well on PLL-coated 18 mm-diameter glass coverslips, and cultured in 2 mL of complete Neurobasal medium, containing 2% B27, 1% Penicillin/Streptavidin and 1% Glutamine.

Primary neuron transfection was carried out at Day In Vitro 7(DIV7), by treating the neurons with 1 µg/well of the ALFATag_hCD4_mOrange DNA plasmid and 2.5 µg/well of Lipofectamine

2000 (Invitrogen) in plain Neurobasal medium. Neurons were incubated at 37 °C for 30 min, in the mixture, washed twice and kept for at least 48 hours in their conditioned medium prior to further experiments.

Primary neuron phage targeting experiments were performed on ALFATag_hCD4_mOrange expressing cortical neurons. Briefly, the $M13_{Nb\alpha}$ phage solution was diluted to 5 x 10^{11} v/mL in the neurons conditioned medium, incubated for 1 hour at 37 °C. Neurons were fixed in 4 % PFA and imaged with a Leica SP8 confocal microscope equipped with a 63x oil immersion objective. The images were analyzed with the CellProfiler image analysis software.

5.10 GL261 hEGFR-vIII$^+$ cell line generation

5.10.1 Cell transfection

Murine glioma GL261 cells were genetically engineered to stably express the human Epidermal Growth Factor Receptor Variant III (hEGFR - vIII) using non-viral transfection methods. The plasmid carrying the hEGFRvIII sequence also contained a Geneticin (G418) resistance cassette to enable positive selection of transfected clones.

For transfection, GL261 cells were seeded at a density of 5×10^4 cells per well in 96-well plates one day prior to transfection. Two non-viral transfection reagents were evaluated: Lipofectamine™ 2000 (Invitrogen) and FuGENE® 6 (Promega). A constant amount of 800 ng of plasmid DNA was used per well, and different DNA:reagent ratios were optimized according to the manufacturer's guidelines. Specifically, ratios of 1:2 and 1:2.5 (w/v) were tested for Lipofectamine 2000, while 1:3 and 1:5 ratios were tested for FuGENE 6.

For both transfections, plasmid DNA and the transfection reagent were mixed in serum-free DMEM and incubated for 20 min at room temperature to allow complex formation. The resulting mixture was then added to the cells in complete medium and incubated for 48 h under standard culture conditions (37 °C, 5% CO_2). In both cases, control samples included one with plasmid DNA only and another containing the transfection reagent mixed with an unrelated construct (hCD4_mOrange_AlfaTag). After 48 h, cells were detached and reseeded by limiting dilution (12 cells per well) in the presence of Geneticin (Promega; stock 50 mg/mL, used at 0.4 mg/mL final concentration) to apply continuous selective pressure. The cells were subsequently cultured for a period of three weeks under continuous selective pressure to

ensure the robust establishment of stable expressors. During this time, the population was routinely detached and progressively scaled up by transferring them to larger culture supports to allow the expansion of the genetically engineered GL261-hEGFR-vIII+ cell line

Although clonal isolation ideally requires single-cell seeding to obtain stably transfected clones, the GL261 line exhibited poor viability at densities below 12 cells per well, making standard single-cell cloning unfeasible. The resulting polyclonal population was therefore maintained under Geneticin selection to promote plasmid integration and stable expression of hEGFRvIII.

5.10.2 Sorting

To enrich for stably hEGFR-vIII expressing cells, Fluorescence-Activated Cell Sorting (FACS) was performed. Only GL261 cells transfected with FuGENE® showed stable expression of hEGFR - vIII under continuous antibiotic selection. They were harvested and stained with a specific antibody against the human EGFRvIII receptor. For quality control and gating, four control conditions were included in parallel:

- Non-transfected GL261 cells stained with the primary antibody only.
- Non-transfected GL261 cells stained with the secondary antibody only.
- Transfected GL261 cells stained with the secondary antibody only (background fluorescence control).
- Unstained transfected GL261 cells (autofluorescence control).

A total of 2×10^7 transfected cells were detached and centrifuged. The pellet was resuspended in PBS containing the primary antibody, a rabbit monoclonal anti-hEGFRvIII (Cell Signaling Technology, #64952), at a 1:1000 dilution, and incubated for 30 min at RT under agitation. After two PBS washes, cells were incubated with a fluorophore-labeled secondary antibody (Goat anti-Rabbit IgG Alexa Fluor™ 488, Invitrogen) at a 1:1000 dilution for 30 min at RT in the dark, followed by two additional PBS washes. The final pellet was resuspended in PBS supplemented with 2% Penicillin-Streptomycin.

Before sorting, the suspension was passed through a 35 µm nylon filter (Corning Falcon® 5 mL Round Bottom Polystyrene Test Tube with Cell Strainer Snap Cap) to remove aggregates and ensure a single-cell suspension. The sorting was conducted on a FACSAriaIII cytometer

(R656700G50003) using FACSDiva Version 9.4 software. A 70 micron precision nozzle was employed for a 4-Way Purity sort. The sorting ran for an elapsed time of 25 minutes and 47 seconds. During this time, 5201945 threshold events were counted, and 330785 positive events were collected with an efficiency of 100%. Collection tube contained 7 mL of complete DMEM supplemented with 2% Penicillin-Streptomycin to maintain post-sorting cell viability.

The sorted cells, which were cultured under standard conditions (37 °C, 5% CO_2) in supplemented DMEM containing 2% Penicillin-Streptomycin and Geneticin (G418, 1:125 dilution) to preserve selection pressure.

5.10.3 Targeting

Following expansion, the sorted GL261-hEGFRvIII$^+$ cells were subjected to a targeting assessment to confirm the specific binding affinity of the $M13_{7D12}$ nanovector for the expressed receptor.

Sorted cells were seeded at a density of 9×10^4 cells per well in a 24-well plate the day prior to the experiment. The next day, cells were incubated with the $M13_{7D12}$ phage solution for 90 minutes. Control conditions included non-transfected GL261 cells treated with the $M13_{7D12}$ phage and transfected GL261-hEGFRvIII+ cells treated with the $M13_{WT}$ phage.

After incubation, cells were fixed using a 4%PFA solution for 15 minutes under stirring conditions. Cells were subsequently blocked for 45 minutes at room temperature in PBS containing 0.05% Tween-20 and 5% BSA. Following blocking, the cells were incubated for 1 hour with a monoclonal anti-pVIII antibody (New England Biolabs – NEB) at a dilution of 1:500, prepared in the same blocking solution. After the primary antibody incubation, cells were washed twice with PBS and incubated for 1 hour in the dark with the Alexa Fluor™ 488-labelled Goat anti-Mouse secondary antibody (Invitrogen, REF A32766TR). Finally, the cells were resuspended in PBS containing Sytox Blue (Invitrogen™ Catalog number S34857), a viability dye that binds to the DNA of permeabilised cells at a final concentration of 3 µM.

Samples were analysed using a 90.78.120.043 BD FORTESSA **Flow Cytometer**, and the resulting data were analysed using FlowJo V10 software (Tree Star, Inc.).

For **immunofluorescence** analysis, transfected GL261 cells were seeded on round glass coverslips (22 mm diameter) and treated under the same staining conditions described above.

During incubation with the secondary antibody, cells were simultaneously stained with Hoechst (1 µM) to label nuclei. After the final washes, coverslips were mounted on glass slides using Aquatex® mounting medium (Sigma-Aldrich, REF 1.08562). Fluorescence images were acquired using a Nikon Eclipse Ti2-E inverted microscope and processed with Imagej Fiji.

5.11 Photodynamic Therapy (PDT)

To assess the PDT efficacy of the $M13_{7D12}$ – RB platform on hEGFR-vIII-expressing cells and to evaluate the modality of cell death induced by treatment, a series of experiments were performed on both unsorted and FACS-sorted GL261-hEGFRvIII$^+$ populations.

For all PDT experiments, cells were **seeded** at a density of 8×10^4 cells per well in 96-well plates 24 h before treatment. Non-transfected untreated GL261 cells and transfected cells treated with $M13_{WT}$ phage were used as negative and specificity controls, respectively.

After 24 h, cells were **incubated** with different concentrations (0, 0.3, and 1 µM) of the $M13_{7D12}$–RB platform according to the experimental design. Incubation times tested were 1 and 24 h. Following incubation, cells were washed with PBS and irradiated using a Thorlabs M565L3 mounted LED (λ = 565 nm, 880 mW, 1000 mA). The **irradiation** duration was set to either 1 or 2 minutes depending on the experiment.

After irradiation, cells were incubated in cDMEM under standard conditions (37 °C, 5% CO_2) for a 24-hour recovery period.

The **cytotoxic effect** of the platform was assessed using either the **MTS assay** or flow cytometry–based viability analysis. For the MTS assay, treated and recovered cells were incubated with the CellTiter 96® AQueous Non-Radioactive Cell Proliferation Assay (MTS, Promega) according to the manufacturer's instructions. After a 2-hour incubation period at 37 °C, absorbance was measured using a TECAN microplate reader to quantify cell metabolic activity as an indicator of cell viability.

For the **flow cytometry viability assay**, after treatment and a 24-hour recovery period, cells were detached, centrifuged, and resuspended in PBS containing 1 µM Sytox Blue viability dye (Thermo Fisher Scientific). Samples were analyzed using a BD FORTESSA Flow Cytometer (BD Biosciences), and data were processed with FlowJo v10 software. The fluorescence intensity

of Sytox Blue was used to quantify the proportion of non-viable cells, as the dye selectively penetrates and binds to the DNA of cells with compromised membrane integrity.

The **Annexin V assay** was performed to determine the modality of cell death. After treatment and a 24-hour recovery period, cells were resuspended in 1X Annexin V binding buffer, prepared by diluting the 10X stock solution (0.1 M HEPES, pH 7.4; 1.4 M NaCl; 25 mM $CaCl_2$) 1:10 with distilled water. To each sample, 4 µL of Annexin V FITC (Life Technologies, V13242/2024) and Sytox Blue (final concentration 1 µM) were added. Control samples included:

- Cells resuspended in buffer only (unstained control).
- Cells stained with Sytox Blue only.
- Cells stained with Annexin V only.

Cells were analyzed using a BD FORTESSA Flow Cytometer (BD Biosciences), and the resulting data were processed with FlowJo v10 software (Tree Star, Inc.). Fluorescence signals were used to distinguish early apoptotic (Annexin V^+/Sytox $Blue^-$), late apoptotic (Annexin V^+/Sytox $Blue^+$), and necrotic (Annexin V^-/Sytox $Blue^+$) cells.

References

Abbott, N. J. (2013). Blood–brain barrier structure and function and the challenges for CNS drug delivery. *Journal of Inherited Metabolic Disease*, *36*(3), 437–449. https://doi.org/10.1007/s10545-013-9608-0

Achar, A., Myers, R., & Ghosh, C. (2021). Drug Delivery Challenges in Brain Disorders across the Blood–Brain Barrier: Novel Methods and Future Considerations for Improved Therapy. *Biomedicines*, *9*(12), 1834. https://doi.org/10.3390/biomedicines9121834

Alessandrini, F., Menotti, L., Avitabile, E., Appolloni, I., Ceresa, D., Marubbi, D., Campadelli-Fiume, G., & Malatesta, P. (2019). Eradication of glioblastoma by immuno-virotherapy with a retargeted oncolytic HSV in a preclinical model. *Oncogene*, *38*(23), 4467–4479. https://doi.org/10.1038/s41388-019-0737-2

Appolloni, I., Alessandrini, F., Menotti, L., Avitabile, E., Marubbi, D., Piga, N., Ceresa, D., Piaggio, F., Campadelli-Fiume, G., & Malatesta, P. (2021). Specificity, Safety, Efficacy of EGFRvIII-Retargeted Oncolytic HSV for Xenotransplanted Human Glioblastoma. *Viruses*, *13*(9), 1677. https://doi.org/10.3390/v13091677

Badawi, A. H., Mohamad, N. A., Stanslas, J., Kirby, B. P., Neela, V. K., Ramasamy, R., & Basri, H. (2024). In Vitro Blood-Brain Barrier Models for Neuroinfectious Diseases: A Narrative Review. *Current Neuropharmacology*, *22*(8), 1344–1373. https://doi.org/10.2174/1570159X22666231207114346

Barr, J. J. (2017). A bacteriophages journey through the human body. *Immunological Reviews*, *279*(1), 106–122. https://doi.org/10.1111/imr.12565

Bergmann, S., Lawler, S. E., Qu, Y., Fadzen, C. M., Wolfe, J. M., Regan, M. S., Pentelute, B. L., Agar, N. Y. R., & Cho, C.-F. (2018). Blood–brain-barrier organoids for investigating the permeability of CNS therapeutics. *Nature Protocols*, *13*(12), 2827–2843. https://doi.org/10.1038/s41596-018-0066-x

Bhatwa, A., Wang, W., Hassan, Y. I., Abraham, N., Li, X.-Z., & Zhou, T. (2021). Challenges Associated With the Formation of Recombinant Protein Inclusion Bodies in Escherichia coli and Strategies to Address Them for Industrial Applications. *Frontiers in Bioengineering and Biotechnology*, *9*, 630551. https://doi.org/10.3389/fbioe.2021.630551

Bichet, M. C., Chin, W. H., Richards, W., Lin, Y.-W., Avellaneda-Franco, L., Hernandez, C. A., Oddo, A., Chernyavskiy, O., Hilsenstein, V., Neild, A., Li, J., Voelcker, N. H., Patwa, R., & Barr, J. J. (2021). Bacteriophage uptake by mammalian cell layers represents a potential sink that may impact phage therapy. *iScience*, *24*(4), 102287. https://doi.org/10.1016/j.isci.2021.102287

Bichet, M. C., Patwa, R., & Barr, J. J. (2021). Protocols for studying bacteriophage interactions with in vitro epithelial cell layers. *STAR Protocols*, *2*(3), 100697. https://doi.org/10.1016/j.xpro.2021.100697

Blanco, E., Shen, H., & Ferrari, M. (2015). Principles of nanoparticle design for overcoming biological barriers to drug delivery. *Nature Biotechnology*, *33*(9), 941–951. https://doi.org/10.1038/nbt.3330

Bortot, B., Apollonio, M., Baj, G., Andolfi, L., Zupin, L., Crovella, S., Di Giosia, M., Cantelli, A., Saporetti, R., Ulfo, L., Petrosino, A., Di Lorenzo, G., Romano, F., Ricci, G., Mongiat, M., Danielli, A., Calvaresi, M., & Biffi, S. (2022). Advanced photodynamic therapy with an engineered M13 phage targeting EGFR: Mitochondrial localization and autophagy induction in ovarian cancer cell lines. *Free Radical Biology and Medicine*, *179*, 242–251. https://doi.org/10.1016/j.freeradbiomed.2021.11.019

Bratkovič, T. (2010). Progress in phage display: Evolution of the technique and its applications. *Cellular and Molecular Life Sciences*, *67*(5), 749–767. https://doi.org/10.1007/s00018-009-0192-2

Cader, Z., & Neuhaus, W. (Eds). (2022). *Physiology, Pharmacology and Pathology of the Blood-Brain Barrier* (Vol. 273). Springer International Publishing. https://doi.org/10.1007/978-3-030-99654-3

Castagnola, V., Deleye, L., Podestà, A., Jaho, E., Loiacono, F., Debellis, D., Trevisani, M., Ciobanu, D. Z., Armirotti, A., Pisani, F., Flahaut, E., Vazquez, E., Bramini, M., Cesca, F., & Benfenati, F. (2023). Interactions of Graphene Oxide and Few-Layer Graphene with the Blood–Brain Barrier. *Nano Letters*, *23*(7), 2981–2990. https://doi.org/10.1021/acs.nanolett.3c00377

Catanzaro, E., Feron, O., Skirtach, A. G., & Krysko, D. V. (2022). Immunogenic Cell Death and Role of Nanomaterials Serving as Therapeutic Vaccine for Personalized Cancer Immunotherapy. *Frontiers in Immunology*, *13*, 925290. https://doi.org/10.3389/fimmu.2022.925290

Chaitanya, K. V. (2019). Structure and Organization of Virus Genomes. In K. V. Chaitanya, *Genome and Genomics* (pp. 1–30). Springer Singapore. https://doi.org/10.1007/978-981-15-0702-1_1

Chang, C., Guo, W., Yu, X., Guo, C., Zhou, N., Guo, X., Huang, R.-L., Li, Q., & Zhu, Y. (2023). Engineered M13 phage as a novel therapeutic bionanomaterial for clinical applications: From tissue regeneration to cancer therapy. *Materials Today Bio*, *20*, 100612. https://doi.org/10.1016/j.mtbio.2023.100612

Chio, I. I. C., & Tuveson, D. A. (2017). ROS in Cancer: The Burning Question. *Trends in Molecular Medicine*, *23*(5), 411–429. https://doi.org/10.1016/j.molmed.2017.03.004

Correia, A. C., Monteiro, A. R., Silva, R., Moreira, J. N., Sousa Lobo, J. M., & Silva, A. C. (2022). Lipid nanoparticles strategies to modify pharmacokinetics of central nervous system targeting drugs: Crossing or circumventing the blood–brain barrier (BBB) to manage neurological disorders. *Advanced Drug Delivery Reviews*, *189*, 114485. https://doi.org/10.1016/j.addr.2022.114485

Cuggino, J. C., Blanco, E. R. O., Gugliotta, L. M., Alvarez Igarzabal, C. I., & Calderón, M. (2019). Crossing biological barriers with nanogels to improve drug delivery performance. *Journal of Controlled Release*, *307*, 221–246. https://doi.org/10.1016/j.jconrel.2019.06.005

De Sordi, L., Lourenço, M., & Debarbieux, L. (2019a). "I will survive": A tale of bacteriophage-bacteria coevolution in the gut. *Gut Microbes*, *10*(1), 92–99. https://doi.org/10.1080/19490976.2018.1474322

De Sordi, L., Lourenço, M., & Debarbieux, L. (2019b). The Battle Within: Interactions of Bacteriophages and Bacteria in the Gastrointestinal Tract. *Cell Host & Microbe*, *25*(2), 210–218. https://doi.org/10.1016/j.chom.2019.01.018

Dos Santos, A. F., De Almeida, D. R. Q., Terra, L. F., Baptista, M. S., & Labriola, L. (2019). Photodynamic therapy in cancer treatment—An update review. *Journal of Cancer Metastasis and Treatment*, *2019*. https://doi.org/10.20517/2394-4722.2018.83

Dubos, R. J., Straus, J. H., & Pierce, C. (1943). THE MULTIPLICATION OF BACTERIOPHAGE IN VIVO AND ITS PROTECTIVE EFFECT AGAINST AN EXPERIMENTAL INFECTION WITH SHIGELLA DYSENTERIAE. *Journal of Experimental Medicine*, *78*(3), 161–168. https://doi.org/10.1084/jem.78.3.161

Efimova, I., Catanzaro, E., Van Der Meeren, L., Turubanova, V. D., Hammad, H., Mishchenko, T. A., Vedunova, M. V., Fimognari, C., Bachert, C., Coppieters, F., Lefever, S., Skirtach, A. G., Krysko, O., & Krysko, D. V. (2020). Vaccination with early ferroptotic cancer cells induces efficient antitumor immunity. *Journal for ImmunoTherapy of Cancer*, *8*(2), e001369. https://doi.org/10.1136/jitc-2020-001369

Fadaie, M., Dianat-Moghadam, H., Ghafouri, E., Naderi, S., Darvishali, M. H., Ghovvati, M., Khanahmad, H., Boshtam, M., & Makvandi, P. (2023). Unraveling the potential of M13 phages in biomedicine: Advancing drug nanodelivery and gene therapy. *Environmental Research*, *238*, 117132. https://doi.org/10.1016/j.envres.2023.117132

G. J. Barbas, C. F. . I. B. D. R. . S. J. K. . S. (2001). *Phage Display: A Laboratory Manual*.

Gawarkar-Patil, P., Mahajan, B., Pawar, A., & Dhapte-Pawar, V. (2024). Cubosomes: Evolving platform for intranasal drug delivery of neurotherapeutics. *Future Journal of Pharmaceutical Sciences*, *10*(1), 91. https://doi.org/10.1186/s43094-024-00665-7

Ghosh, D., Kohli, A. G., Moser, F., Endy, D., & Belcher, A. M. (2012). Refactored M13 Bacteriophage as a Platform for Tumor Cell Imaging and Drug Delivery. *ACS Synthetic Biology*, *1*(12), 576–582. https://doi.org/10.1021/sb300052u

Ghosh, D., Lee, Y., Thomas, S., Kohli, A. G., Yun, D. S., Belcher, A. M., & Kelly, K. A. (2012). M13-templated magnetic nanoparticles for targeted in vivo imaging of prostate cancer. *Nature Nanotechnology*, *7*(10), 677–682. https://doi.org/10.1038/nnano.2012.146

Götzke, H., Kilisch, M., Martínez-Carranza, M., Sograte-Idrissi, S., Rajavel, A., Schlichthaerle, T., Engels, N., Jungmann, R., Stenmark, P., Opazo, F., & Frey, S. (2019). The ALFA-tag is a highly

versatile tool for nanobody-based bioscience applications. *Nature Communications*, *10*(1), 4403. https://doi.org/10.1038/s41467-019-12301-7

G.P. Smith, V. Petrenko. (1997). Phage Display. *Phage Display*, 391–410.

Hanahan, D. (1983). Studies on transformation of Escherichia coli with plasmids. *Journal of Molecular Biology*, *166*(4), 557–580. https://doi.org/10.1016/S0022-2836(83)80284-8

Harada, L. K. (2018). *Biotechnological applications of bacteriophages_ State of the art*.

Helms, H. C., Abbott, N. J., Burek, M., Cecchelli, R., Couraud, P.-O., Deli, M. A., Förster, C., Galla, H. J., Romero, I. A., Shusta, E. V., Stebbins, M. J., Vandenhaute, E., Weksler, B., & Brodin, B. (2016). In vitro models of the blood–brain barrier: An overview of commonly used brain endothelial cell culture models and guidelines for their use. *Journal of Cerebral Blood Flow & Metabolism*, *36*(5), 862–890. https://doi.org/10.1177/0271678X16630991

Henry, K. A., Arbabi-Ghahroudi, M., & Scott, J. K. (2015). Beyond phage display: Non-traditional applications of the filamentous bacteriophage as a vaccine carrier, therapeutic biologic, and bioconjugation scaffold. *Frontiers in Microbiology*, *6*. https://doi.org/10.3389/fmicb.2015.00755

Hess, G. T., Cragnolini, J. J., Popp, M. W., Allen, M. A., Dougan, S. K., Spooner, E., Ploegh, H. L., Belcher, A. M., & Guimaraes, C. P. (2012). M13 Bacteriophage Display Framework That Allows Sortase-Mediated Modification of Surface-Accessible Phage Proteins. *Bioconjugate Chemistry*, *23*(7), 1478–1487. https://doi.org/10.1021/bc300130z

Huh, H., Wong, S., St. Jean, J., & Slavcev, R. (2019). Bacteriophage interactions with mammalian tissue: Therapeutic applications. *Advanced Drug Delivery Reviews*, *145*, 4–17. https://doi.org/10.1016/j.addr.2019.01.003

Jiang, Y., Pan, X., Yu, T., & Wang, H. (2023). Intranasal administration nanosystems for brain-targeted drug delivery. *Nano Research*, *16*(12), 13077–13099. https://doi.org/10.1007/s12274-023-6026-y

Jiao, Y., Yang, L., Wang, R., Song, G., Fu, J., Wang, J., Gao, N., & Wang, H. (2024). Drug Delivery Across the Blood–Brain Barrier: A New Strategy for the Treatment of Neurological Diseases. *Pharmaceutics*, *16*(12), 1611. https://doi.org/10.3390/pharmaceutics16121611

Kan, L., & Barr, J. J. (2023). A Mammalian Cell's Guide on How to Process a Bacteriophage. *Annual Review of Virology*, *10*(1), 183–198. https://doi.org/10.1146/annurev-virology-111821-111322

Kepp, O., Senovilla, L., Vitale, I., Vacchelli, E., Adjemian, S., Agostinis, P., Apetoh, L., Aranda, F., Barnaba, V., Bloy, N., Bracci, L., Breckpot, K., Brough, D., Buqué, A., Castro, M. G., Cirone, M., Colombo, M. I., Cremer, I., Demaria, S., … Galluzzi, L. (2014). Consensus guidelines for the detection of immunogenic cell death. *OncoImmunology*, *3*(9), e955691. https://doi.org/10.4161/21624011.2014.955691

Koo, J., Lim, C., & Oh, K. T. (2024). Recent Advances in Intranasal Administration for Brain-Targeting Delivery: A Comprehensive Review of Lipid-Based Nanoparticles and Stimuli-

Responsive Gel Formulations. *International Journal of Nanomedicine*, *Volume 19*, 1767–1807. https://doi.org/10.2147/IJN.S439181

Krysko, D. V., Garg, A. D., Kaczmarek, A., Krysko, O., Agostinis, P., & Vandenabeele, P. (2012). Immunogenic cell death and DAMPs in cancer therapy. *Nature Reviews Cancer*, *12*(12), 860–875. https://doi.org/10.1038/nrc3380

Lee, K. H., Lee, J.-W., Song, J., & Hwang, M. (2013). Nanoscale bacteriophage biosensors beyond phage display. *International Journal of Nanomedicine*, 3917. https://doi.org/10.2147/ijn.s51894

Lee, S.-W., Mao, C., Flynn, C. E., & Belcher, A. M. (2002). Ordering of Quantum Dots Using Genetically Engineered Viruses. *Science*, *296*(5569), 892–895. https://doi.org/10.1126/science.1068054

Li, J., Zhang, Q., Pang, Z., Wang, Y., Liu, Q., Guo, L., & Jiang, X. (2012). Identification of peptide sequences that target to the brain using in vivo phage display. *Amino Acids*, *42*(6), 2373–2381. https://doi.org/10.1007/s00726-011-0979-y

Li, X., Vemireddy, V., Cai, Q., Xiong, H., Kang, P., Li, X., Giannotta, M., Hayenga, H. N., Pan, E., Sirsi, S. R., Mateo, C., Kleinfeld, D., Greene, C., Campbell, M., Dejana, E., Bachoo, R., & Qin, Z. (2021). Reversibly Modulating the Blood–Brain Barrier by Laser Stimulation of Molecular-Targeted Nanoparticles. *Nano Letters*, *21*(22), 9805–9815. https://doi.org/10.1021/acs.nanolett.1c02996

Loh, B., Gondil, V. S., Manohar, P., Khan, F. M., Yang, H., & Leptihn, S. (2021). Encapsulation and Delivery of Therapeutic Phages. *Applied and Environmental Microbiology*, *87*(5), e01979-20. https://doi.org/10.1128/AEM.01979-20

Lourenço, M., Chaffringeon, L., Lamy-Besnier, Q., Pédron, T., Campagne, P., Eberl, C., Bérard, M., Stecher, B., Debarbieux, L., & De Sordi, L. (2020). The Spatial Heterogeneity of the Gut Limits Predation and Fosters Coexistence of Bacteria and Bacteriophages. *Cell Host & Microbe*, *28*(3), 390-401.e5. https://doi.org/10.1016/j.chom.2020.06.002

Lourenço, M., De Sordi, L., & Debarbieux, L. (2018). The Diversity of Bacterial Lifestyles Hampers Bacteriophage Tenacity. *Viruses*, *10*(6), 327. https://doi.org/10.3390/v10060327

Luo, Q., Yang, J., Yang, M., Wang, Y., Liu, Y., Liu, J., Kalvakolanu, D. V., Cong, X., Zhang, J., Zhang, L., Guo, B., & Duo, Y. (2025). Utilization of nanotechnology to surmount the blood-brain barrier in disorders of the central nervous system. *Materials Today Bio*, *31*, 101457. https://doi.org/10.1016/j.mtbio.2025.101457

Madadi, A. K., & Sohn, M.-J. (2024). Advances in Intrathecal Nanoparticle Delivery: Targeting the Blood–Cerebrospinal Fluid Barrier for Enhanced CNS Drug Delivery. *Pharmaceuticals*, *17*(8), 1070. https://doi.org/10.3390/ph17081070

Mahringer, A., Puris, E., & Fricker, G. (2021). Crossing the blood-brain barrier: A review on drug delivery strategies using colloidal carrier systems. *Neurochemistry International*, *147*, 105017. https://doi.org/10.1016/j.neuint.2021.105017

Mai-Prochnow, A., Hui, J. G. K., Kjelleberg, S., Rakonjac, J., McDougald, D., & Rice, S. A. (2015). 'Big things in small packages: The genetics of filamentous phage and effects on fitness of their host'. *FEMS Microbiology Reviews*, *39*(4), 465–487. https://doi.org/10.1093/femsre/fuu007

Maya-Vetencourt, J. F., Manfredi, G., Mete, M., Colombo, E., Bramini, M., Di Marco, S., Shmal, D., Mantero, G., Dipalo, M., Rocchi, A., DiFrancesco, M. L., Papaleo, E. D., Russo, A., Barsotti, J., Eleftheriou, C., Di Maria, F., Cossu, V., Piazza, F., Emionite, L., … Benfenati, F. (2020). Subretinally injected semiconducting polymer nanoparticles rescue vision in a rat model of retinal dystrophy. *Nature Nanotechnology*, *15*(8), 698–708. https://doi.org/10.1038/s41565-020-0696-3

Montegiove, N., Calzoni, E., Emiliani, C., & Cesaretti, A. (2022). Biopolymer Nanoparticles for Nose-to-Brain Drug Delivery: A New Promising Approach for the Treatment of Neurological Diseases. *Journal of Functional Biomaterials*, *13*(3), 125. https://doi.org/10.3390/jfb13030125

Montesano, R., Pepper, M. S., Möhle-Steinlein, U., Risau, W., Wagner, E. F., & Orci, L. (1990). Increased proteolytic activity is responsible for the aberrant morphogenetic behavior of endothelial cells expressing the middle T oncogene. *Cell*, *62*(3), 435–445. https://doi.org/10.1016/0092-8674(90)90009-4

Nguyen, S., Baker, K., Padman, B. S., Patwa, R., Dunstan, R. A., Weston, T. A., Schlosser, K., Bailey, B., Lithgow, T., Lazarou, M., Luque, A., Rohwer, F., Blumberg, R. S., & Barr, J. J. (2017). Bacteriophage Transcytosis Provides a Mechanism To Cross Epithelial Cell Layers. *mBio*, *8*(6), e01874-17. https://doi.org/10.1128/mBio.01874-17

Niazi, S. K. (2023). Non-Invasive Drug Delivery across the Blood–Brain Barrier: A Prospective Analysis. *Pharmaceutics*, *15*(11), 2599. https://doi.org/10.3390/pharmaceutics15112599

Pagani, F., Orzan, F., Lago, S., De Bacco, F., Prelli, M., Cominelli, M., Somenza, E., Gryzik, M., Balzarini, P., Ceresa, D., Marubbi, D., Isella, C., Crisafulli, G., Poli, M., Malatesta, P., Galli, R., Ronca, R., Zippo, A., Boccaccio, C., & Poliani, P. L. (2025). Concurrent RB1 and P53 pathway disruption predisposes to the development of a primitive neuronal component in high-grade gliomas depending on MYC-driven EBF3 transcription. *Acta Neuropathologica*, *149*(1), 8. https://doi.org/10.1007/s00401-025-02845-y

Pardridge, W. M. (2012). Drug Transport across the Blood–Brain Barrier. *Journal of Cerebral Blood Flow & Metabolism*, *32*(11), 1959–1972. https://doi.org/10.1038/jcbfm.2012.126

Passaretti, P., Khan, I., Dafforn, T. R., & Goldberg Oppenheimer, P. (2020). Improvements in the production of purified M13 bacteriophage bio-nanoparticle. *Scientific Reports*, *10*(1), 18538. https://doi.org/10.1038/s41598-020-75205-3

Petrosino, A., Saporetti, R., Starinieri, F., Sarti, E., Ulfo, L., Boselli, L., Cantelli, A., Morini, A., Zadran, S. K., Zuccheri, G., Pasquini, Z., Di Giosia, M., Prodi, L., Pompa, P. P., Costantini, P. E., Calvaresi, M., & Danielli, A. (2023). A modular phage vector platform for targeted

photodynamic therapy of Gram-negative bacterial pathogens. *iScience*, *26*(10), 108032. https://doi.org/10.1016/j.isci.2023.108032

Porro, G., Basile, M., Xie, Z., Tuveri, G. M., Battaglia, G., & Lopes, C. D. F. (2025). A new era in brain drug delivery: Integrating multivalency and computational optimisation for blood–brain barrier permeation. *Advanced Drug Delivery Reviews*, *224*, 115637. https://doi.org/10.1016/j.addr.2025.115637

Qiao, R., Jia, Q., Hüwel, S., Xia, R., Liu, T., Gao, F., Galla, H.-J., & Gao, M. (2012). Receptor-Mediated Delivery of Magnetic Nanoparticles across the Blood–Brain Barrier. *ACS Nano*, *6*(4), 3304–3310. https://doi.org/10.1021/nn300240p

Qu, Z., Luo, J., Li, Z., Yang, R., Zhao, J., Chen, X., Yu, S., & Shu, H. (2024). Advancements in strategies for overcoming the blood–brain barrier to deliver brain-targeted drugs. *Frontiers in Aging Neuroscience*, *16*, 1353003. https://doi.org/10.3389/fnagi.2024.1353003

Rakonjac, J., Gold, V. A. M., León-Quezada, R. I., & Davenport, C. H. (2024). Structure, Biology, and Applications of Filamentous Bacteriophages. *Cold Spring Harbor Protocols*, *2024*(8), pdb.over107754. https://doi.org/10.1101/pdb.over107754

Rakonjac, J., & Model, P. (1998). Roles of pIII in filamentous phage assembly. *Journal of Molecular Biology*, *282*(1), 25–41. https://doi.org/10.1006/jmbi.1998.2006

Riccardi, C., Napolitano, F., Montesarchio, D., Sampaolo, S., & Melone, M. A. B. (2021). Nanoparticle-Guided Brain Drug Delivery: Expanding the Therapeutic Approach to Neurodegenerative Diseases. *Pharmaceutics*, *13*(11), 1897. https://doi.org/10.3390/pharmaceutics13111897

Rodrigues, M. C., De Sousa Júnior, W. T., Mundim, T., Vale, C. L. C., De Oliveira, J. V., Ganassin, R., Pacheco, T. J. A., Vasconcelos Morais, J. A., Longo, J. P. F., Azevedo, R. B., & Muehlmann, L. A. (2022). Induction of Immunogenic Cell Death by Photodynamic Therapy Mediated by Aluminum-Phthalocyanine in Nanoemulsion. *Pharmaceutics*, *14*(1), 196. https://doi.org/10.3390/pharmaceutics14010196

Roovers, R. C., Vosjan, M. J. W. D., Laeremans, T., El Khoulati, R., De Bruin, R. C. G., Ferguson, K. M., Verkleij, A. J., Van Dongen, G. A. M. S., & Van Bergen En Henegouwen, P. M. P. (2011). A biparatopic anti-EGFR nanobody efficiently inhibits solid tumour growth. *International Journal of Cancer*, *129*(8), 2013–2024. https://doi.org/10.1002/ijc.26145

Saint-Pol, J., Gosselet, F., Duban-Deweer, S., Pottiez, G., & Karamanos, Y. (2020). Targeting and Crossing the Blood-Brain Barrier with Extracellular Vesicles. *Cells*, *9*(4), 851. https://doi.org/10.3390/cells9040851

Sattar, S., Bennett, N. J., Wen, W. X., Guthrie, J. M., Blackwell, L. F., Conway, J. F., & Rakonjac, J. (2015). Ff-nano, short functionalized nanorods derived from Ff (f1, fd, or M13) filamentous bacteriophage. *Frontiers in Microbiology*, *6*. https://doi.org/10.3389/fmicb.2015.00316

Senanayake, D., Yapa, P., Dabare, S., & Munaweera, I. (2025). Precision targeting of the CNS: Recent progress in brain-directed nanodrug delivery. *RSC Advances*, *15*(32), 25910–25928. https://doi.org/10.1039/D5RA03578C

Sioud, M. (2019). Phage Display Libraries: From Binders to Targeted Drug Delivery and Human Therapeutics. *Molecular Biotechnology*, *61*(4), 286–303. https://doi.org/10.1007/s12033-019-00156-8

Spencer, A. P., Torrado, M., Custódio, B., Silva-Reis, S. C., Santos, S. D., Leiro, V., & Pêgo, A. P. (2020). Breaking Barriers: Bioinspired Strategies for Targeted Neuronal Delivery to the Central Nervous System. *Pharmaceutics*, *12*(2), 192. https://doi.org/10.3390/pharmaceutics12020192

Srinivasan, B., Kolli, A. R., Esch, M. B., Abaci, H. E., Shuler, M. L., & Hickman, J. J. (2015). TEER Measurement Techniques for In Vitro Barrier Model Systems. *SLAS Technology*, *20*(2), 107–126. https://doi.org/10.1177/2211068214561025

Strathdee, S. A., Hatfull, G. F., Mutalik, V. K., & Schooley, R. T. (2023). Phage therapy: From biological mechanisms to future directions. *Cell*, *186*(1), 17–31. https://doi.org/10.1016/j.cell.2022.11.017

Sun, B., Li, R., Ji, N., Liu, H., Wang, H., Chen, C., Bai, L., Su, J., & Chen, J. (2025). Brain-targeting drug delivery systems: The state of the art in treatment of glioblastoma. *Materials Today Bio*, *30*, 101443. https://doi.org/10.1016/j.mtbio.2025.101443

Sweeney, M. D., Zhao, Z., Montagne, A., Nelson, A. R., & Zlokovic, B. V. (2019). Blood-Brain Barrier: From Physiology to Disease and Back. *Physiological Reviews*, *99*(1), 21–78. https://doi.org/10.1152/physrev.00050.2017

Szatmári, T., Lumniczky, K., Désaknai, S., Trajcevski, S., Hídvégi, E. J., Hamada, H., & Sáfrány, G. (2006). Detailed characterization of the mouse glioma 261 tumor model for experimental glioblastoma therapy. *Cancer Science*, *97*(6), 546–553. https://doi.org/10.1111/j.1349-7006.2006.00208.x

Teixeira, M. I., Lopes, C. M., Amaral, M. H., & Costa, P. C. (2023). Surface-modified lipid nanocarriers for crossing the blood-brain barrier (BBB): A current overview of active targeting in brain diseases. *Colloids and Surfaces B: Biointerfaces*, *221*, 112999. https://doi.org/10.1016/j.colsurfb.2022.112999

Terstappen, G. C., Meyer, A. H., Bell, R. D., & Zhang, W. (2021). Strategies for delivering therapeutics across the blood–brain barrier. *Nature Reviews Drug Discovery*, *20*(5), 362–383. https://doi.org/10.1038/s41573-021-00139-y

Turrini, E., Ulfo, L., Costantini, P. E., Saporetti, R., Di Giosia, M., Nigro, M., Petrosino, A., Pappagallo, L., Kaltenbrunner, A., Cantelli, A., Pellicioni, V., Catanzaro, E., Fimognari, C., Calvaresi, M., & Danielli, A. (2024). Molecular engineering of a spheroid-penetrating phage nanovector for photodynamic treatment of colon cancer cells. *Cellular and Molecular Life Sciences*, *81*(1), 144. https://doi.org/10.1007/s00018-024-05174-7

Turubanova, V. D., Balalaeva, I. V., Mishchenko, T. A., Catanzaro, E., Alzeibak, R., Peskova, N. N., Efimova, I., Bachert, C., Mitroshina, E. V., Krysko, O., Vedunova, M. V., & Krysko, D. V. (2019). Immunogenic cell death induced by a new photodynamic therapy based on photosens and photodithazine. *Journal for ImmunoTherapy of Cancer*, *7*(1), 350. https://doi.org/10.1186/s40425-019-0826-3

Ulfo, L., Cantelli, A., Petrosino, A., Costantini, P. E., Nigro, M., Starinieri, F., Turrini, E., Zadran, S. K., Zuccheri, G., Saporetti, R., Di Giosia, M., Danielli, A., & Calvaresi, M. (2022). Orthogonal nanoarchitectonics of M13 phage for receptor targeted anticancer photodynamic therapy. *Nanoscale*, *14*(3), 632–641. https://doi.org/10.1039/D1NR06053H

Ulfo, L., Costantini, P. E., Di Giosia, M., Danielli, A., & Calvaresi, M. (2022). EGFR-Targeted Photodynamic Therapy. *Pharmaceutics*, *14*(2), 241. https://doi.org/10.3390/pharmaceutics14020241

Venkataraman, S., Shahgolzari, M., Yavari, A., & Hefferon, K. (2025). Bacteriophages as Targeted Therapeutic Vehicles: Challenges and Opportunities. *Bioengineering*, *12*(5), 469. https://doi.org/10.3390/bioengineering12050469

Wang, H., Yang, Y., Xu, Y., Chen, Y., Zhang, W., Liu, T., Chen, G., & Wang, K. (2024). Phage-based delivery systems: Engineering, applications, and challenges in nanomedicines. *Journal of Nanobiotechnology*, *22*(1), 365. https://doi.org/10.1186/s12951-024-02576-4

Wang, R., Li, H.-D., Cao, Y., Wang, Z.-Y., Yang, T., & Wang, J.-H. (2023). M13 phage: A versatile building block for a highly specific analysis platform. *Analytical and Bioanalytical Chemistry*, *415*(18), 3927–3944. https://doi.org/10.1007/s00216-023-04606-w

Weksler, B. B., Subileau, E. A., Perrière, N., Charneau, P., Holloway, K., Leveque, M., Tricoire-Leignel, H., Nicotra, A., Bourdoulous, S., Turowski, P., Male, D. K., Roux, F., Greenwood, J., Romero, I. A., & Couraud, P. O. (2005). Blood-brain barrier-specific properties of a human adult brain endothelial cell line. *The FASEB Journal*, *19*(13), 1872–1874. https://doi.org/10.1096/fj.04-3458fje

Wu, D., Chen, Q., Chen, X., Han, F., Chen, Z., & Wang, Y. (2023). The blood–brain barrier: Structure, regulation and drug delivery. *Signal Transduction and Targeted Therapy*, *8*(1), 217. https://doi.org/10.1038/s41392-023-01481-w

Wu, L.-P., Ahmadvand, D., Su, J., Hall, A., Tan, X., Farhangrazi, Z. S., & Moghimi, S. M. (2019). Crossing the blood-brain-barrier with nanoligand drug carriers self-assembled from a phage display peptide. *Nature Communications*, *10*(1), 4635. https://doi.org/10.1038/s41467-019-12554-2

Xie, J., Shen, Z., Anraku, Y., Kataoka, K., & Chen, X. (2019). Nanomaterial-based blood-brain-barrier (BBB) crossing strategies. *Biomaterials*, *224*, 119491. https://doi.org/10.1016/j.biomaterials.2019.119491

Yang, R., Wei, T., Goldberg, H., Wang, W., Cullion, K., & Kohane, D. S. (2017). Getting Drugs Across Biological Barriers. *Advanced Materials*, *29*(37), 1606596. https://doi.org/10.1002/adma.201606596

Yu, J.-H., Hamari, Z., Han, K.-H., Seo, J.-A., Reyes-Domínguez, Y., & Scazzocchio, C. (2004). Double-joint PCR: A PCR-based molecular tool for gene manipulations in filamentous fungi. *Fungal Genetics and Biology*, *41*(11), 973–981. https://doi.org/10.1016/j.fgb.2004.08.001

Yuan, F., Wang, Y., Yuan, L., Tang, T., Ye, L., Li, Y., Dai, X., & Cheng, H. (2025). EGFRvIII-positive glioblastoma contributes to immune escape and malignant progression via the c-Fos-MDK-LRP1 axis. *Cell Death & Disease*, *16*(1), 453. https://doi.org/10.1038/s41419-025-07771-1

Zadran, S. K., Facchinello, N., De Rosa, P., Saporetti, R., Costantini, P. E., Ulfo, L., Nigro, M., Petrosino, A., Pappagallo, L., Aloisi, S., Milazzo, G., Din, Z. A., Rigamonti, A., Flora, L., Santulli, M., Cimadom, L., Zuccheri, G., Zangoli, M., Sante, M. D., … Perini, G. (2025). Systematic Targeting of GD2-Positive Neuroblastoma Tumors With a Photooncolytic Phage Nanovector Platform. *Advanced Science*, e15356. https://doi.org/10.1002/advs.202415356